Advances in the Endoscopic Management of Esophageal Neoplasia using Ultrahigh Speed Endoscopic Optical Coherence Tomography

by

Hsiang-Chieh Lee

B.S. Civil Engineering
National Taiwan University, Taiwan, 2004

S.M. Electro-Optical Engineering
National Taiwan University, Taiwan, 2006

SUBMITTED TO THE DEPARTMENT OF ELECTRICAL ENGINEERING AND COMPUTER SCIENCE IN PARTIAL FULFILLMENT OF THE REQUIREMENTS FOR THE DEGREE OF

DOCTOR OF PHILOSOPHY IN ELECTRICAL ENGINEERING AND COMPUTER SCIENCE

AT THE
MASSACHUSETTS INSTITUTE OF TECHNOLOGY

FEBRUARY 2017

Signature of Author: Signature redacted
Department of Electrical Engineering and Computer Science
January 31, 2017

Certified by: Signature redacted
James G. Fujimoto
Professor of Electrical Engineering and Computer Science
Thesis Supervisor

Certified by: Signature redacted
Hiroshi Mashimo
Associate Professor of Medicine, Harvard Medical School
Thesis Supervisor

Accepted by: Signature redacted
Leslie A. Kolodziejski
Professor of Electrical Engineering and Computer Science
Chair, Committee for Graduate Students

Advances in the Endoscopic Management of Esophageal Neoplasia using Ultrahigh Speed Endoscopic Optical Coherence Tomography

by

Hsiang-Chieh Lee

Submitted to the Department of Electrical Engineering and Computer Science on January 31, 2017 in Partial Fulfillment of the Requirements for the Degree of Doctor of Philosophy in Electrical Engineering and Computer Science at the Massachusetts Institute of Technology

ABSTRACT

Esophageal cancer is one of the most lethal malignancies, with a five-year survival rate of only 16.7%. Barrett's esophagus (BE) is a premalignant condition with increased risk of developing into esophageal adenocarcinoma, the most common type of esophageal cancer in the West. In current BE surveillance protocol, random biopsies are used to diagnose and detect dysplasia in BE, which is time-consuming and suffers from sampling error. Endoscopic optical coherence tomography (OCT) is a unique imaging technique that can provide micrometer scale, two- and three-dimensional imaging of esophageal tissue without requiring exogenous contrast agents. Although various studies have investigated the feasibility of endoscopic OCT in the human GI tract, the diagnostic accuracy of endoscopic OCT in the detection of dysplasia in BE was still suboptimal.

Most previous endoscopic OCT studies were limited to investigating the changes in tissue architecture but not microvasculature, due to hardware limitations of the OCT system and optical scanning instability of the imaging catheters. Alteration of microvasculature has been demonstrated as a critical marker of the neoplastic progression of dysplasia in BE. Although OCT has been demonstrated to provide vascular contrast with OCT angiography (OCTA) in ophthalmology, the translation of OCTA to endoscopic applications has been challenging. The aims of this thesis are: 1) Development of distally actuated imaging devices including a micromotor balloon catheter allowing wide field OCTA imaging and a hollow shaft micromotor catheter enabling unobstructed endoscopic OCT imaging in the gastrointestinal tract. 2) A clinical feasibility study investigating the association of OCTA microvascular features with the detection of dysplasia in patients with BE. 3) Laboratory studies using OCT to monitor radiofrequency ablation (RFA) dynamics with concurrent OCT imaging in *ex vivo* swine specimens. The scope of this thesis includes the design and development of novel imaging devices, laboratory imaging studies with both *ex vivo* and *in vivo* animal models, and a collaborative clinical imaging study with patients. The ultimate goal of this thesis work is to facilitate the implementation of endoscopic OCT and OCTA techniques in the endoscopic management of BE.

Thesis Supervisor: James G. Fujimoto
Title: Elihu Thomson Professor of Electrical Engineering and Computer Science

Acknowledgements

Through my Ph.D. journey in the department of the Electrical Engineering and Computer Science at MIT, it has been a great privilege to have the opportunity working with many brilliant scientists, physicians, collaborates, and graduate students. Without their support and active involvement, this thesis work cannot be completed. Many of them continued dedicating their careers in the field of optical coherence tomography (OCT) and played important roles in the advances of OCT in various biomedical applications. I want to especially thank my advisor Professor James Fujimoto for providing me the opportunity of working in this world-class laboratory, as well as his guidance and support over these years. The research environment he offered is more than a graduate student can expect. I also thank my thesis co-advisor Dr. Hiroshi Mashimo for his long-term mentoring and support on the endoscopic OCT projects conducted at the VABHS and the friendship over these years. I thank my thesis committee member, Professor Elfar Adalsteinsson for his input and advice to polish my thesis. In addition, I want to thank Dr. Chao Zhou and Dr. Aaron Aguirre for their mentorship, allowing me to continue the development of optical coherence microscopy (OCM) technique. I also want to thank Dr. Tsung-Han Tsai for his guidance and friendship since the first day I joined Professor Fujimoto's lab, patiently teaching me the secrets of Fourier-domain mode-locked laser as well as the hard-core OCT catheter engineering.

It was a great pleasure to work on the endoscopic OCT project (the "GI team") since the beginning of my Ph.D. journey at MIT. I had a great time working with various former or current GI team members including Dr. Desmond Adler, Dr. Chao Zhao, Dr. Tsung-Han Tsai, Dr. Zhao Wang, Osman Ahsen, and Kaicheng Liang, as well as the support from Dr. Yuankai Tao, Dr. Michael Giacomelli, and Dr. Ning Zhang. I am sure I will never forget the "VA Mashimo Monday" and the RLE van we often reserved for the commute between the MIT and VA. In particular, I want to thank Osman Ahsen and Kaicheng Liang, being such incredible and extremely helpful colleagues and friends. It was a truly an honor for me to closely working with you over the past four years. I would also like to express my appreciation to Dr. Hiroshi Mashimo, Dr. Qin Huang, Dr. Laren Becker, Dr. Tejas Kirtane, Dr. Walter Chan, Marisa Figueiredo, Dr. Frances Achee, Rachel Bereiweriso, Rayhme Collins, Caroline Costa, Greg Daniels, the nursing staff and the technicians in the endoscopic unit at VABHS, in particular, Annalee Murphy and Joanne Hill for their putting up with the space being occupied by the OCT instruments, the fragile OCT imaging catheters, and sometimes the last minute add-on of the OCT schedule.

I thank Dr. Aaron Aguirre, Dr. Chao Zhou, and Dr. Jonathan Liu at MIT, as well as Dr. David Cohen, Dr. Dejun Shen, Dr. Yuri Sheikine, and Dr. James Connolly in the Department of Pathology at Beth Israel Deaconess Medical Center for their support on the development and application of OCM for the path lab imaging. In addition, I would like to thank both former and current members of the Biomedical Optics Imaging and Biophotonics Group at RLE and MIT including Dr. Shu-Wei Huang, Dr. Bernhard Baumann, Dr. Ireneusz Grulkowski, Dr. Yueli Chen, Dr. Umit Demirbas, Dr. Alphan Sennaroglu, Dr. Yu Gu, Dr. Al-Hafeez Dhalla, Dr. Duo Li, Jing Wang, Dr. WooJhon Choi, Dr. Martin Kraus, Chen Lu, ByungKun Lee, Eric Moult, Tadayuki Yoshitake, Lucas Cahill, Kathrin Mohler, Lennart Husvogt, Stefan Ploner, Julia Schottenhamml.

Although I did not have a chance to work with you on the projects in ophthalmology and microscopy, the exchanges of opinions on various topics during the daily interaction and the assistance of the lab-related works make my lab life more interesting and fulfilling. And of course, I thank Ms. Dorothy Fleischer for all the administrative assistance and the heartwarming encouragement whenever I felt down or frustrated over these years. I thank Professor Erich Ippen and Professor Franz Kaertner for being part of my delightful MIT life, in particular, the Oktoberfest and the Christmas parties, makes me feel welcome while studying aboard alone.

I also want to thank the strong industrial support making my thesis work possible. I thank Dr. Benjamin Potsaid and Mr. Alex Cable from Thorlabs, Inc., as well as Dr. Vijarsekhar Jayaraman from Praevium Research, Inc. for their continuing support of VCSEL light source and other critical electronic components to facilitate the development of the ultrahigh speed endoscopic OCT engine. I thank Mr. Eric Swanson, Dr. Long Chen, and Dr. Chris Doerr from Acacia Communication, Inc. for their support of the development of the silicon photonic integrated SS-OCT system. I must thank the National Institute of Health and the Air Force Office of Scientific Research for the funding assistance to support my thesis work.

Lastly, I want to save the most appreciative thanks for my friends and family. I want to thank my parents Feng-Liang Lee and Mei-Hua Lai for their sacrifice and unwavering love over these years supporting me to chase my dream studying aboard. My wife, Li-Hsin Chen, who stopped her career temporarily and came to the US to take care of me during the most challenging period of my Ph.D. journey. I am fortunate and blessed to have the support from my sister, Ying-Ling Lee, and brother Zhung-Fu Lee taking care of the family while I am not at home. Thanks to all my wonderful friends, in particular, Chien-Jen Lai, Cheng-Wei Cheng, I-Hua Chen, Tsung-Han Tsai, Chun-Ting Su, and Jonathan Liu.

TABLE OF CONTENTS

CHAPTER 1

1.0 Introduction: Endoscopic Management of Barrett's Esopahgus

1.1 Background – Barrett's Esophagus and Esophageal Carcinoma

Barrett's esophagus (BE) is a common esophageal disease affecting 1% to 2% of the general population in the West [1] and represents a strong precursor in the neoplastic progression of esophageal cancer. In particular, esophageal adenocarcinoma (EAC), the most common type of esophageal cancer in the West, has a poor 5-year survival rate of 17% [2]. The incidence of EAC has increased 3-6 fold over the past 3-4 decades [3-5]. BE is highly associated with several risk factors including male gender, white race, age, and the presence of chronic gastroesophageal reflux disease (GERD) [6]. Histopathologically, BE is characterized by the replacement of stratified esophageal squamous epithelium with metaplastic columnar epithelium containing goblet cells, termed specialized intestinal metaplasia (IM). Endoscopically, BE is visualized under white light illumination as salmon-colored mucosa above the gastric folds. The neoplastic progression of BE to EAC involves a multistep process from non-dysplastic BE (NDBE) to low-grade dysplasia (LGD), high-grade dysplasia (HGD), and EAC [7]. For patients diagnosed with NDBE but not dysplasia, the annual risk of EAC is about 0.1-0.3% [8, 9]. In contrast, The incidence of EAC is significantly increased in patients with any grade of dysplasia [8], and HGD is associated with 10-60% increased risk of developing into EAC within 3-5 years [7, 10, 11]. The detection of dysplasia relying on conventional white light endoscopy (WLE) is challenging due to the patchy nature of dysplasia in the background of NDBE [12] and also the minute differences in surface and vascular pattern between lesions with dysplasia and neighboring NDBE tissue. Only 13% of dysplastic lesions are present in the nodular or raised form, and discernible on WLE [13].

Therefore, for patients with prior diagnosis of NDBE, surveillance EGD with standard Seattle biopsy protocol is recommended, which involves the collection of biopsy specimens at 4 quadrants of the esophagus with an interval of every 2 cm till the top of the BE mucosa is reached. Prior to the biopsy procedure, the BE length is documented carefully following the Prague C&M criteria [14] where C and M correspond to the distance from the incisor to the circumferential and maximum extent of the BE mucosa (salmon-color appearance) respectively to facilitate performing Seattle biopsy protocol. Although this rigorous biopsy showed a significant increase in the number of detected HGD cases [15], it is challenging to adhere to the exact protocol in community centers. Even among endoscopists, the adherence becomes worse

for cases with long segment BE [16, 17], suggesting the need for advanced imaging tools to enhance the contrast of dysplastic regions in the background of NDBE, and enable a more cost-effective and sensitive targeted biopsy approach.

1.2 Advanced Endoscopic Imaging Methods for Dysplasia Detection in BE

To date, various advanced endoscopic imaging modalities have been developed and investigated to facilitate the detection of dysplasia in BE. In the later sections, the background and current opinion on selected advanced imaging modalities including chromoendoscopy, narrow band imaging, and confocal laser endomicroscopy will be briefly reviewed and discussed.

1.2.1 Chromoendoscopy

Chromoendoscopy involves the topical spray of dyes to enhance the surface mucosal or vascular pattern, and is often used in combination with magnification endoscopy to better differentiate dysplasia from neighboring NDBE tissue because of improved resolution. Various dyes have been used in chromoendoscopy including methylene blue (MB), indigo carmine, cresyl violet, and acetic acid (AA) in the examination of BE. Since the clinical utility of MB- or AA-based chromoendoscopy has been investigated most comprehensively, the following discussion will focus on chromoendoscopy utilizing these two dyes. In practice, chromoendoscopy involves two parts: the use of a spray catheter to distribute dyes evenly over the esophageal luminal surface, and the subsequent examination of the surface mucosa with white light magnification endoscopy.

In MB based chromoendoscopy, which typically uses 10-20 mL of 0.5% of MB for every 5 cm BE mucosa [18], a regular, homogeneous dark blue colored mucosa is observed in BE. In contrast, dysplasia is characterized as irregular, heterogeneous, and either very dark or light blue colored mucosa [19]. Despite its initial success in differentiating IM and dysplasia in BE [20], subsequent studies showed varying accuracy in the detection of dysplasia [21-24]. A recent meta-analysis study including 450 patients concluded that targeted biopsy by MB-based chromoendoscopy showed no additional benefit compared to conventional Seattle protocol [25]. In addition, MB is a vital stain that can induce oxidative damage to DNA in response to white light illumination [26]. Therefore, MB based chromoendoscopy is not regularly used in clinical practice today.

On the other hand, acetic acid based chromoendoscopy (AAC) uses acetic acid to enhance the visualization of surface mucosa patterns because of reversible acetylation of nuclear proteins within the BE mucosa [27]. Typically, a 1.5% to 3% acetic acid solution is sprayed over the BE mucosa. AAC was first demonstrated in combination with magnification endoscopy investigating the feasibility of detecting SIM in BE based on surface mucosa patterns [28]. For gastric epithelium, the surface mucosal pattern is characterized by circular pits. Surface mucosa patterns showing the absence of circular pits, and the presence of villous or ridged (cerebriform) patterns are suggestive of SIM [28]. Subsequent studies demonstrated high accuracy in the detection of dysplasia using targeted biopsies guided by AAC without magnification [29, 30]. In addition, a high correlation of the surface mucosal patterns with the histology was observed [29]. Although studies have shown the improved yield of targeted biopsy guided by AAC, randomized studies still need to be performed. In addition, acetic acid alters the electrical conductivity of the surface of BE mucosa, which might affect the efficacy of certain endoscopic treatments, such as radiofrequency ablation (RFA) [31]. Lastly, compared to virtual or optical chromoendoscopy, the spray procedure in AAC is still relatively time-consuming.

1.2.2 Narrow Band Imaging (Virtual Chromoendoscopy)

Virtual or optical chromoendoscopy is an imaging technique extended from existing WLE platforms that use optical filters and post processing to enhance the visualization of surface mucosal and vascular patterns. Compared to Fujinon FICE or Pentax i-scan techniques, narrow band imaging (NBI, Olympus Inc.) is the most widely utilized optical chromoendoscopy technique in clinical practice today, and thus this section will solely focus on NBI. NBI, first described by Gono et al. in 2004 [32], uses optical filters to limit illumination from white light to two narrow spectral bands with specific central wavelengths of 415 nm and 540 nm, that are strongly absorbed by hemoglobin and penetrate only the surface of the esophageal mucosa. The feasibility of NBI on dysplasia detection in BE was first investigated in combination with magnification endoscopy [33, 34]. For NDBE or IM, it is characterized by a regular villous or ridge surface mucosal pattern with a regular vascular pattern and absence of abnormal vessels. On the contrary, the dysplastic region is characterized by an irregular/distorted surface mucosal pattern with an irregular vascular pattern and increased vascularity. A recent meta-analysis of 8

studies including 446 patients showed a high detection accuracy of dysplasia in BE with a 96% sensitivity and 94% specificity using NBI with magnification endoscopy. However, the detection accuracy decreased to 95% sensitivity and 65% specificity on NDBE pathology. Furthermore, when comparing the accuracy for the detection of patients with dysplasia, NBI without using magnification endoscopy (targeted biopsies) showed comparable performance (sensitivity/specificity: 52.7%/100%) to standard high-definition (HD) WLE (targeted + random biopsies (Seattle protocol), sensitivity/specificity: 63.6%/100%) [35]. The sensitivity of NBI is significantly decreased compared to using magnification endoscopy.

1.2.3 Confocal Laser Endomicroscopy

Confocal laser endomicroscopy (CLE) is an emerging endoscopic imaging technique allowing real time and high resolution imaging in the human GI tract during endoscopy [36]. Unlike previous 'red flag,' wide field imaging techniques such as chromoendoscopy or NBI, the imaging field of CLE is more limited. In the literature reported to date, there exists two different CLE platforms: (1) a special endoscope integrating CLE into the distal end of the endoscope (eCLE, Pentax Medical, NJ) or (2) a small size probe comprising a 30,000-core fiber bundle that can be introduced into the 2.8 mm instrument channel of a standard endoscope (pCLE, CellVizio, Mauna Kea Technologies, France) [37]. In CLE, *in vivo* fluorescence imaging was performed by scanning the tissue surface with a blue laser following either topical or intravenous (IV) application of contrast agents. In current practice, IV application of 3-5 mL of 10% fluorescein is the preferred method due to its superior safety over other agents such as cresyl violet or acriflavine [38]. The specifications of CLE imaging performance vary between the two platforms. Although eCLE has larger imaging coverage (~475 x 475 μm^2) over pCLE (240 x 240 μm^2), the frame rate of eCLE is limited to <2 frames per second (fps), which is slower than 12 fps in pCLE.

The initial study by Kiesslich et al. in 2006 demonstrated the feasibility of using CLE to predict the pathology of BE and dysplasia with 98.1% and 92.9% sensitivity as well as 94.1% and 98.4% specificity, respectively [36] albeit only approximately 38% of the CLE images acquired exhibiting good quality. Later studies developed a consensus image analysis criteria in differentiating HGD/EAC vs. NDBE [39]. A recent large scale multicenter randomized controlled study of 192 patients demonstrated the added clinical utility of CLE for improving the

sensitivity in detecting dysplasia from 40% to 96% by using a combination of endoscopic examination of HD-WLE with eCLE [40]. In addition, the diagnostic yield of targeted biopsy has been increased by 3x fold. Despite the promising results in the detection accuracy of dysplasia in BE, there exist several limitations in CLE. First, most of the high accuracy studies were reported with the eCLE modality, using the relatively high image quality of the eCLE platform. However, eCLE is no longer available commercially. In addition, the limited imaging field of CLE, in particular, pCLE makes it challenging to survey wide areas of the esophagus, and vulnerable to sampling error when correlating the histopathological diagnoses with the CLE images [41].

Recently, studies have demonstrated high resolution imaging of BE using a low cost, confocal laser endomicroscopy platform with a 1 mm diameter fiber bundle imaging probe, termed high resolution microendoscopy (HRME) [42]. The configuration of HRME is very similar to pCLE, without requiring the optical beam scanning unit. In addition, a high speed 2D camera was used to detect fluorescence images rather than a single detector. For the fluorescence imaging, a topical application of 0.01% proflavine is used, followed by light illumination over the tissue surface using a 455 nm blue light emitting diode. Based on these hardware implementations, HRME systems can be built at a low cost of <$3500 [43]. Using HRME, a recent study has reported a detection accuracy of HGD and early EAC with 90% sensitivity and 82% specificity. Although HRME showed high detection accuracy in initial results, the contrast agents used (proflavine) are still under investigation, and carry a mutagenic effect on DNA. In addition, the imaging field is still relatively limited (~720 x 720 μm^2).

1.3 Endoscopic Treatment Methods for the Eradication of Dysplasia in BE

The ultimate goal of the treatment of dysplasia in BE is the resection or ablation of dysplastic BE mucosa followed by acid suppression medication to promote the re-epithelization (generation of the neosquamous mucosa) over treated BE mucosa. In the endoscopic resection approaches, the histopathological information of the resected specimen is available, which can be used to accurately stage the resected specimen if the tumor is involved, as well as assessing the lateral and deep resection margins. On the contrary, the histological information over regions treated with ablative methods is not available. In the following sections, the most commonly used endoscopic resection and ablative treatments methods including endoscopic mucosal resection

(EMR), radiofrequency ablation (RFA) and cryoablation, will be briefly reviewed and discussed below.

1.3.1 Endoscopic Mucosal Resection

Endoscopic mucosal resection (EMR) is a treatment method that not only removes the neoplastic tissue (potential curative value) but also provides histopathological information of the resected specimens. The practice of EMR was first described by Inoue et al. in 1992 [44]. The EMR procedures can be performed in three different approaches: injection assisted, cap assisted, or ligation assisted [45]. Among these three approaches, due to its ease of use, cost and time [46], the ligation assisted EMR procedure has been widely performed. In the ligation assisted EMR procedure (Duette multiband mucosectomy kit (Cook Medical, IN)), the suspected lesion is suctioned into a cylindrical end cap, and the rubber band over the end cap is released to create a pseudopolyp, which can be resected via hot snare and retrieved for histological assessment.

Several prospective studies showed the complete remission rate of dysplastic and early EAC lesions with EMR, and a high 5-year survival rate of 84-98% [47-49]. Although attempts to resect entire lengths of BE mucosa have been demonstrated via stepwise EMR procedures, a high rate of esophageal stenosis has been observed [50]. Therefore, along with the advances in ablative treatment methods as described in the later section, a treatment regimen combining the use of EMR to remove nodular regions and subsequent ablative treatments has been adopted in the current practice of complete eradication of dysplasia in BE [51]. Apart from the therapeutic value of EMR, previous studies also reported a greater interobserver agreement in the pathologic diagnosis by EMR than that of pinch biopsies (LGD, κ=0.33 vs 0.22, $P < 0.001$; HGD, κ =0.43 vs 0.35, $p < 0.02$) [52]. A 25% change of diagnosis was observed among patients with HGD and early EAC lesions by using EMR as a diagnostic tool [53]. In addition, compared to endoscopic ultrasound (EUS), EMR allows accurate T staging and precise assessment of the lymphovascular involvement by providing a larger resected specimen over the pinch biopsy [54].

1.3.2 Radiofrequency Ablation

Radiofrequency ablation (RFA) uses an electrode array to deliver RF energy superficially to the dysplastic esophageal tissue [31, 55, 56]. It has been demonstrated as a safe and effective

treatment method toward the eradication of dysplasia in BE compared to other endoscopic treatment methods. In RFA, the low-frequency electromagnetic field results in rapid oscillation of charged ions within the tissue and creates molecular friction leading to the thermal injury of the treated tissue [57]. The commercially available RFA devices (Barrx series, Medtronic (formerly BARRX Medical, CA), MN) can be generally divided into two categories based on the treatment area: (1) circumferential ablation catheters which consist of an inflatable balloon with a variety of balloon sizes to accommodate the varying diameter of the esophagus among individuals (18-31 mm in diameters), and (2) focal ablation catheters which can be mounted to the distal end of the endoscope or introduced through the instrument channel of the endoscope for targeting specific lesions inside the esophagus under endoscopic guidance.

To date, various studies have demonstrated the efficacy and durability of RFA in the complete eradication of dysplasia (CE-D) in BE. Among patients who received RFA treatments for either NDBE (IM) or any grade of dysplasia, 78% and 91% of the patients achieved complete eradication of IM (CE-IM) and CE-D, respectively, based on a recent large scale, meta-analysis study [58]. In addition, CE-IM was achieved in 92% of patients at the five-year follow-up [56]. Furthermore, a low stricture rate (<6%) was reported among the patients treated with RFA compared to previous treatment methods [31, 59]. Therefore, RFA has become the standard treatment for patients with BE and dysplasia. However, RFA also has several limitations. Repeated RFA sessions were required to achieve CE-IM or CE-D. On average, 3.4 and 3.5 sessions were required for patients with IM alone [60] or any grade of dysplasia to achieve CE-IM [31], respectively. In addition, abrasion of coagulum between multiple RFA applications at each treated site is critical to ensure sufficient treatment efficacy. Lastly, the assessment of the effectiveness of each RFA application mainly relied on visual inspection, which might be challenging due to bleeding from the ablated sites. Recently, a high recurrent rate of IM has been reported in 13% [31], and 25.9% [61] of the patients who received RFA treatment for dysplasia at 1 year after CE-IM was achieved, suggesting that current RFA practice might not be optimal.

1.3.3 Cryospray Ablation

Cryospray ablation utilizes the application of cryogen over the dysplastic BE mucosa, with repeated cycles of fast freezing and slow thawing to generate tissue injury. The mechanism of

tissue injury due to cryogen application is relatively complex compared to RFA and associated with several factors, such as the number of spray cycles, the temperature at the tissue surface, and the durations of the freezing/thawing in each cycle [62]. Although cryospray ablation can also be performed using compressed carbon dioxide, the cryospray ablation (CSA) system using liquid nitrogen (CSA Medical Inc., MA) has been the most investigated. In CSA, as a non-contact ablation method, liquid nitrogen is sprayed over the tissue surface using a 7 French catheter introduced through the 2.8 mm instrument channel of a standard endoscope, while a decompression tube is placed in advance to ventilate the nitrogen gas. Ablation with 15-20 secs of liquid nitrogen (-176 degrees Celsius) and followed by a complete thawing is recommended by the manufacturer. In addition, for each targeted lesion, 3-4 cycles of freezing-thawing is recommended.

CSA was first demonstrated by Johnston et al. to treat BE [63]. In this study, 9 of 11 patients with BE and dysplasia achieved complete eradication of intestinal metaplasia (CE-IM) after treatment with CSA. High CE-D rates of 88% and 87% were reported from two separate studies by Greenwald et al. and Shaheen et al., respectively [64, 65]. However, the CE-IM rates reported in these two studies were limited to ~50%, suggesting the potential of recurrent BE. A subsequent study of 36 patients who achieved CE-IM after CSA for HGD prior to being enrolled in the study reported a recurrent rate of 30% patients at a median 6.5 months follow-up period [66].

Recently, with better hardware designs, which include lower flow, better venting and more even spray (leading to less distention for the patients), the complexity of the CSA procedure (freezing, thawing, and the need for decompression tube for ventilation) has been reduced (truFreeze, CSA Medical Inc., MA). Nevertheless, in general, the CSA procedure time is usually longer than RFA. In addition, the dosing in CSA procedures is relatively imprecise compared to RFA. Lastly, the CSA system footprint is still relatively bulky, and limited by the liquid nitrogen tank inside the system. Recently, a novel focal cryoablation catheter (The Coldplay CryoBalloon, C2 Therapeutics, CA) became commercially available. It combines an inflated balloon with a spray catheter and can be controlled via a compact battery-powered handle [67]. The cryoballoon catheter can be introduced through the 3.7 mm instrument channel of a therapeutic endoscope.

The balloon is inflated after reaching the targeted lesion and centered with respect to the size of the esophagus lumen, followed by a continuous and stable release of nitrous oxide (-85 degrees Celsius). The nitrous oxide flow stops once reaching the preset ablation duration. Initial studies demonstrated the feasibility of squamous regeneration over previously treated regions. Future large scale studies are required to validate its clinical utility in eradicating dysplasia in BE.

1.4 Endoscopic OCT in the Endoscopic Management of BE

Optical coherence tomography (OCT) is an imaging technique that can perform two and three-dimensional (3D) imaging of tissue architecture with near microscopic resolution [68]. Since its first demonstration in the *ex vivo* imaging of human retina and coronary artery tissue in 1991 [68], OCT technology has been successfully applied to a wide variety of applications, such as ophthalmology [69], cardiology [70, 71], gastroenterology [72-74], urology [75], dermatology [76, 77], and gynecology [78-80]. In 1997, Tearney et al. first demonstrated *in vivo* endoscopic OCT imaging of the rabbit esophagus and trachea using a 1 mm diameter fiber-optic catheter [81]. The architectural features of the rabbit esophagus and trachea identified in the OCT images were well correlated with corresponding histology. Endoscopic OCT was later applied to investigate the architectural features of the gastrointestinal (GI) tract such as the esophagus and stomach [73, 74, 82-88], small and large intestines [74, 83, 89, 90], and bile ducts [91, 92].

BE architectural features are clearly differentiated from the normal esophagus due to the metaplastic process during BE progression. Endoscopic OCT has been previously demonstrated to differentiate SIM or NDBE from normal squamous and gastric mucosa [85, 93]. Recently, two separate studies investigated the accuracy of detecting dysplasia in BE [94, 95]. Isenberg et al. reported a 68% sensitivity and an 82% specificity for the detection of dysplasia from 33 patients with BE [94]. Evans et al. reported an 83% sensitivity and 75% specificity for detecting HGD and intramucosal carcinoma (IMC) with a scoring system using blinded OCT images from 55 patients [95]. Recently, Leggett et al. reported a decision tree based diagnostic algorithm comprising three OCT structural features: (1) effacement of the mucosal layer, (2) OCT signal contrast between the surface and subsurface regions, and (3) the number of atypical glands [96]. 86% sensitivity and 88% specificity were reported for detecting dysplasia on 50 *ex vivo* EMR specimens by performing the diagnostic algorithm in multiple OCT frames in individual 3D

OCT datasets. In addition to performing manual analysis on the endoscopic OCT images, Qi et al. reported an 82% sensitivity and 74%specificity for identifying dysplasia in 13 patients based on a computer-aided analysis algorithm [97].

Although studies have demonstrated the feasibility using of endoscopic OCT to differentiate dysplasia from NDBE, the slow imaging speed limited endoscopic OCT imaging coverage of the esophagus. With the recent development of Fourier-domain (FD) detection techniques, both the imaging speed and quality of the OCT datasets have significantly improved [98, 99]. Volumetric endoscopic OCT imaging of the esophagus was first demonstrated in animal models *in vivo* using high speed FD-OCT systems [86, 87]. Subsequent studies have investigated endoscopic OCT in various gastroenterology applications either using a small size probe to provide high resolution imaging over the targeted area [100-103] or a balloon imaging catheter to perform endoscopic OCT imaging with large field coverage [104, 105]. Because of the rapid development of high speed OCT technology, endoscopic OCT has been used to image patients who received prior treatments for dysplasia. Adler et al. showed identification of subsquamous specialized intestinal metaplasia (SSIM) in patients treated with RFA in previous EGD visits [100]. In conventional biopsy procedures, both the sampling depth and area are limited. Therefore, SSIM is hard to detect without endoscopic OCT. Two other studies have shown improved detection of SSIM using OCT images from patients *in vivo* [103] and also from the analysis of the esophagectomy specimens [106] compared to standard biopsy.

As a result of limited catheter scanning speeds and OCT system imaging speeds, the majority of previous endoscopic OCT studies were limited to investigating changes in tissue architecture during BE progression identified in cross-sectional OCT images [95, 96, 107]. Several architectural features in BE progression have been identified in previous studies, for example, the difference in the OCT signal intensity between surface and subsurface mucosal layers (surface maturation), the presence of distorted glandular architecture (number and shape), and the effacement of the mucosal layer [95, 96].

Angiogenesis has been identified as a precursor in tumor progression and spreading [108]. The formation of new vessels from a pre-existing vascular network has been demonstrated as an

early event in the neoplastic progression from NDBE to dysplasia [109, 110]. OCT angiography (OCTA) has been used to visualize 3D microvasculature using the Doppler effect to isolate blood flow from static tissue [111, 112]. OCTA was later performed using motion contrast, by calculating the amplitude, phase, or complex amplitude variation of the OCT signals between neighboring B-scan frames [113]. Amplitude-based OCTA relaxes phase stability requirements of the OCT system and has good sensitivity to slow blood flows in the capillaries [114-118]. However, performing OCTA endoscopically has been challenging. Early studies suggested the feasibility of identifying 2D blood flow in the human GI tract and 3D blood flow in the living swine but did not visualize microvasculature [119, 120]. Recently, using an ultrahigh speed endoscopic OCT system and a micromotor imaging catheter, our group performed the first demonstration of OCT angiographic imaging to detect microvasculature in a patient with NDBE [121]. Due to technical advances, these methods can provide detailed information on the structural/functional changes in the subsurface glandular/microvascular features, which might facilitate the early detection of dysplasia in BE using OCT/OCTA techniques.

1.5 Scope of the Thesis

The aims of this thesis work are described as follows. 1) Development of distally actuated imaging devices including a micromotor balloon catheter allowing wide field OCTA imaging and a hollow shaft micromotor catheter enabling unobstructed endoscopic OCT imaging in the gastrointestinal tract. 2) A clinical feasibility study investigating the association of OCTA microvascular features with the detection of dysplasia in patients with BE. 3) Laboratory studies using OCT to monitor radiofrequency ablation (RFA) dynamics with concurrent OCT imaging in *ex vivo* swine specimens.

This thesis is organized according to these aims. Chapter 2 describes the design and specification of the novel 360-degree unobstructed imaging micromotor imaging catheter. Chapter 2 also presents the preliminary results using this novel micromotor imaging catheter in combination with an ultrahigh speed OCT system to perform OCT and OCTA imaging of human tissue. Chapter 3 describes the design and specification of the micromotor imaging catheter as well as the imaging results of circumferential wide field OCTA imaging of the swine esophagus. Chapter 4 summarizes the feasibility study of using OCTA to identify microvascular features

associated with dysplasia in BE. Chapter 4 also reports the preliminary results of the detection accuracy of using OCTA images on multiple blinded readers testing the developed OCTA criteria. Chapter 5 details the feasibility study of using OCT to identify and measure the changes of tissue architecture with respect to RFA applications with different RF energy density settings. Chapter 6 concludes the thesis work.

CHAPTER 2

2.0 Endoscopic Optical Coherence Tomography Imaging using a 360-degree Unobstructed Micromotor Imaging Catheter

2.1 Motivation

To date, a variety of endoscopic OCT imaging catheters has been developed to address the special need for different luminal organs such as the size and imaging coverages. In general, these catheters can be divided into two categories based on the beam scanning methods: forward viewing or side viewing catheters. In particular, because of the potential to provide wide field imaging over the luminal surface, side viewing catheters has gained relatively strong interests over the forward viewing imaging catheters.

Among various scanning methods observed in the side viewing catheters, a spiral (helical) scanning is the most common method to achieve a 2D optical beam scanning over the tissue surface with side viewing catheters. Conventionally, the helical scanning pattern is achieved by rotating the distal optics assembly using the torque transmitted from the proximal rotary motor through the torque cable while proximally translating the entire catheter longitudinally. Although it can enable very small size catheters and exhibits a low manufacturing cost, the proximal rotary actuation is vulnerable to the relatively poor frame-to-frame repeatability, resulting in nonuniform rotation distortion (NURD) observed in the OCT images. The NURD becomes exacerbated if the catheter needs to pass through multiple bends in order to reach the imaged site because of the complex organ geometry. In addition, the rotary frame rate is limited by the fiber-optic rotary joint (FORJ) used in the proximal rotary actuation scheme, which makes endoscopic OCT imaging more vulnerable to motion artifacts, such as respiration or cardiac motion, even though high speed imaging is used.

Alternatively, distal scanning method either using a miniature piezoelectric transducer (PZT) [122-125] or microelectromechanical system (MEMS) [126-130] scanner allows precise beam scanning over the tissue surface and has demonstrated endoscopic OCT imaging with resolution near cellular level. However, the size of most MEMS imaging catheters is still relatively bulky, in particular, those with electromagnetic actuation albeit a lower driving voltage (<10 volts) [128] compared to electric static ones (~tens of volts) [129]. On the other hand, the imaging field of the PZT based imaging catheters is relatively limited although the small catheter size. Also, the assembling process of PZT catheter is relatively complicated. Different from the approaches aforementioned, a distal micromotor imaging catheter enables precise circumferential beam

scanning without requiring an FORJ [131, 132]. In combination with a proximal pullback actuation, micromotor imaging catheters can provide a wider imaging coverage and less vulnerable to the flexing of the catheters. Various studies have investigated the feasibility of endoscopic OCT imaging using micromotor imaging catheters in different luminal organs. More importantly, as a result of low NURD, our group has successfully demonstrated endoscopic OCT angiography (OCTA) in the human GI tract using an ultrahigh speed OCT system and micromotor catheters [121, 133]. Endoscopic OCTA enables volumetric imaging of the subsurface microvasculature of esophageal mucosa at a frame rate of 400 frames per second (fps) and an imaging speed of 600,000 axial scans per second.

However, one crucial drawback of the micromotor imaging catheter is the motor wiring shadowing, which obscures a portion of the imaging coverage along the circumferential/rotary direction [134-136]. In addition, due to the scanning mechanism of the micromotor, a metal housing was used to facilitate the alignment and mounting of the micromotor as well as the focusing optical components in the micromotor imaging catheters [133, 135]. In our previous study [137], a customized brass housing with a single large window was used to enable ~70% imaging coverage in the rotary/circumferential direction, while still providing sufficient mechanical strength over the strut part. As a result of the imaging field blockage, prior to the imaging acquisition, the operator needs to align the imaging window facing toward the regions of the interest (ROIs), which prolongs the imaging session and also affects the yield of the OCT images. One potential approach would be to replace the metal housing with transplant material, such as plastic tubing or a hollow glass rod. However, this will introduce aberration into the focused light beam as well as increasing back-reflection from multiple interfaces, which can affect the quality of the OCT images.

Recently, several groups have demonstrated unobstructed full circumference imaging with PZT based squiggle motors, which allows light propagating through the central hollow space of the motor and being focused afterward with either a GRIN lens or ball-lensed fiber [138, 139]. However, the imaging speed was very slow (2 fps). In addition, the vibration resulted from the PZT benders or cubes might affect the fiber positioning inside the motor during the rotation. In this study, we developed a micromotor imaging catheter allowing 360-degree unobstructed

circumferential/rotary imaging coverage using a novel DC brushless hollow shaft motor. In combination with an ultrahigh speed OCT system, volumetric OCT images of a human finger/buccal mucosa as well as a healthy human rectal-anal junction (dentate line) were demonstrated at a 200 fps frame rate and a 600 kHz axial scan rate. In addition, an NURD correction algorithm similar to the version recently demonstrated by our group [137, 140] was implemented to suppress NURD from the brushless hollow shaft micromotor, enabling endoscopic OCT angiography (OCTA) [121]. Volumetric imaging of the subsurface microvasculature naturally coregistered to the structural volumetric OCT dataset was demonstrated. This study showed unobstructed coregistered endoscopic OCT and OCTA imaging using a novel 360-degree micromotor imaging catheter.

The prototype ultrahigh speed OCT engine used in this study was developed in a team effort led by a previous graduate student, Tsung-Han Tsai with the assistance from Drs. Benjamin Potsaid and Yuankai Tao, and Osman Ahsen in Professor Fujimoto's group. Osman Ahsen designed and built the 2nd generation of the patient interface for clinical OCT imaging as well as the optimization of the acquisition software enabling streamline large size OCT data storage and on site *en face* visualization of the OCT dataset immediately post acquisition. Both features were critical to facilitate the workflow of the OCT imaging session in the endoscopy suite. Kaicheng Liang and Osman Ahsen participated in the discussion of the design of the 360-dgree micromotor catheter and the development of the NURD correction algorithms used in this study. The OCT data of the human lower GI tract presented in this study was taken in collaboration with Dr. Hiroshi Mashimo, MD. PhD., who performed the endoscopy session. All the data processing and analysis were performed by the author of the thesis work.

2.2 Development of the 360-degree Unobstructed Imaging Catheter

2.2.1 Ultrahigh speed endoscopic OCT system

In this study, an ultrahigh speed endoscopic OCT system as described in detail previously [121, 133] was used (Figure 2.1). Briefly, a 1310nm MEMS-tunable vertical-cavity surface-emitting laser (VCSEL) light source was driven a 300 kHz sinusoidal signal to provide an effective 600kHz Ascan rate (bidirectional sweep) with a ~120 nm wavelength sweep range and an output

optical power of ~50 mW. Five percent of the light source output was connected to a Mach-Zehnder interferometer (MZI) and detected using a dual balanced optical clock generator (Thorlabs Inc., NJ). A clock signal with a maximum clock frequency of ~1.1GHz, as determined by the optical path length difference in the MZI, and the optical bandwidth and sweep rate of the wavelength swept light source was used to external clock a high speed, 12bit, A/D acquisition card (ATS 9373, AlazarTech, Canada). The implementation of optical clock eliminates conventional wavelength calibration steps in the post-processing and hence decreases the computation cost of OCT imaging.

The remaining 95% of light output was connected to a dual circulator based Michelson interferometer comprising a 95/5 fiber-optic coupler (AC Photonics, CA). Light returning from the reference arm and sample arm were interfered at the 50/50 fiber-optic coupler (AC Photonics, CA) and connected to a dual balanced photodetector (PDB480C-AC, Thorlabs, Inc., NJ). The detected OCT signal was acquired using the A/D acquisition card aforementioned. Overall, this system allows ultrahigh speed OCT imaging with an axial resolution of ~8 μm (in tissue), an imaging range of ~2.4 mm (in tissue), and a detection sensitivity of ~101dB. In the sample arm, a customized patient interface unit (PIU) was used to connect the imaging catheter and translating the imaging catheter longitudinally via a high precision translational motorized stage inside the PIU (Parker, CA).

2.2.2 360-degree micromotor imaging catheter

Figure 2.2 shows the schematic diagram of the 360-degree unobstructed micromotor imaging catheter. As shown in Fig. 2.2(a), a DC brushless, hollow shaft micromotor (DBL024-05, Namiki Precision, CA) was used, enabling 360-degree unobstructed OCT imaging at a frame rate of >100 fps. The hollow shaft micromotor has an outer diameter (OD) of 2.4 mm and a rigid length of 5 mm (6.35 mm, if including a 1.35 mm distal extrusion of the central shaft). The inner diameter (ID) and length of the central shaft are 0.55 mm and 6.35 mm, respectively. Details on the specification of the electrical properties of the hollow shaft motor and a conventional 2 mm micromotor (SBL02-06, Namiki Precision, CA) used in our group's previous studies [133] served as the benchmark were summarized in Table 2.1.

Due the small size of individual components, a customized brass housing was used to facilitate the centering, alignment, and mounting of the torque coil (2.2 mm OD, Asahi Intecc, CA), hollow shaft micromotor, and a 1.4 mm OD optical focuser (10.5 mm working distance, Go!Foton Corp., NJ). In addition, a small customized micro prism (40-90-50 degrees, 1 mm length, Shanghai Optics, China) was used to deflect light transmitting from the optical focuser and propagating through the central shaft of the micromotor subsequently toward the tissue surface. To facilitate the assembly process, a prism holder encapsulating the prism was attached the distal end of the motor shaft. The angle of the prism was specifically designed to avoid specular reflection from the fluorinated ethylene propylene (FEP) plastic sheath (AWG 9, 3 mm ID, 3.4 mm OD, Zeus Industrial Products, SC) outside the imaging catheter. The focused spot size was ~28 μm (FWHM) at a distance of ~900 μm beneath the tissue surface. As shown in Figure 2.2, this design further simplifies the assembly process and most importantly enables an unobstructed imaging along the circumferential/rotary direction.

Here, the specification of the optical focuser was specifically designed to optimize the focused spot size and the throughput of light propagating through the central shaft at a given working distance, with respect to the rigid length of the imaging catheter. Figure 2.3 shows the simulated optical beam size ($1/e^2$ diameter) as a function of the distance from the exit lens surface and the designated focused spot size based on Gaussian beam optics. Due to the limitation on the central shaft ID (550 μm), a small focused spot size yields a large beam diameter at the proximal end of the motor shaft, resulting in a decreased light throughput after the micromotor. Therefore, a focused spot size of ~28 μm (FWHM), yielding to a beam diameter of <240 μm (FWHM) at the proximal end of the motor shaft was used. In addition, the beam tilt of light transmitting from the optical focuser was set close to zero to facilitate the alignment and a constant light throughput when the motor rotates. Although the beam diameter can be further decreased to facilitate the alignment of light propagating through the shaft, the increased focused spot size might prohibit the capability of visualizing fine architectures within the tissue specimen. The overall measured light throughput (transmission ratio) of the imaging catheter was >80%.

In this study, the motor rotation speed was set as 12,000 revolutions per minute (rpm, equivalent to a frame rate of 200 fps) to avoid applying a high driving voltage on the micromotor

itself and hence damage/degrade the performance/lifetime of the micromotor (Table 2.1). The designated motor speed yielded a sampling interval of ~3.6 μm per Ascan, which is ~4 times Nyquist sampling along the circumferential/rotary direction. The pullback speed of the imaging catheter was 1 mm per second (mm/s), resulting in a 5 μm sampling interval between sequential OCT frames (~3 times Nyquist), which is crucial for the generation of OCTA imaging. Each volumetric OCT dataset imaged a surface area of 10 x 18 mm^2 in 18 seconds, comprising 3000 x 3600 Ascans (rotary x pullback). Fig. 2.2(b) shows the photograph of the distal end of the 360-degree micromotor imaging catheter.

2.2.3 Non-uniform rotation distortion correction

Due to the small size of the motor, a feedback control was not possible for the hollow shaft motor used in the 360-degree micromotor imaging catheter. Therefore, it is expected the presence of residual NURD in the OCT images and requires a correction algorithm to remove or suppress the NURD in the OCT images. Figure 2.4 shows the cross-sectional OCT images of (a) human finger and inner cheek as well as (b) rectum where no imaging field obstruction due to either motor electric wirings or metal housing struts was observed. Our group previously demonstrated the use of metal strut edges in the cross-sectional OCT images as fiducial markers to measure the instantaneous rotational speed of the micromotor to develop an NURD correction algorithm [137]. These locations were used to cubic spline resample the OCT data, such that the pixels in the transverse direction were spatially equally spaced. However, as shown in Fig. 2.4, no metal strut edges can be identified in the OCT images and thus an alternative method to measure the instantons motor speed needs to be developed.

Recently, our group successfully demonstrated the use of multiple regions of interest (ROIs) within individual OCT frames to measure the instantaneous motor speed as an extension to the original method using the metal strut edges [140]. In this method, individual cross-sectional OCT images were divided into multiple ROIs with an identical number of Ascans. Then, the relative of shift of the middle Ascan in individual ROIs between adjacent frames was computed by calculating the cross-correlation similar to those demonstrated previously [141] but on a sub-pixel level [142]. Rotational speeds for all transverse pixels were then estimated by applying a cubic spline interpolation to the rotation speed of the ROIs (the motion trace). Finally, a cubic

spline resampling was applied to the OCT data to produce an equal spacing between the transverse pixels. The same subpixel, cross-correlation based correction algorithm was used in this study to suppress the NURD in the OCT images. As shown in Figs. 2.4(a, b), multiple ROIs (red dashed box) were selected within the OCT frames and used to estimate the instantaneous rotation speed following the same algorithm described above [140]. Here, in particular, the motion trace of individual ROIs was manually examined afterward to remove those exhibiting slowly varying motion components such as the varying catheter-tissue contact due to the physiological motion prior to cubic spline interpolation step.

2.2.4 Endoscopic OCT angiography (OCTA) and data visualization

Before calculating the intensity decorrelation (D) between sequential OCT frames to identify the motion contrast from the moving erythrocytes within the microvascular network, an NURD correction algorithm was performed to remove or suppress the NURD exhibited in the volumetric OCT datasets (section 2.2.3). Then, the intensity decorrelation was calculated pixel-by-pixel between sequential NURD-corrected cross-sectional OCT frames in linear OCT signal intensity scale, following the formula listed below where A_n is the OCT signal amplitude.

$$D_n(x,z) = 1 - \frac{A_n(x,z)A_{n+1}(x,z)}{1/2\left[A_n^2(x,z) + A_{n+1}^2(x,z)\right]}. \qquad (1)$$

After the decorrelation calculation, a moving average of three consecutive decorrelation images was taken to suppress the background decorrelation noise. Finally, a threshold mask was applied to the averaged cross-sectional OCTA images to remove regions with low OCT signal where the OCTA data is invalid [118, 121, 137, 140].

Prior to generating the depth-resolved *en face* OCT and OCTA images, the surface of the plastic sheath in the NURD corrected OCT images were identified using a graph cut, automatic segmentation algorithm [143]. Individual cross-sectional OCT and OCTA images in the volumetric OCT and OCTA dataset were shifted radially with respect to the plastic sheath identified to generate surface flattened volumetric OCT and OCTA datasets, respectively afterward. The depth resolved *en face* OCT and OCTA images were computed by using a mean projection over a 50 and 100 μm window at various depth level beneath sheath surface,

respectively. For example, an *en face* OCT image at 200 μm below sheath surface was the mean projection of the OCT signal intensities from 176 to 225 μm below sheath surface. The *en face* OCT images were displayed using square root compression gray scale and cross-sectional OCT images were displayed using logarithmic gray compression scale. *En face* OCTA images were displayed in a linear gray scale. Here, the black color corresponds to a low signal level while white color as a high signal (inverted gray scale).

2.3 Results

2.3.1 NURD characterization

Figure 2.5 shows the NURD characterization of the 360-degree micromotor imaging catheter based on the measurement of 100 continuously acquired cross-sectional OCT images of human fingers. Noted that these images were acquired without pulling back the imaging catheter. Figure 2.5(a) shows the characteristic layered architectures of the human finger including epidermis and dermis. As described in section 2.2.3, multiple ROIs with an identical number of Ascans within individual frames were used to measure the instantaneous motor speed (red dashed box, Fig. 2.5(a)). Figure 2.5(b) shows the angular deviation of the shift of the middle Ascan of one ROI in Fig. 2.5(a). Compared to the same measurement using a micromotor catheter wth a conventional 2 mm OD, DC brushless micromotor (SBL02-06, Namiki Precision, CA) as shown in Fig. 2.5(c), the NURD was more severe in the 360-degree micromotor imaging catheter. Given a 3.4 mm catheter OD (including the plastic sheath), the standard deviation of the angular deviation was 113.4 μm (66.7 milliradians (mrad)), which is worse than 11.6 μm (6.8 mrad) of the conventional micromotor. The NURD performance of the 360-degree micromotor catheter makes it difficult to completely remove or suppress the NURD in the OCT images and enabling endoscopic OCTA with low decorrelation noise.

2.3.2 Human skin and buccal mucosa imaging

Figure 2.6 shows the coregistered *en face* OCT and OCTA images of the human finger and inner cheek (oral mucosa). The *en face* OCT and OCTA images were reconstructed from the surface flattened, NURD-corrected volumetric OCT and OCTA dataset at a depth of 260 μm beneath the tissue surface, which is within the epidermis and epithelium layer (EP) of the skin (finger) and

oral mucosa (inner cheek), respectively. Characteristic architectural features of sweat duct (red arrows) and the epidermis ridge in the skin can be identified (Fig. 2.6(a)). The EP layer in the oral mucosa (inner cheek) is characterized by a relatively homogeneous appearance. A pattern comprising straight lines due to the delayed translation of the imaging catheter can be observed on the left portion of the *en face* OCT image. In the coregistered *en face* OCTA images, a rich of fine microvascular network representing the microvasculature perfusing from the underlying LP layer to the superficial EP layer can be observed over the region corresponding to oral mucosa part. However, over the skin region, no OCTA signal representing the microvasculature within the epidermis can be observed, which might be related to the pressure exerted on the skin surface while trying to position the catheter over the inner cheek. In addition, bright lines (high decorrelation signal) because of the residual NURD can be observed. Nevertheless, Figure 2.6 shows unobstructed coregistered *en face* OCT and OCTA images of the human skin and inner cheek tissue over a surface area of 10 x 10 mm^2.

2.3.3 Human lower GI tract imaging – dentate line

Figure 2.7 shows the OCT and OCTA images of a normal rectal-anal junction (RAJ, dentate line). The dentate line separating rectum (columnar epithelium) and anal verge (squamous epithelium) can be delineated based on the difference in the subsurface structural features in the *en face* OCT image at a depth of 280 μm (Fig. 2.7(a)). Tissue folds over the anal verge can be observed as well. Figure 2.7(b) shows the cross-sectional OCT image along the pullback (longitudinal) direction indicated by the blue dashed-dotted line in Fig. 2.7(a). The difference in the tissue architectures between the rectum and the anal verge, which exhibited layered features the same as Fig. 2.4(a) can be identified. Figure 2.7(c) shows coregistered *en face* OCTA image of the *en face* OCT image (Fig. 2.7(a)) at the same depth (280 μm below tissue surface). A honeycomb-like microvascular pattern can be observed over the rectum side (arrows, Fig. 2.7(c)) reminiscent the surface mucosal pattern of rectum crypts. By contrast, an intricate microvascular network (diamond arrows, Fig. 2.7(c)) corresponding to the microvasculature within the LP layer of the squamous epithelium was identified. However, due to the presence of residual NURD in the motion corrected volumetric OCT dataset, regions exhibiting high decorrelation noise (stars) can be identified in the imaging field.

2.4 Discussion

There existed several limitations in conventional proximally actuated catheters. First, the NURD presented in the OCT images becomes exacerbated if endoscopic imaging involved organs with complex geometry. In addition, in the proximal actuation scheme, an FORJ is required to couple light while continuously providing rotary torque transmission to the catheter. However, the light transmission ratio/throughput of the FORJ is relatively low in general (~80% coupling efficient typically). In addition, the maximum rotation speed and stability of the FORJ are very sensitive to the balance of moment of inertia inside the FORJ. Although studies have demonstrated a frame rate of 500 fps using an in-house developed FORJ, it requires customized machining components and careful management of inertia balance while preserving the mechanical strength of the FORJ unit [144]. Furthermore, the optical bandwidth of the FORJ is ultimately limited by the chromatic aberration presented in the optical coupling components inside the FORJ, which is more sensitive in the 800 nm wavelength regime compared to 1300 nm [145]. This also complicates the setup to perform multimodality imaging. Lastly, in proximally actuated imaging catheters, the fiber was continuously rotated and might be twisted during the imaging session, which alters the polarization state of the illumination beam over the tissue surface. The varying polarization state of the illumination beam will introduce polarization artifacts in the OCT images, requiring the implementation of polarization diversity detection to remove the artifacts.

In comparison, a low NURD performance has been reported in the endoscopic OCT system using micromotor imaging catheters compared to proximally actuated catheters [136, 137]. In addition, studies have demonstrated all fiber-optic simultaneous OCT and fluorescence imaging using micromotor imaging catheter without requiring high-performance dual clad fiber FORJ [135]. Lastly, the fiber stays stationary during the imaging session, which minimizes the variation of the polarization state of the illumination beam during the imaging session and the presence of polarization artifacts in the OCT images, which might be a better platform to perform endoscopic polarization-sensitive OCT imaging as demonstrated by our group recently [146]. However, the motor electric wiring shadowing reduces the field of view along the circumferential or rotary direction, which is limited by the scanning mechanism of conventional micromotors.

In this study, we developed a novel micromotor imaging catheter enabling 360-degree unobstructed imaging over the circumferential or rotary dimension, free from the motor wiring shadowing over a surface area of 10 x 18mm^2. Leveraging the unique scanning mechanism of the new hollow shaft brushless micromotor, the assembly process of the micromotor imaging catheter can be significantly simplified. This unobstructed circumferential imaging, more importantly, promises to further simplify the imaging procedure using a small size micromotor catheter which requires aligning the imaging window toward the ROI prior to the imaging acquisition to maximize imaging coverage. This alignment procedure makes the imaging session prolonged and might affect the yield of the OCT imaging. Although the concept of the hollow shaft motor has been demonstrated before with the PZT squiggle motors, no complex mirror head cap synchronous to the screw shaft is required. In addition, the driving voltage for the brushless hollow shaft motor is much lower compared to PZT squiggle motor. Lastly, the new catheter employs a "collimated" beam design (using long working distance focuser) to transmit light through the central shaft rather than conventionally positioning the fiber inside the central shaft, which makes the imaging vulnerable to the vibration of the optical fiber during the motor rotation. Also, the insertion loss in the fiber design is sensitive to the cleaved angle of the fiber terminal. Furthermore, the "collimated" beam design is an ideal platform for endoscopic optical coherence microscopy (OCM) imaging inside the luminal organs where an objective lens with desired focusing power can be attached to the distal mirror cap.

However, there existed several limitations in the current version of the 360-degree micromotor imaging catheter. First, as shown Table 2.1, the rotation torque of the brushless hollow shaft micromotor is lower compared to the conventional 2 mm OD micromotor (0.23 vs. 0.314 mNm/A). Therefore, a higher driving voltage is required to achieve a rotation speed of 6,000 rpm (100 fps). The driving voltage needs to be further increased to achieve an even higher rotation speed, which leads to a high electric power consumption because of the low terminal resistance of the hollow shaft motor itself. In particular, the high power consumption generates heat over the coil and affects the lifetime of the motor. Therefore, in this study, a motor speed of 12,000 rpm (200 fps) was used to avoid overheating and hence damaging the motor. As a result of the scanning mechanism, the wiring characteristic inside the brushless hollow shaft motor such as the number of turns, wire diameter, and the coil material were different from those of the

conventional micromotors to achieve the desired performance. Since this is the first generation of the brushless hollow shaft motor, future improvements on the performance of the micromotor are warranted to enable a comparable scanning performance as conventional small size micromotor catheters.

In addition to the limited rotation speed due to the high power consumption, the NURD presented in the OCT images was worse compared to the conventional 2 mm micromotors. The NURD performance might be related to the limited torque and scanning mechanism of the motor. In this study, a motion correction algorithm based on the extension from the existing algorithms developed in our group's recent studies. After applying the correction algorithm, the NURD exhibited in the volumetric OCT images were suppressed and thus enabled OCTA imaging. However, as shown in Fig. 2.7(c), regions showing high decorrelation noise because of residual NURD can be observed. In the current version of the motion correction algorithm, the OCT images were divided into multiple small ROIs, and the shift of individual ROIs between sequential frames was calculated based on the cross-correlation computation at a subpixel level. The accumulated shift of individual ROIs in the consecutive OCT frames was used to measure the instantaneous rotation speed. However, small errors might generate during the calculation, for example, the varying the catheter-tissue contact and distort the images in the end. The method used in this study may not be optimal, but demonstrate the feasibility of the new 360-degree micromotor imaging catheter. As discussed previously, future improvements on the design of the motor itself as we as the motion correction algorithm need to be performed to validate its optimal imaging performance over conventional micromotor catheters.

2.5 Figures

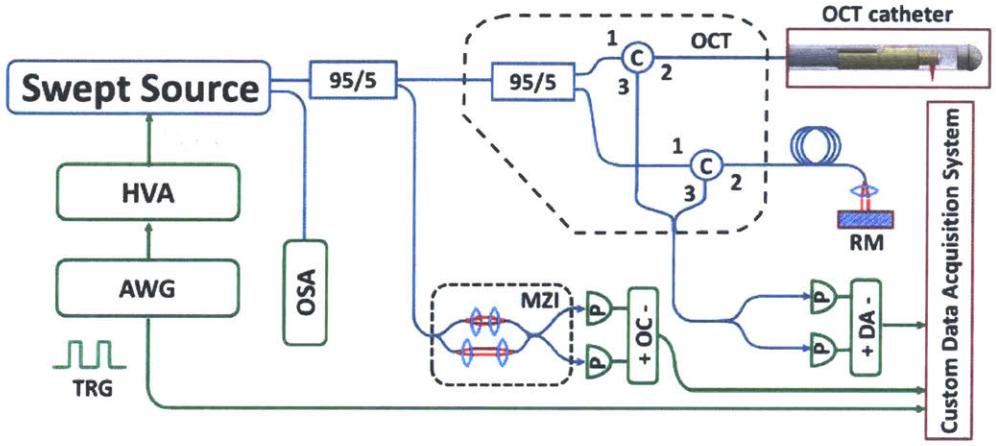

Figure 2.1. Schematic of the ultrahigh speed endoscopic OCT system. HVA: high voltage amplifier; AWG: arbitrary waveform generator; OSA: optical spectrum analyzer; MZI: Mach-Zehnder interferometer; C: circulator; P: photodetector; OC: optical clock generator, DA: differential amplifier; RM: reference mirror; TRG: trigger signal.

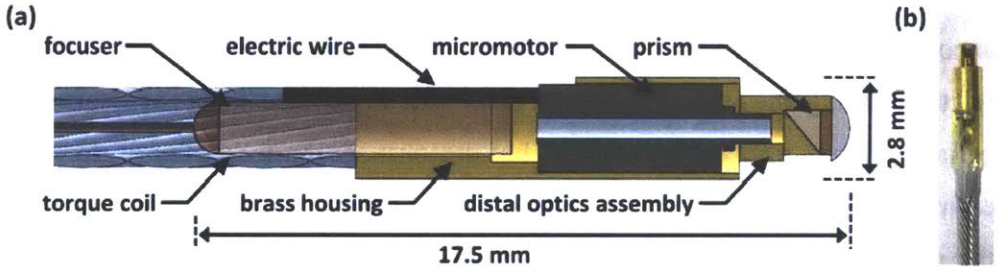

Figure 2.2. 360-degree unobstructed micromotor imaging catheter. (a) Schematic and (b) photograph of the distal end of the 360-degree micromotor imaging catheter.

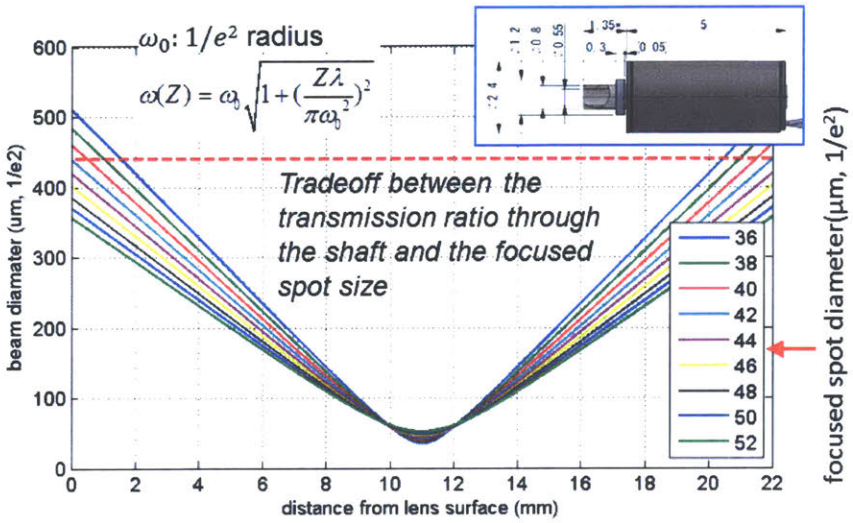

Figure 2.3. Optical beam size as a function of the distance with respect to the exit lens surface and focused spot size designated. Inset: schematic of the brushless hollow shaft micromotor listing the aspect measures of the motor itself (courtesy of Namiki Precision, CA).

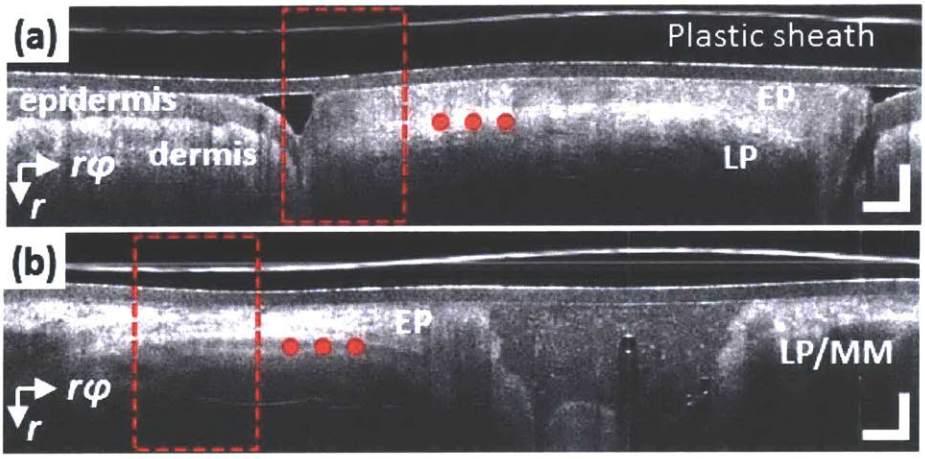

Figure 2.4. Cross-sectional OCT images of (a) human finger/inner cheek and (b) rectum acquired using the 360-degree micromotor imaging catheter. Individual cross-sectional OCT frames were divided into multiple regions of interests (ROIs) and used to estimate the instantaneous rotation speed of the motor. The imaging artifacts due to nonuniform rotation distortion were removed afterward. rφ: circumferential (rotary) direction; r: radial (axial) direction. Scale bars: 500 μm. EP: epithelium; LP: lamina propria; MM: muscularis mucosa.

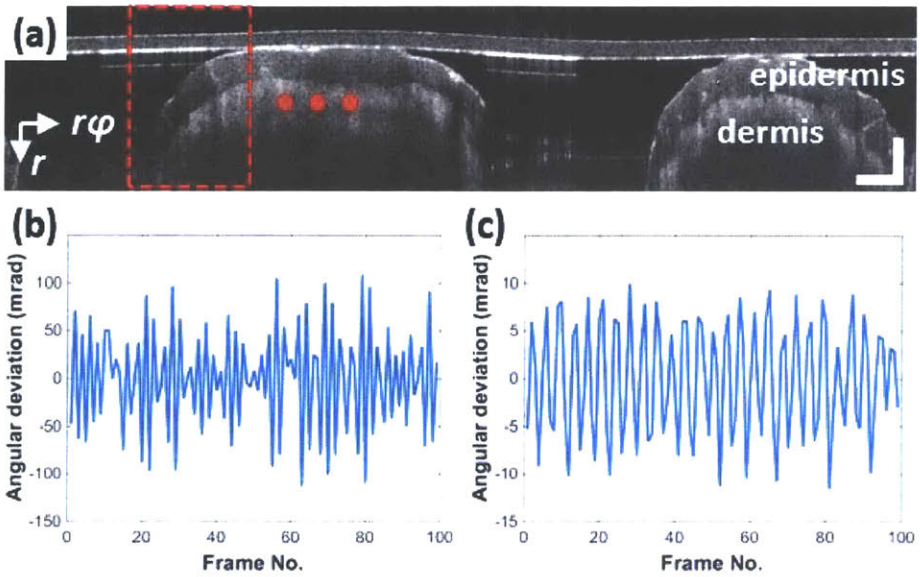

Figure 2.5. Characterization of the NURD exhibited in the 360-degree micromotor imaging catheter. (a) Multiple regions of interest (ROIs) was selected in the cross-sectional OCT images to measure the NURD exhibited in the 360-degree micromotor imaging catheter. (b, c) Temporal traces showing the angular deviation of one ROI or fiducial marker from 100 consecutive frames acquired at a frame rate of 200 fps using 360-degree and conventional micromotor catheters, respectively. rφ: circumferential (rotary) direction; r: radial (axial) direction. mrad: milliradians. Scale bars: 500 μm.

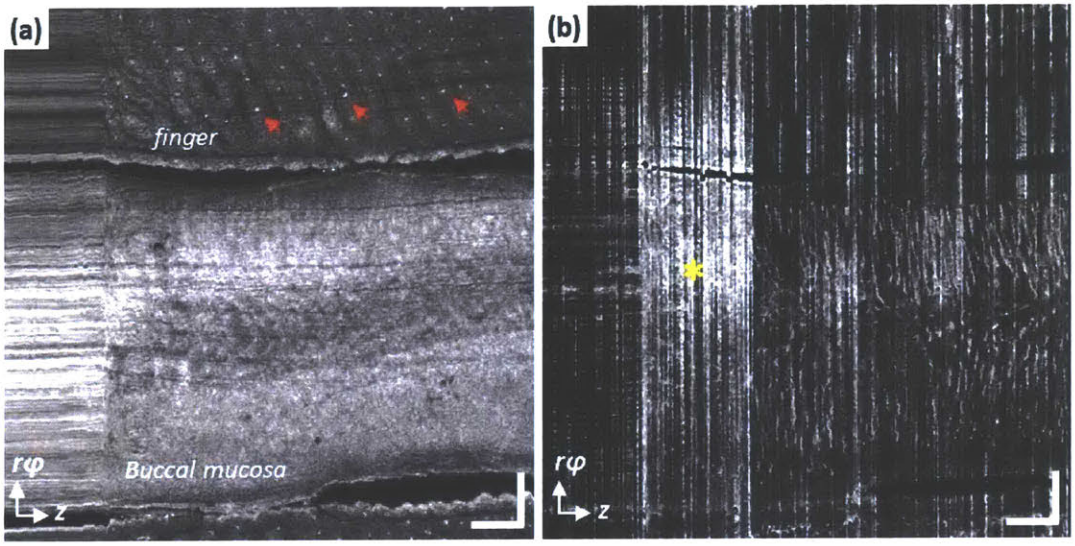

Figure 2.6. Coregistered *en face* (a) OCT and (b) OCTA images of the human finger and inner cheek reconstructed from the NURD-corrected, surface flattened volumetric OCT and OCTA dataset, respectively at a depth of 260 μm beneath the tissue surface. rφ: circumferential (rotary) direction; z: longitudinal (pullback) direction. Scale bars: 1 mm. Red arrows: sweat ducts.

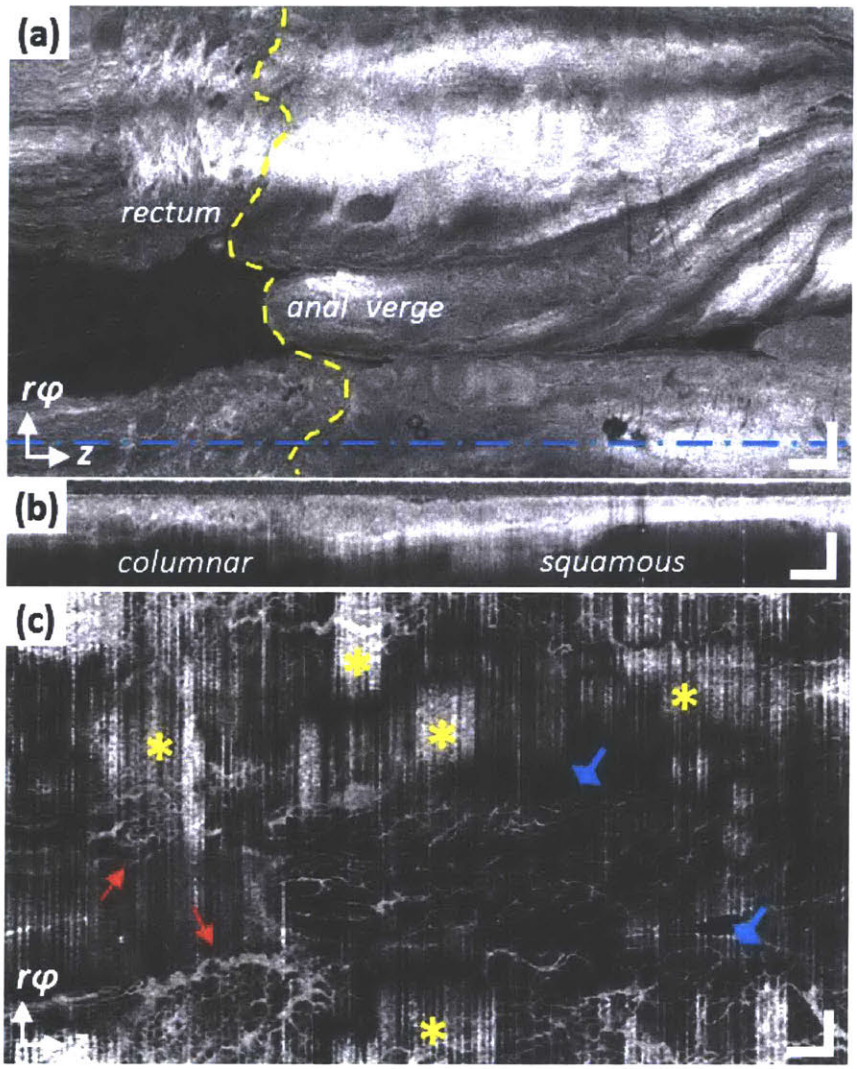

Figure 2.7. OCT and OCTA images of the normal rectal-anal junction (RAJ). The architectural difference between the rectum (columnar epithelium) and anal verge (squamous mucosa) can be identified in the (a) *en face* OCT image at 280 μm beneath tissue surface and (b) cross-sectional OCT image along the pullback direction, corresponding to the indicated location in (blue dashed-dotted line, a). (c) Coregistered *en face* OCTA image at the same depth as (a) where a characteristic microvascular feature of the normal rectum and anal verge, as well as high decorrelation noise (stars) due to residual NURD, can be observed. Red arrows: honeycomb-like microvascular pattern over the rectum. Blue diamond arrows: intricate microvascular networks within the LP layer squamous mucosa in the anal verge. Scale bars: (a, c) 1 mm; (b) 0.5 mm (axial) and 1 mm (lateral).

2.6 Tables

Table 2.1. Specification of the conventional brushless micromotor (SBL02-06) and the new brushless hollow shaft micromotor (DBL024-05) actuated with 3-phase driving signals.

	DBL024-05	SBL02-06
terminal resistance (ohm, measured)	101.4	131.1
terminal driving voltage (Vamp, volts)	2.4	1.2
terminal current (mA)	23.67	9.15
torque constant (mNm/A, nominated)	0.23	0.314
Power consumption (mW, i.e. heat)	56.80	10.98
Motor outer diameter (mm)	2.4	2

Note: the terminal driving voltages were characterized with a motor speed of 6000 revolutions per minute.

CHAPTER 3

3.0 Circumferential Optical Coherence Tomography Angiography using a Micromotor Balloon Catheter

3.1 Motivation

Using fiber-optic scanning catheters, *in vivo* endoscopic OCT imaging of the human gastrointestinal (GI) tract was demonstrated by several groups over a decade ago [73, 74, 84]. Although the fiber optic catheters in these studies were small enough to pass through the accessory port of an endoscope, imaging coverage was very limited. To increase the coverage, an OCT balloon imaging catheter was first proposed in 2000 [84] and subsequently demonstrated in living swine and human esophagus [104, 120]. In contrast to positioning a small diameter imaging catheter over quadrants of the esophageal surface, the balloon catheter allows full circumferential imaging by centering the optics and expanding the esophageal lumen. Circumferential beam scanning was originally implemented with proximal rotary actuation transmitted by a torque cable housing the optical fiber. Later studies demonstrated an optical design using miniature compound gradient-index rod lenses to achieve a small focused spot size (~39 μm, full width at half maximum (FWHM)) at a ~9 mm working distance [147]. In addition, high resolution balloon OCT imaging was achieved by correcting astigmatism from the plastic sheath with a cylindrical aluminum reflector [148]. An alternative double balloon sheath design was proposed to allow endoscopic OCT imaging of the esophageal mucosa either with or without direct balloon contact to the tissue [149].

Volumetric *en face* OCT imaging enables rapid examination of mucosal surface patterns similar to conventional white light endoscopy (WLE) which are known markers of GI neoplasms [150] but with the ability to visualize subsurface features [87, 100]. However, limited imaging speed and instabilities in conventional proximal actuation scanning make images vulnerable to motion artifacts and nonuniform rotational distortion (NURD). Therefore, volumetric *en face* OCT is challenging with endoscopic OCT systems that use a proximally actuated catheter, especially in balloon catheters which have long working distances that increase the effects of scanning instability. NURD in OCT images can be significantly reduced using catheters with distal actuation scanning such as micromotors [131, 151]. Recently, our group demonstrated ultrahigh speed endoscopic OCT using an MEMS-tunable vertical-cavity surface-emitting laser (VCSEL) light source and a micromotor imaging catheter in the rabbit [152] and human GI tracts *in vivo* [121]. The VCSEL light source enables ultrahigh speeds with MHz A-scan rates [152,

153] while the micromotor enables imaging at a high frame rate with minimal NURD [134, 154], which can be further corrected using fiducial based, non-rigid registration algorithms [137].

OCT angiography (OCTA) has been demonstrated to visualize three-dimensional (3D) vascular network using the Doppler effect to isolate blood flow from the static tissue [111, 112]. OCTA was later performed using motion contrast, by calculating the amplitude, phase, or complex amplitude variation of the OCT signals between neighboring B-scan frames [113]. Utilizing the ultrahigh imaging speed provided by VCSEL light sources and precision distal rotary scanning micromotor catheters, our group demonstrated OCTA imaging of 3D microvasculature in the human GI tract [121]. However, the imaging field of the micromotor catheter was limited by its small circumference, which made it difficult to survey large regions of the esophagus. Therefore, it is desirable to have an imaging technology for wide field, circumferential OCT and OCTA imaging of the esophagus.

In this study, we have developed a micromotor balloon imaging catheter to provide circumferential structural and angiographic imaging of the esophagus using an ultrahigh speed endoscopic OCT system. The OCT system has a 1.2 MHz A-scan rate and a ~8.5 μm axial resolution in tissue using a 1310 nm wavelength MEMS tunable VCSEL light source. The micromotor balloon catheter provides volumetric OCT imaging of the esophagus over a 5 cm x 2.6 cm (circumference (rotary) x longitudinal (pullback)) area in <18 seconds. The micromotor enables precision rotary beam scanning at a frame rate of 240 fps. An improved NURD correction algorithm suppresses artifacts from the non-uniform micromotor scanning and physiological motion. The study demonstrates co-registered OCT and OCTA images of the swine esophagus *in vivo* as an important translational step toward human studies.

The portable ultrahigh speed OCT engine used in this study was developed based on the design of an ultrahigh speed endoscopic OCT system dedicated for clinical imaging as described in the previous chapter but modified for the laboratory imaging purpose, including endoscopic OCT imaging in the animal models. The OCT engine was built in a team effort between Kaicheng Liang, Osman Ahsen, Drs. Benjamin Potsaid, Zhao Wang, and Michael G. Giacomelli, and myself. Osman Ahsen and Kaicheng Liang participated the discussion of the design and

assembly of the micromotor balloon catheter as well as the development of the NURD correction algorithm. The performance of the micromotor balloon catheter was validated in collaboration with Dr. Giovanni Traverso, MD. PhD. at MIT. The endoscopic OCT imaging in the swine esophagus with the micromotor balloon catheter was performed with Dr. Traverso and Dr. Jennifer Haupt, DVM. and Morgan Jamiel from the Division of Comparative Medicine (DCM) at MIT as well as Kaicheng Liang, Osman Ahsen, Dr. Zhao Wang and myself from Professor Fujimoto's group. All the data processing and analysis were performed by the author of the thesis work.

3.2 Development of the Micromotor Balloon Catheter

3.2.1 Swept source OCT imaging system

Figure 3.1 shows a schematic of the ultrahigh speed endoscopic OCT system used in this study, similar to the system recently reported [152, 155]. A high speed, wavelength swept light source based on a 1310 nm MEMS-tunable vertical-cavity surface-emitting laser (VCSEL) was driven at 600 kHz to provide 1.2 MHz A-scan rate (bidirectional sweep) [152, 153] and an average output power of ~80 mW. The MZI output connected to a dual balanced clock generator (Thorlabs, Inc., NJ) to externally clock a 4 GSPS, 12 bit, A/D acquisition card (ATS 9370, AlazarTech, Quebec, Canada). The laser sweep range was ~115 nm, enabling OCT imaging with an axial resolution of ~12 μm in air (~8.5 μm in tissue) without spectral shaping and a Nyquist imaging range of ~1.6 mm in air (~1.2 mm in tissue) determined by the maximum MZI clock frequency of 1.1 GHz.

The sample arm of the OCT interferometer included a custom 3D-printed patient interface unit (PIU) to connect to the micromotor balloon catheter. A helical scan pattern was generated by pulling back the torque cable inside the balloon sheath. The incident power on the tissue surface from the balloon imaging catheter was 38 mW, within the ANSI standard for skin exposure. The OCT system sensitivity was measured to be ~102 dB using an isolated reflection from a flat cleaved fiber with calibrated attenuation.

3.2.2 Micromotor balloon imaging catheter

Figure 3.2(a) shows the schematic diagram of the micromotor imaging catheter, similar to previously published designs [152] but modified to extend the working distance for a balloon. The distal optics of the imaging catheter were comprised of two separate parts: a 2 mm outer diameter (OD) brushless DC micromotor (Namiki Precision, CA), and an optical focuser consisting of a 1 mm OD fiber pigtail/ferrule and a plano-convex lens (1.5 mm OD, 2 mm focal length, Edmund Optics, NJ) with an 11 mm working distance. A custom machined brass housing (Kroll Technologies, PA) housed and encapsulated the distal end components, which featured a three-strut design [156] with a ~20° circumferential extent for each strut to provide sufficient mechanical strength while achieving large (~300°) field of view (FOV). Individual struts were separated by 120° along the circumference. A 45°, 1 mm microprism (Tower Optical, FL) was slightly tilted and mounted on the micromotor shaft to deflect the optical beam by <90° towards the tissue while avoiding specular reflection. The focused spot size was ~30 μm (full width at half maximum, FWHM in air). A 2 m long torque cable (2.2 mm OD, Asahi Intecc, CA) was used to connect the distal optics assembly. The rigid length and OD of the micromotor catheter was ~16 mm and 2.6 mm, respectively.

The balloon sheath included a 16 mm OD (~5 cm circumference), 40 mm length, ~55 μm thick polyethylene terephthalate (PET) balloon (Vention Medical, NH) at the distal end of a plastic sheath as shown in Fig. 3.2(b). The proximal neck of the balloon was removed to fit the OD of the plastic sheath (Zeus Industrial Products, SC), consisting of two polytetrafluoroethylene (PTFE) tubings. The inner PTFE sheath (AWG 9, 3 mm ID, 3.4 mm OD) allowed the micromotor imaging housing to translate within the sheath and perform a helical scan pattern with minimal friction. The space between the inner and outer PTFE sheath (AWG 7, 3.8 mm ID, 4.2 mm OD) was used to inflate/deflate the distal balloon. This design combines reusable micromotor imaging catheters and disposable balloon sheaths and thus provides a cost-effective solution. In this study, the micromotor rotation speed was set at 14,400 RPM (240 fps) to ensure a sampling interval of ~10 μm per A-scan, ~1.5 times Nyquist sampling along the circumferential direction. The pullback speed of the micromotor imaging catheter was 1.5 mm/sec, resulting in a 6 μm sampling interval between frames (~2.5 times Nyquist). High-density sampling along the pullback direction was essential to perform endoscopic OCTA, which

will be described in section 3.2.4. The total acquisition time for each 3D-OCT dataset (5000 x 4200 A-scans) was <18 seconds, which corresponds to a volume size of 50 mm x 26 mm x 1.2 mm (rotary x pullback x axial direction) in tissue. Figure 3.2(c) shows a photograph of the distal end of the micromotor balloon imaging catheter.

3.2.3 Nonuniform rotation distortion (NURD) correction

The micromotor imaging catheter does not require proximal rotation via the torque cable and can be actuated at higher rotational speeds. The micromotor catheter exhibits significantly improved NURD performance compared with proximal rotary scanning [137, 141, 157]. Using a fiducial based correction algorithm, residual NURD in the OCT images can be corrected [137]. However, in the current study, the increased radius of the micromotor balloon catheter compared with a small micromotor catheter exacerbated the effect of rotary scanning instability. In addition, physiological motion (e.g. respiration or cardiac beating) near the GI tract introduced artifacts when using a balloon catheter [141]. Therefore, fiducial based correction registration was insufficient.

Figure 3.3 shows the cross-sectional OCT images of the swine esophagus using the micromotor balloon catheter displayed in polar (unwrapped) coordinates. The FOV was split into three zones (~100° FOV each) by brass housing struts (yellow box). The rotary (circumferential) direction is labeled as $r\varphi$, indicating the scaling of this direction, and the radial (axial) direction is labeled as r in the cross-sectional OCT images. The characteristic layered architecture of squamous mucosa can be observed (Figs. 3.3 (a) and (b)). Our previous method used the metal strut edges in the cross-sectional OCT images as fiducial markers to measure the instantaneous rotational speed of the micromotor [137]. These locations were used to cubic spline resample the OCT data, such that the pixels in the transverse direction were spatially equally spaced. In this study, we extended this algorithm to measure the instantaneous rotational speed using multiple ROIs within the frames. The ROIs were selected at the three metal strut locations (e.g. yellow boxes, Fig. 3.3), as well as the tissue structures in individual zones (e.g. red boxes, Fig. 3.3) in the cross-sectional OCT images. In general, at least two ROIs were selected from the locations of individual metal struts, which accounts for >6 ROIs per cross-sectional OCT image. However, the number of ROIs corresponding to the tissue structures might vary between different 3D-OCT

datasets, depending on the catheter-tissue contact with the balloon catheter and OCT signal quality. For example, as shown in Fig. 3.3(a), the tissue contact was good in all three zones. Thus, ~14 ROIs were selected from the three zones in total. Conversely, the tissue contact was limited in one of the zones in Fig. 3.3(b). Therefore, only ~10 ROIs were selected from two zones with tissue contact in Fig. 3.3(b). Selection of the ROIs was performed manually in this study by loading a representative frame and selecting regions with good tissue contact and low specular reflections. For regions where the tissue contact varied rapidly, the measurement of instantaneous rotation speed might be confounded by tissue motion such as the esophageal tissue sliding over the balloon surface. Specular reflections were sensitive to alignment of the OCT beam and balloon surface and were not reliable enough as a fiducial marker to estimate NURD. However, this process can be automated by employing segmentation algorithms.

After selection of ROIs, the instantaneous rotational speed at each ROI is measured by calculating the cross-correlation of individual ROIs between sequential cross-sectional frames. The algorithm calculates the transverse shift-translation between individual ROIs on a sub-pixel level [142]. Rotational speeds for all transverse pixels were then estimated by applying a cubic spline interpolation to the rotational speeds of the ROIs. Finally, a cubic spline resampling was applied to the OCT data to produce equal spacings between the transverse pixels. This method allows estimation of rotational velocity at multiple locations within the frames (not only strut locations), improving motion correction accuracy. Furthermore, using ROIs on the tissue as the fiducial markers also corrects for artifacts caused by physiological motion [141]. However, the disadvantage is that sequential frames need to be highly oversampled to enable calculation of the cross-correlations. Also, this method will not correct for motion which is perpendicular to the image plane. The NURD-correction algorithm described here is a subset of more general non-rigid image registration algorithms. Many of these algorithms estimate a displacement field (circumferential displacements for all A-scans in an image) by maximizing the similarity between images while penalizing motion. We expect that a fully automated algorithm with improved performance should be possible using more advanced, non-rigid registration methods [158].

3.2.4 Endoscopic OCT angiography and data visualization

Prior to calculating the intensity decorrelation between consecutive cross-sectional OCT images, the non-rigid registration algorithm (section 3.2.3) was applied to generate NURD-corrected 3D-OCT datasets. Then, intensity decorrelation between sequential registered cross-sectional OCT images in linear OCT signal was calculated to generate cross-sectional OCTA images (decorrelation images) as described in detail in section 2.2.4 in Chapter 2. Depth resolved *en face* OCT and OCTA images were generated from the surface aligned/flattened NURD-corrected 3D-OCT and 3D-OCTA datasets using mean projection over a depth range of 50 μm at various depth levels beneath the tissue surface. *En face* OCT images were displayed using square root compressed grayscale, while the cross-sectional OCT images were displayed using logarithmic grayscale. *En face* OCTA images were displayed using a linear gray scale.

3.2.5 Animal imaging procedures

OCT imaging was performed under a protocol approved by the Committee on Animal Care (CAC) at the Massachusetts Institute of Technology. Two female Yorkshire swine weighing approximately 30 kg were imaged in a single session. The anesthesia and sedation protocols are similar to previously reported [155]. Prior to the OCT imaging session, sedation was administered to each swine with an intramuscular injection of 5 mg/kg telazol and 2 mg/kg xylazine, and atropine at 0.04 mg/kg was given to maintain heart rate and minimize mucus secretion. Before introducing the micromotor balloon catheter, a 16.7 mm ID overtube (Guardus, US Endoscopy, OH) was placed using a dual channel, upper GI endoscope (EG-3830, Pentax Medical, NJ). Once the overtube was in place, the endoscope was withdrawn, and the micromotor balloon catheter was introduced through the overtube. The distal balloon was partially inflated (~10 psi) after the balloon catheter was positioned in the esophagus. Real time OCT imaging was used to confirm location in the upper GI tract. The endoscope was sometimes re-introduced to facilitate positioning the balloon catheter (Fig. 3.4(a)). X-ray images (Hudson Digital Systems, NJ) were also acquired to confirm positioning (red arrow, Fig. 3.4(b)). Once the catheter was positioned, the balloon was further inflated and maintained at a pressure of ~15 psi to improve the centering of the micromotor and optics in the lumen. After OCT imaging, the balloon was deflated prior to withdrawing the catheter from the esophagus.

3.3 Imaging Results

3.1 Demonstration of the NURD correction

Figure 3.5 shows results from the NURD correction algorithm for *en face* OCT and OCTA images of the swine esophagus. To highlight the improvements in contrast and quality, an enlarged region selected from the FOV (~13 cm^2) is shown. The standard deviation of the transverse shift of the individual ROIs between neighboring frames was ~7 milliradians (mrad, median, 56.3 μm in circumferential position for the 16 mm OD balloon). Figures 3.5(a, d), (b, e) and (c, f) show *en face* OCT and OCTA images of the lamina propria (LP) before and after applying the NURD correction algorithm using ROIs from the metal struts alone, and both the metal struts and tissue structures, respectively. The improvement was less evident in the *en face* OCT images if only ROIs from the metal struts were used for NURD correction as shown in the magnified view (2X, insets, Figs. 3.5(a-b)). The contrast in the *en face* OCT image was improved more after further including ROIs from the tissue structures in the NURD correction (Figs. 3.5(a, c)). In OCTA, NURD increases decorrelation noise (Fig. 3.5(d)). In addition, severe NURD between successive frames causes a spike in the OCTA decorrelation seen as a white line motion artifact in the *en face* OCTA images (Fig. 3.5(d)). The decorrelation noise, as well as the white line artifacts in the en face OCTA image, were decreased significantly or removed using the NURD correction algorithm with ROIs from both the metal struts and tissue architecture (red arrows, Fig. 3.5(f)). In addition, the contrast of the smaller vessels in the *en face* OCTA image was improved, enabling visualization of microvasculature that was hard to identify prior to applying the correction algorithm. A rich and intricate vascular network mixed with larger-sized vessels was identified in the LP (Fig. 3.5(f)).

3.2 Swine esophageal imaging

Figure 3.6 shows representative cross-sectional OCT images of the swine esophagus in both polar and Cartesian coordinates. The epithelium (EP), lamina propria (LP), muscularis mucosa (MM), and submucosa (SM) of the squamous mucosa were identified in the OCT images (Figs. 3.6(a, b)). Regions not fully in contact with the balloon surface were observed in the 12 and 6 o'clock locations in Fig. 3.6(b) where the contact level varied because of cardiac motion. The circumferential view (Cartesian coordinate) was displayed using a 4:1 aspect ratio. In the

magnified view (3X) of the ROI in the cross-sectional OCT image (Fig. 3.6(a)), detailed layered architecture of normal swine esophagus can be appreciated more clearly, along with the presence of small vessels (star mark, Fig. 3.6(c)). Figure 3.6(d) shows a 3D rendering of the esophagus. The circumferential FOV was decreased from 360 to 300 degrees due to the metal struts in the imaging catheter (red arrows, Fig. 3.6(b)). Shadowing from a large vessel was also observed (blue arrow, Fig. 3.6(d)).

Figure 3.7(a) shows the *en face* OCT image obtained using a mean projection from 75 to 125 μm below the tissue surface, corresponding to the EP layer, showing a homogeneous tissue composition. However, variation in catheter-tissue contact can be noted as an oscillating tissue boundary along the pullback/longitudinal direction (red arrows). The *en face* OCT images are displayed oriented with the top and bottom of individual images corresponding to the longitudinal direction from the proximal to distal end of the esophagus. Figure 3.7(b) shows the *en face* OCT image obtained by mean projection from ~225 to 275 μm below the surface showing the LP where shadowing from a large vessel is seen (blue arrows) along with an oscillating tissue boundary (red arrows) due to cardiac motion.

Figure 3.8 shows coregistered *en face* OCTA images at different depths. In Fig. 3.8(a), high decorrelation signal was observed where the tissue lost contact with the balloon. Debris in the space between the balloon and esophagus as well as tissue movement from cardiac motion generated high decorrelation (red arrows). Figure 3.8(b) shows *en face* OCTA images of the LP layer from a 225 to 275 μm mean projection below the tissue surface. The microvascular pattern in Fig. 3.8(b) is finer than in Fig. 3.7(b), where vasculature is seen because of shadowing effects. An intricate microvascular network can be appreciated across most of the visible FOV. In the region on the right, the increased decorrelation noise in the background might be due to the varying catheter-tissue contact from cardiac motion. About 14 oscillatory periods are seen in the decorrelation signal on the left in Fig. 3.8(a), consistent with the swine heart rate.

Figure 3.9 shows coregistered *en face* OCT and OCTA images of the distal esophagus including the gastroesophageal junction (GEJ) from ~250 μm (mean projection from 225 to 275 μm) below the tissue surface. Tissue contact was limited in the gastric region because the

esophagus opens into the stomach distal to the GEJ (Fig. 3.9(a)). In the region having reasonable catheter-tissue contact on the gastric side, contact was unstable and varied along the pullback direction (red arrows), possibly because of cardiac motion. At the GEJ, the effect of cardiac motion can be more pronounced than in regions away from GEJ, such as the middle esophagus. This motion made it challenging to identify gastric microvasculature because of insufficient tissue contact and increased decorrelation noise. However, if the catheter-tissue contact was sufficient, such as in the squamous epithelium near the GEJ, fine microvasculature can be observed from 250 μm (mean projection from 225 to 275 μm) beneath tissue surface (Fig. 3.9(b)) albeit with higher decorrelation noise compared to Fig. 3.8.

The cross-sectional OCTA image from the location highlighted in Fig 3.8(a) showed regions of high decorrelation signals from blood flow in the microvascular network. In addition, speckle decorrelation tails (OCTA projection artifacts) below the vessels were observed (red arrows, Fig. 3.8(c)). Artifacts from the volumetric data flattening operation were also present. Magnified views from the ROIs in Fig. 3.8(b) better visualized the intricate microvascular network in the LP (Figs. 3.8(d, e)). The size of the smallest vessels in the magnified views was ~40-50 μm diameter (blue arrows), close to the focused OCT beam size.

3.4 Discussion

Mucosal surface patterns have been widely investigated to detect regions of dysplasia in BE using several endoscopic imaging techniques including chromoendoscopy [150], narrow band imaging (NBI) [33], and confocal laser endomicroscopy (CLE) [36]. Although studies from expert imaging centers showed promising results with high dysplasia detection accuracy [35], data establishing widespread utility is still lacking. Chromoendoscopy requires the topical application of stains, a cumbersome procedure which might obscure the endoscopic view after contrast agent application. CLE also requires administration of contrast agents, typically IV fluorescein [36]. In addition, the imaging field is limited to $<0.1 mm^2$ with the probe-based CLE system, making it vulnerable to motion and difficult to assess large areas of pathology.

En face OCT allows rapid assessment of mucosal surface patterns, similar to conventional WLE, but with depth resolution. Our group recently demonstrated high contrast *en face* OCT

images of normal human esophagus and patients with BE and dysplasia, although the imaging coverage was limited to ~2 cm^2 using small micromotor catheters [121]. Recently, we also showed *en face* OCT images over a longitudinal extent of the esophagus in living swine using a micromotor capsule [155]. However, contact with the full esophageal circumference is challenging with capsule devices, and studies by other groups reported ≥50% tissue contact in 94% of the OCT images [159]. This might make capsule imaging more vulnerable to sampling errors than balloon catheters. In addition, balloon catheters can potentially pass through the accessory port of the endoscope as shown in current commercially available balloon based OCT systems. This facilitates the collection of co-registered biopsies or administration of endoscopic therapies in conjunction with OCT imaging.

Combining the merits of micromotor and balloon catheters, the technology demonstrated in the current study can provide volumetric cross-sectional and *en face* OCT images of the esophagus. *En face* OCT images of the swine esophagus with >90% coverage of esophageal circumference over a ~2.6 cm longitudinal extent were demonstrated. Cross-sectional and *en face* OCTA images can be obtained over a wide field of view, but require oversampling and therefore reduce the area coverage compared to structural OCT alone. At the same time, *en face* OCTA images have distinctive features and data can be rapidly inspected and compared with structural OCT. This promises to facilitate the diagnostic reading of volumetric data.

Angiogenesis is known to have an essential role in the progression from nondysplastic BE to dysplasia [160]. It has been suggested that the ability to identify atypical microvasculature in BE might facilitate detection of dysplasia [161]. Several endoscopic imaging modalities such as NBI and CLE can increase vascular contrast. However, NBI only visualizes surface vascular patterns. Although CLE can provide subsurface imaging of microvasculature using exogenous contrast agents, it has a limited FOV, and only superficial vasculature can be visualized. OCTA has the advantage that it can perform depth resolved imaging over large fields of view.

Studies investigated Doppler OCT to provide vascular information of the GI tract, measuring blood flow in the large vessels within or below the muscularis mucosa layer [119, 120]. Conversely, OCTA techniques can visualize smaller vessels with slow flow, which are difficult

to see with Doppler OCT. The majority of microvasculature is oriented transverse to the OCT beam and thus is difficult to visualize using the Doppler effect, which is sensitive to axial flow. Our group recently demonstrated the feasibility of using endoscopic OCTA to visualize subsurface vasculature in patients with dysplastic BE using small micromotor catheters [121]. However, the imaging coverage of endoscopic OCTA in this study was limited. Although the diagnostic performance of endoscopic OCTA for detecting dysplasia in BE is still under evaluation, the ability to acquire densely sampled and motion corrected volumetric OCT and OCTA data, enabling both *en face* and cross-sectional views is important for future clinical applications as well as fundamental studies.

Endoscopic OCTA requires a higher sampling density compared with structural OCT because it uses motion contrast to visualize microvasculature. Assuming a focused spot size of ~30 μm (FWHM), the longitudinal sampling interval for OCTA in the current study is ~6 μm, compared to the Nyquist sampling interval of 15 μm. The dense sampling in OCTA increases the acquisition time to survey the esophagus. In addition, since OCTA detects motion, it is more vulnerable to physiological motion artifacts. The imaging speed can be improved by increasing the frame rate of the catheter as well as the A-scan rate of the light source. However, for a given laser exposure, detection sensitivity will decrease inversely proportionally to A-scan rate. In addition, the imaging range will decrease for fixed A/D sampling speeds. Decreased sensitivity can decrease the performance of OCTA especially the ability to detect small vessels or capillaries. An alternative approach would be to rapidly survey the esophagus with Nyquist sampling and then scan with dense sampling to acquire OCT microvasculature information over ROIs with suspicious structural abnormalities.

In addition, the imaging range of the current system was 1.2 mm in tissue due to the A/D sampling, limited by the optical clock module electronics. Although balloon catheters provide stable scanning, centration of the micromotor and optics can vary with flexure of the central sheath, causing changes in range. The flexure is more pronounced if the esophagus has a complex or tortuous geometry, such as in a stricture/narrowing near the gastroesophageal junction (GEJ) or a hiatal hernia. The imaging range can be improved by increasing the optical clock electronic bandwidth to operate at the full A/D card rate. The VCSEL light source driving

waveform can be modified to provide a linearized frequency sweep and improve imaging range. Alternatively, an acoustic-optical modulator [162] or a silicon photonic integrated IQ receiver [163] can be used to remove the complex conjugate ambiguity in the OCT imaging and double the imaging range. However, if variations in centration of the optics are larger than the focusing depth of field, the transverse image resolution will be degraded.

The size of the micromotor balloon catheter in this study was too large to fit in the 3.7 mm endoscope accessory port (GIF-2TH180, Olympus) even after deflating the balloon. Although the current balloon catheter can still be introduced via an overtube, it is desirable to further reduce the size to allow passage through the accessory port. A 2 mm OD micromotor and a ~4.2 mm OD plastic sheath were used in this study. However, micromotors with ODs as small as 1 mm have been reported in recent studies [134]. A customized balloon with desired OD, length, distal and proximal neck can be fabricated. The OD of the plastic sheath used in this study increases the rigidity of the balloon catheter and can be decreased.

There are many approaches which can be used for motion/NURD correction as well as for signal processing in OCTA. The methods demonstrated in this study may not be optimal, but demonstrate the feasibility of the imaging platform. Improvements in motion correction, OCTA processing as well as mechanical design should improve performance in the future, enabling even smaller vessels to be visualized.

Future development of the micromotor balloon catheters promises to enable an integrated platform combining high speed OCT imaging with other endoscopic capabilities. Studies have demonstrated laser marking of biopsy sites for OCT-guided biopsy procedures with distally scanned balloon catheters [164]. Laser thermal coagulation has also been suggested as a therapy for dysplastic BE [165]. Micromotor balloon catheters can improve the beam scanning and positioning accuracy compared with distal scanning, improving laser marking as well as laser beam scanning for treatment.

3.5 Figures

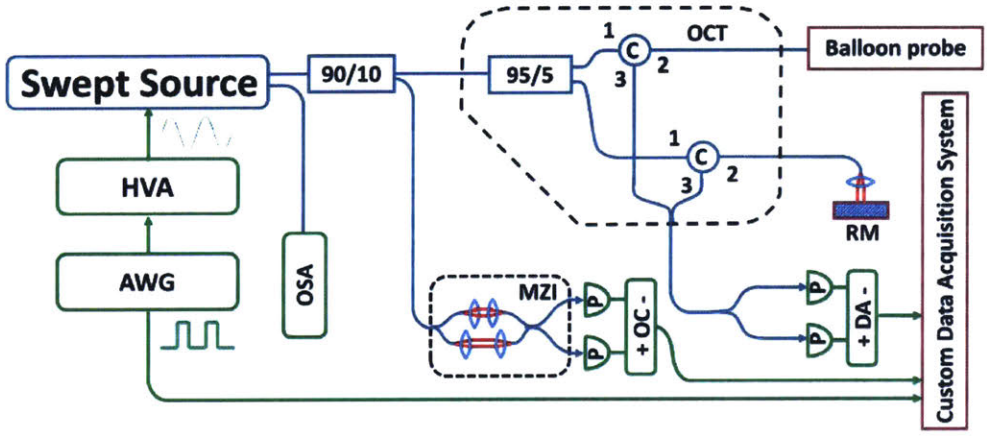

Figure 3.1. Schematic of the ultrahigh speed endoscopic OCT system. HVA: high voltage amplifier; AWG: arbitrary waveform generator; OSA: optical spectrum analyzer; MZI: Mach-Zehnder interferometer; C: circulator; P: photodetector; OC: optical clock, DA: differential amplifier; RM: reference mirror.

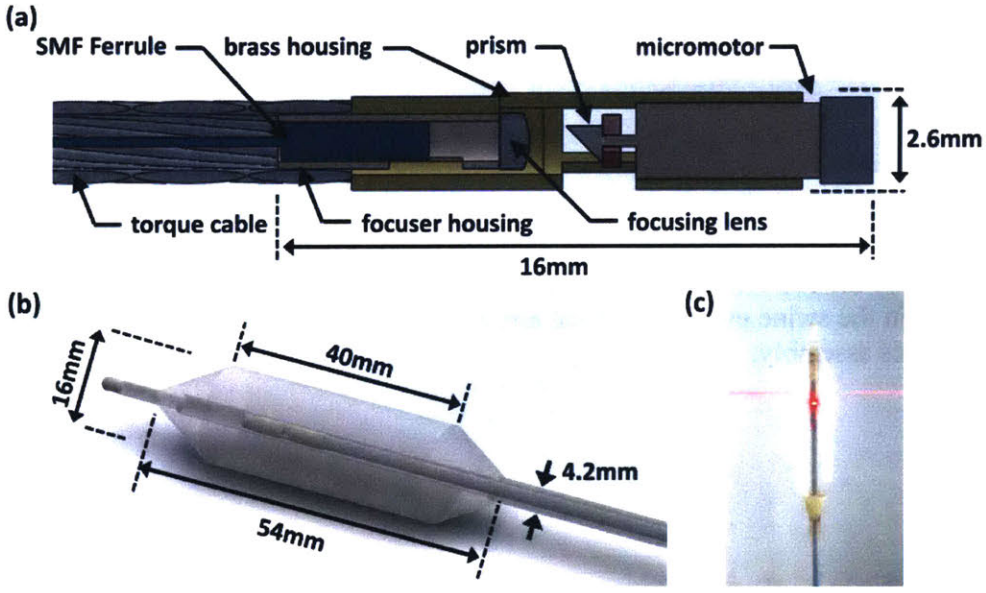

Figure 3.2. Micromotor balloon imaging catheter. (a, b) Schematics of the micromotor imaging catheter and the balloon sheath respectively. (c) Photograph of the distal end of the micromotor balloon imaging catheter.

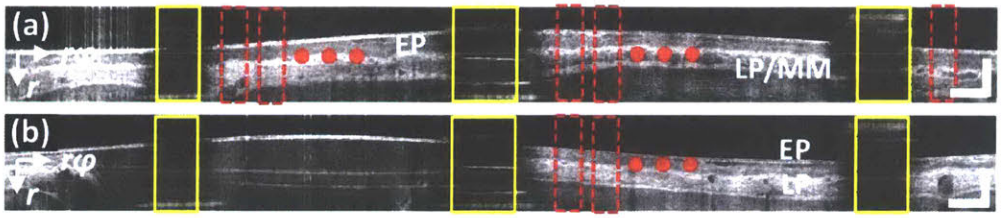

Figure 3.3. Correction of nonuniform rotational distortion (NURD) from the micromotor scanning and physiological motion. (a, b) Cross-sectional OCT image of the swine esophagus, where the esophagus was not fully in contact with the balloon catheter during imaging in (b). Multiple regions of interest (ROIs) were selected from locations of the metal struts (yellow box) and tissue structures in multiple zones (red boxes and red dots) to remove the motion artifacts in the images. Scale bars: 0.5 mm (axial) and 2 mm (lateral). EP: epithelium; LP: lamina propria. rφ: circumferential direction; r: radial (axial) direction.

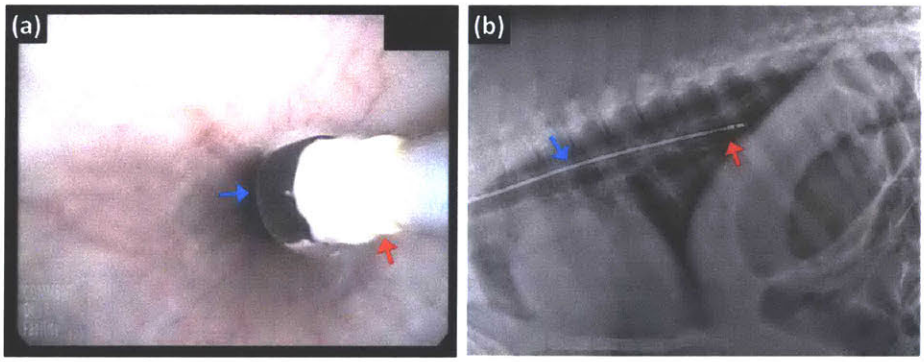

Figure 3.4. (a) White light endoscopy image showing the positioning of the micromotor balloon imaging catheter in the swine esophagus. Blue arrow: inflated balloon; red arrow: joint between the proximal end of the balloon and plastic sheath. (b) X-ray showing the position of micromotor balloon catheter in the swine esophagus. Blue arrow: torque coil of the micromotor catheter; red arrow: distal optics assembly.

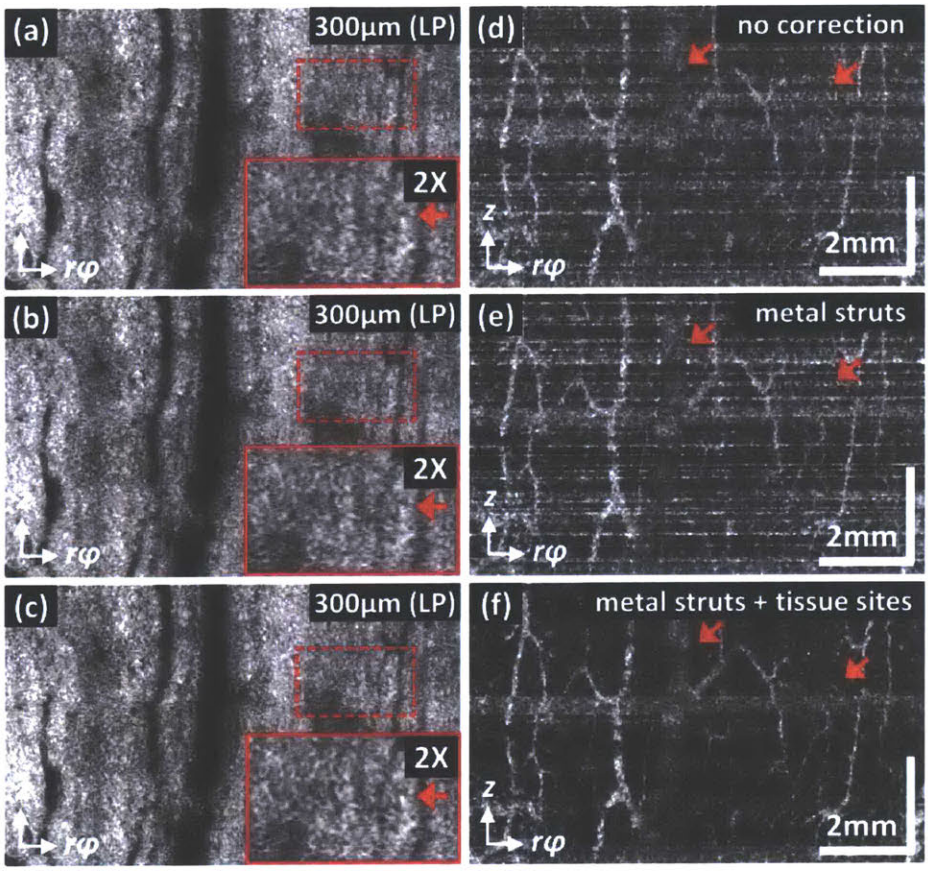

Figure 3.5. Demonstration of the NURD correction algorithm for *en face* OCT and OCT angiography (OCTA) images. (a, d) , (b, e), and (c, f) Co-registered *en face* OCT and OCTA images of the lamina propria (LP) layer of the swine esophagus from 300 μm beneath tissue surface before and after motion correction using regions of interest (ROIs) from the metal struts alone compared with both metal struts and tissue sites, respectively. Insets: magnified view (2X) from the selected region (dashed boxes, a-c) demonstrated that NURD between neighboring frames was significantly reduced (red arrows). In OCTA, decorrelation noise and white line motion artifacts were reduced, and image contrast was improved after NURD correction (red arrows, e-f). rφ: circumferential direction; z: longitudinal pull back direction. The same signal thresholds were applied for (a), (b) and (c), as well as for (d), (e) and (f).

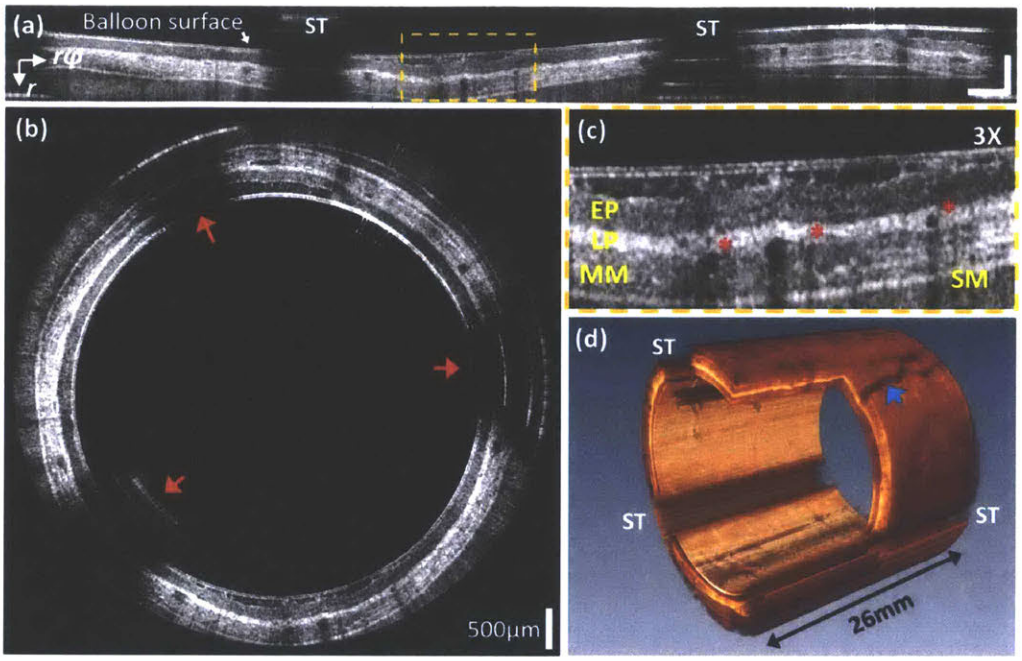

Figure 3.6. Micromotor balloon OCT of the swine esophagus in vivo. (a, b) Representative cross-sectional images in polar and Cartesian coordinates. The Cartesian image is shown with a 4:1 aspect ratio. (c) Magnified view (3X) of the cross-sectional OCT image from the region of interest (dashed box, (a)) shows epithelium (EP), lamina propria (LP), muscularis mucosa (MM), and submucosa (SM) of normal esophagus. Small vessels in the LP (star) are also visible. (d) Rendering of the esophagus. Blue arrow: shadowing from a large vessel. ST: circumferential regions blocked by metal struts. Scale bars in (a): 0.5 mm (axial) and 2 mm (lateral). rφ: circumferential direction; r: radial (axial) direction.

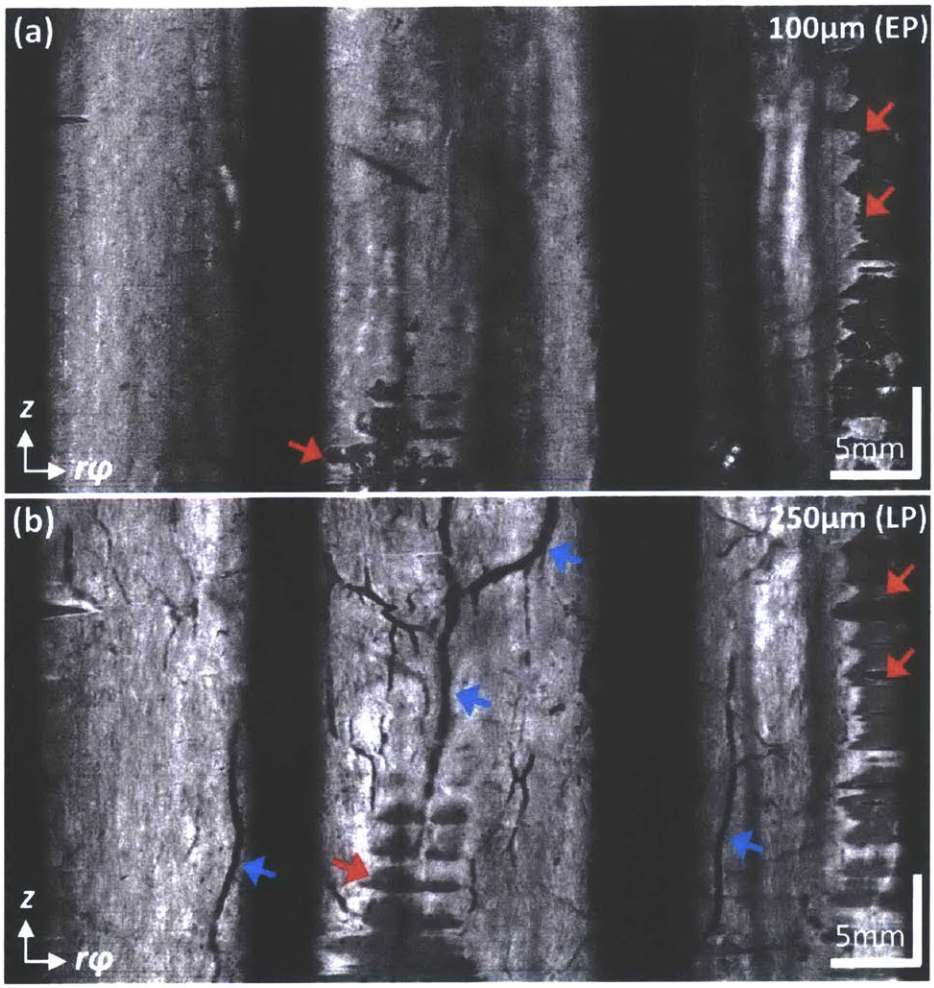

Figure 3.7. (a, b) *En face* OCT of the swine esophagus from ~100 μm (mean projection from 75 to 125 μm) and 250 μm (mean projection from 225 to 275 μm) below surface correspond to the epithelium (EP) and the lamina propria (LP) layer, respectively. Tissue contact varied along the pullback direction (red arrows) because of cardiac motion. Shadowing from the shallower vessels can be seen (blue arrows). rφ: circumferential direction; z: longitudinal direction.

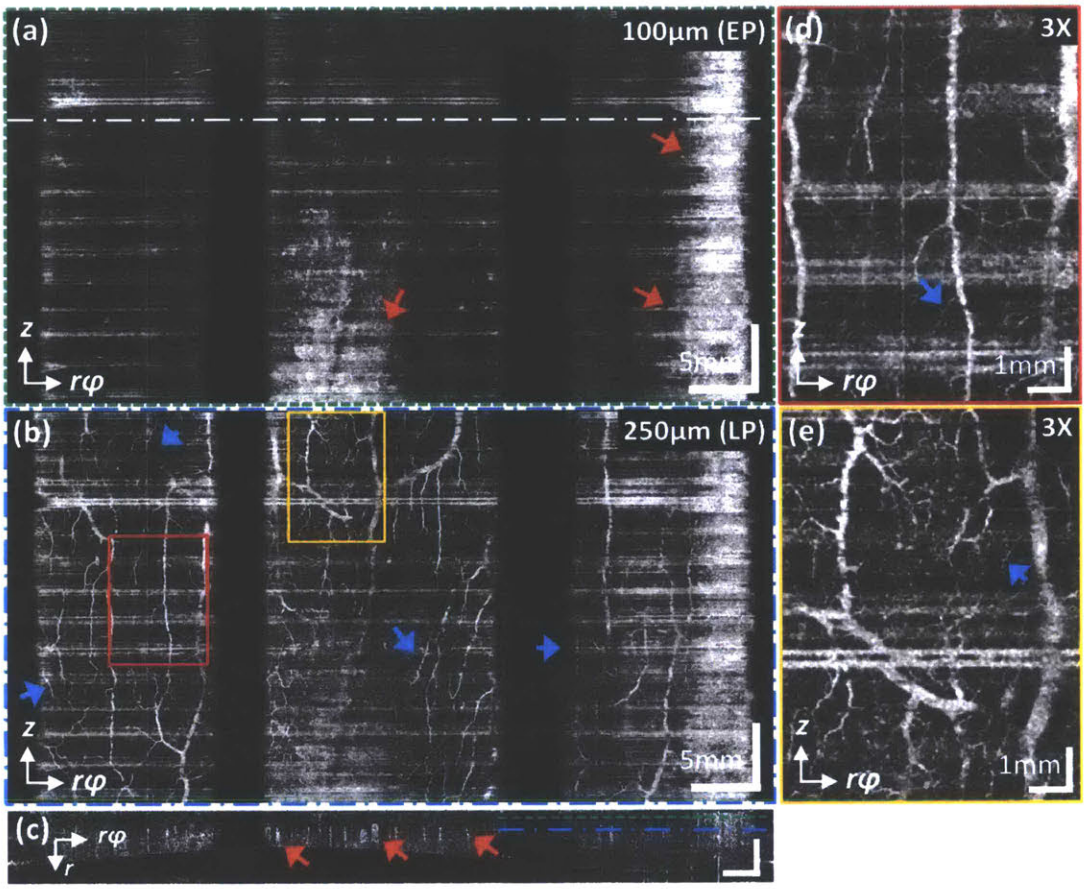

Figure 3.8. (a, b) *En face* OCTA of the swine esophagus from 100 μm (mean projection 75 to 125 μm) and 250 μm (mean projection from 225 to 275 μm) below the tissue surface, corresponding to the epithelium (EP) and lamina propria (LP) layer, respectively. Tissue contact varied along the pullback direction (red arrows) from cardiac motion, resulting in high decorrelation near the tissue boundary. Microvascular networks are seen in the LP layer (blue arrows). (c) Cross-sectional OCTA image from the location in (a) marked by a white dashed-dotted line. The locations of the microvasculature can be identified from regions exhibiting high decorrelation signals (red arrows). The depth locations of the *en face* OCTA images of the EP and LP layer (a, b) are marked by green and blue lines, respectively. (d, e) Magnified (3X) view of the OCTA from the region of interest marked (b) where the small vessels can be observed more clearly (blue arrows). rφ: circumferential direction; z: longitudinal pull back direction; r: radial (axial) direction. Scale bars in (c): 0.25 mm (axial) and 2 mm (lateral).

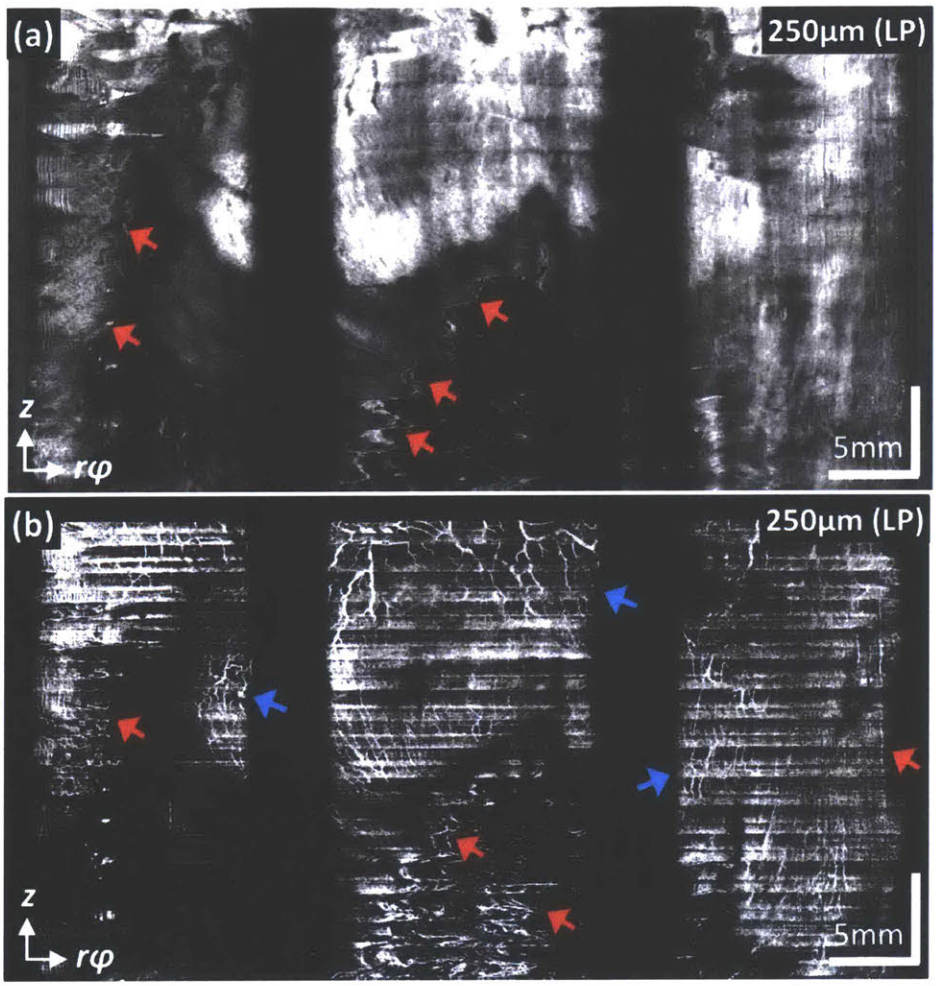

Figure 3.9. (a, b) Coregistered *en face* OCT and OCTA images of the swine distal esophagus including the gastroesophageal junction (GEJ) from about 250 μm (mean projection from 225 to 275 μm) beneath the tissue surface, corresponding to the lamina propria (LP) layer in the squamous mucosa. As a result of the opening after GEJ, the tissue contact was poor in the gastric mucosa (red arrows, (a, b)). Fine microvasculature in the LP layer can be observed in the squamous mucosa (blue arrows, (b)). rφ: circumferential direction; z: longitudinal direction.

CHAPTER 4

4.0 Endoscopic Optical Coherence Tomography Angiography Microvascular Features Associated with Dysplasia in BE

4.1 Motivation

Barrett's esophagus (BE) is a precursor in the progression of esophageal adenocarcinoma (EAC), which is among the most lethal diseases with a five-year survival rate <20% [166]. The incidence of EAC is significantly increased in patients with any grade of dysplasia [8], and HGD is associated with 10-60% increased risk of developing into EAC within 3-5 years [7, 10, 11]. Although various advanced endoscopic imaging modalities have been widely investigated, detecting dysplasia in BE with high diagnostic accuracy remains a challenge [167]. Angiogenesis is associated with tumor progression, and vascular alterations often precede neoplastic transformation, suggesting that changes in vascular patterns may be indicators for early stage neoplasms [109, 110, 168]. Increased microvessel density in the progression from NDBE to LGD and HGD was recently reported based on *ex vivo* pathology specimens[169]. Narrow band imaging (NBI) [33, 34] and confocal laser endomicroscopy (CLE) [36, 39] were used to investigate microvascular changes as a potential marker for dysplasia. However, NBI has limited resolution and only visualizes surface vascular patterns. CLE has a limited field of view (<0.2 mm^2), is less suited for surveying wide areas of the esophagus and requires contrast agents such as fluorescein. Multiple administrations of fluorescein may be required if the imaging session is prolonged [170].

Endoscopic optical coherence tomography (OCT) provides near-microscopic, real-time, volumetric imaging of esophageal mucosa with an imaging depth of 1-2 mm [86, 88]. Previous studies investigated structural features for detecting dysplasia using cross-sectional OCT images, but diagnostic accuracy and interobserver agreement were limited [95, 107, 171]. OCT angiography (OCTA) is an extension of OCT, which can visualize subsurface three-dimensional (3D) microvasculature without requiring contrast agents [88, 119]. However, the limited imaging speed and optical scanning instability in previous endoscopic OCT systems have made clinical OCTA difficult. Recently, our group demonstrated endoscopic OCTA imaging of subsurface microvasculature in the human esophagus using an ultrahigh speed endoscopic OCT system and micromotor imaging catheters that address these limitations [121]. Compared with other endoscopic imaging modalities providing vascular contrast, OCTA can image a larger area than CLE and does not require contrast agent administration. Furthermore, OCTA allows subsurface imaging of the esophagus with higher imaging resolution than NBI. Therefore, OCTA is a

promising technique for assessing mucosal microvascular features of dysplasia. In this study, we investigated the feasibility of using endoscopic OCTA to differentiate dysplasia from NDBE. We performed a pilot study investigating microvascular features associated with NDBE and dysplasia in OCTA datasets obtained from patients with BE and developed OCTA criteria to detect LGD/HGD. Preliminary results on the accuracy of the OCTA criteria using blinded reading of the OCTA datasets by multiple readers are reported.

The prototype ultrahigh speed endoscopic OCT system used in this study was developed by the members in Professor Fujimoto's group as described in detail in chapter 2. All the endoscopic OCT/OCTA datasets were taken in collaboration with Dr. Hiroshi Mashimo, MD. PhD. who performed all the endoscopy sessions at the VA Boston Healthcare System (VABHS, Jamaica Plain Campus). Kaicheng Liang and Osman Ahsen participated in the discussion improving the design of the micromotor catheters to meet the requirement for this clinical study. Osman Ahsen, Kaicheng Liang, Drs. Michael G. Giacomelli and Zhao Wang, and I shared the responsibility managing the OCT imaging session in the clinics. All the micromotor catheters used in the study were assembled by Osman Ahsen and myself, and so do the management of the patient recruitment at VABHS. The processing of the datasets used to develop the OCTA criteria was performed by Osman Ahsen and myself. The management of the blinded OCTA readings as well as the statistical analysis was all performed by the author of the thesis work.

4.2 Endoscopic OCTA and Study Design

4.2.1 Patient enrollment

The imaging procedures were performed at the VABHS with approvals from the institutional review boards at VABHS, Harvard Medical School, and Massachusetts Institute of Technology. Fifty-two patients including: (1) patients without history of dysplasia and undergoing BE surveillance (N=23) and (2) patients with history of dysplasia who were treatment naïve or undergoing endoscopic eradication therapy (EET, including radiofrequency ablation, endoscopic mucosal resection (EMR), or cryospray ablation) for dysplasia (N=29) were recruited from March 2014 to February 2016.

After providing written informed consent, patients underwent standard EGD. Regions of interest (ROIs) identified by white light endoscopy (WLE) or NBI per standard clinical practice were imaged with endoscopic OCTA using a micromotor imaging catheter introduced through one instrument channel of a high-definition, dual-channel endoscope (GIF-2TH180, Olympus) while the other channel was reserved for the biopsy forceps. Details of the OCT/OCTA imaging procedure can be found in the subsequent section 4.2.2. Following OCTA imaging, either biopsies using standard biopsy forceps or EMRs (Duette, Cook Medical) were taken from the imaged sites for histopathology analysis based on clinical indication (Figure 4.1). The spatial location information (e.g. clock and longitudinal location) of all the histology specimens, which were submitted in separate jars for histology processing, were documented per standard clinical practice, and the histopathological diagnosis was used to correlate and classify the associated OCTA dataset. This protocol enabled accurate registration of the OCTA image data with histology, but the OCT catheter had limited area coverage compared with imaging balloons [120].

OCTA datasets corresponding to NDBE were obtained from patients undergoing BE surveillance who had all histopathological diagnoses negative for dysplasia, or from patients undergoing EET with prior dysplasia diagnosis, who had all histopathological diagnoses negative for dysplasia in the same visit as the OCTA imaging session. All histopathological diagnoses from any neighboring regions were required to be negative for dysplasia in order to assure the integrity of the OCTA datasets corresponding to NDBE. OCTA datasets corresponding to dysplasia were obtained from patients with a history of dysplasia having histopathological diagnoses positive for dysplasia, or from patients undergoing BE surveillance who had incidental histopathological diagnoses positive for dysplasia. Overall, 97 OCTA datasets with corresponding histological diagnoses (NDBE: N=74; LGD: N=10; HGD: N=13) were collected from 52 patients (NDBE: N=41; LGD: N=7: HGD: N=4, based on the baseline pathology) enrolled to the study.

4.2.2 Endoscopic OCT and OCT Angiography (OCTA) imaging procedure

In this study, as described in section 4.2.1, patients without a history of dysplasia and undergoing BE surveillance (naïve NDBE) as well as patients with a history of dysplasia who were treatment naïve or undergoing EET for dysplasia (dysplastic BE) were enrolled. The endoscopic OCTA

imaging procedure and the subsequent histology specimen collection were specifically designed and performed to address the nature of the patient demographic and being consistent with the clinical practice.

For patients with naïve NDBE, the OCT/OCTA imaging procedure was performed as listed following:

- Position the OCT catheter at 6 o'clock near GEJ and take sequential OCT datasets (pullback length: 2 cm each) separated by an interval of 1 cm or 2 cm depending on the length of BE until SCJ is observed in the OCT preview.
- If the length of BE is longer than 6 cm, an interval of 2 cm is used. Otherwise, each sequential OCT datasets is separated by 1 cm.
- During the sequential acquisition, if OCT preview after each acquisition shows motion or contact issue, attempt to reacquire OCT imaging at given location might be performed.
- If any ROI is identified by WLE or NBI, OCT imaging over the ROI region will be performed. The ROI can be at any clock hour or position. For example, if there is a tongue or island of BE.
- Seattle biopsy protocol commences (4 quadrants every 2 cm). Biopsies from same longitudinal positions are stored in the same jar, i.e. biopsies from different quadrants cannot be distinguished.
- Biopsy over the ROIs if present and not overlapped with those collected from the Seattle protocol. The biopsy over the ROI will be stored in a separate jar.
- Lastly, although multiple OCT/OCTA datasets might be collected from individual patient visits, each OCT/OCTA collected needs to separated apart by a distance of $\geq$ 2cm.
- For example, a patient shows 4 cm BE, which results in 3 jars of biopsies. If all 3 jars shows NDBE, only 2 OCT datasets with corresponding NDBE histology can be collected.

For patients with dysplastic BE, the OCT/OCTA imaging procedures were different from that of the patients with naïve NDBE since potentially there existed prior information on the location of the ROIs (i.e. the dysplastic BE).

- ROIs are defined using the following protocols:

i. If the location information of the dysplastic BE diagnosis is indicated on the prior exam. Note that only the longitudinal information of the biopsy specimens was documented compared to that both the clock and longitudinal location information were documented for the EMR specimens.

ii. Examine with WLE and NBI. If the ROI is a raised lesion, EMR will be performed after the OCTA imaging procedure; if ROI is not raised but exhibits an abnormal mucosal pattern, a biopsy will be performed afterward.

- If there is an ROI on (ii) above, perform OCT over this region (can be any clock hour or longitudinal position). Position the OCT catheter in ROI and acquire multiple OCT data sets (distal/proximal margins).
- If there is no ROI (which often occurs in patients in the follow up EGD visit after the EET treatment), position the OCT catheter at 6 o'clock near GEJ and take sequential OCT datasets (pullback length: 2 cm each) separated by 1 cm or 2 cm till SCJ is observed in the OCT preview. If the length of BE is longer than 6 cm, an interval of 2 cm is used. Otherwise, each sequential OCT datasets is separated by 1 cm.
- Perform biopsy every 2 cm at 6 o'clock (not Seattle protocol).

4.2.3 Endoscopic OCT imaging system

The study used a prototype, ultrahigh speed endoscopic OCT instrument and micromotor imaging catheters to perform volumetric imaging of the esophageal microvasculature. The technology has been described in detail previously [121, 133]. Briefly, the OCT system and micromotor catheter had an imaging speed of 600,000 depth (axial) scans per second and a frame rate of 400 frames per second, >10 times faster than commercially available endoscopic OCT systems. The axial and lateral image resolution was ~8 μm and ~20 μm in tissue, respectively. Each volumetric OCT acquisition imaged a surface area of 10 mm (rotary) x 16 mm (longitudinal) in ~8 seconds using a helical (pullback) optical scan pattern, consisting of 1500 (rotary) x 3200 (longitudinal) depth scans.

4.2.4 Endoscopic OCTA and data visualization

OCTA visualizes microvasculature by using motion contrast, without requiring exogenous contrast agents. Figure 4.2 shows a flow chart summarizing the image processing steps for

generating depth resolved *en face* OCTA images [133, 137]. Prior to computing the volumetric OCTA datasets, a motion correction algorithm was applied offline in post-processing to remove the nonuniform rotation distortion (NURD) [137]. Volumetric OCTA datasets were generated afterward by computing pixel-by-pixel differences/variations of the OCT signal intensities between consecutive OCT frames in NURD-corrected volumetric OCT dataset. Moving erythrocytes in microvasculature cause the OCT signal intensity to vary with time, which can be quantified by calculating a decorrelation (D). Conversely, static tissue has a constant OCT signal. Depth resolved *en face* OCTA images were generated by using mean projection over a depth range of 100 μm, at various depth levels beneath the tissue surface. Faster vs. slower blood flows are associated with higher vs. lower OCTA decorrelation signals. However, it is important to note that OCTA does not measure absolute flow. In addition, OCTA is more sensitive to tissue motion than OCT and respiration or cardiac motion can generate artifacts, compromising data quality [133]. The tissue motion can potentially result in varying catheter-tissue contact, which decreases the effective OCTA imaging coverage. Furthermore, the excessive pressure exerted by the catheter over the tissue surface can suppress the blood flow and hence results in low OCTA signals.

4.2.5 OCTA reading criteria and protocol

The 97 OCTA datasets collected from 52 patients were reviewed to assess image quality by a single investigator, not involved in validating the OCTA reading criteria. A total of 54 datasets (NDBE: N=35; LGD: N=8; HGD: N=11) from 32 patients (NDBE: N=22; LGD: N=6: HGD: N=4, based on the baseline pathology) were retained for training and reading, while 43 OCTA datasets (NDBE: N=39; LGD: N=2; HGD: N=2) were not used because of inadequate image quality due to artifacts from tissue motion, decreased imaging coverage from varying catheter-tissue contact, or excessive pressures shown in the example OCTA images (Figure 4.3). The inadequate image quality resulted in part because OCTA images were generated by post processing and were not available in real time during endoscopy. Most of the dysplasia OCTA datasets exhibited adequate image quality due to the attempts to carefully perform OCTA imaging over the regions exhibiting irregular mucosa or vascular pattern under WLE or NBI. The 54 volumetric OCTA datasets were examined by the same investigator to identify features associated with dysplasia in order to develop the OCTA reading criteria. Details of the

development of the OCTA criteria in the initial learning phase, as well as the following training and validation session, are provided in the sections 4.2.5 and 4.2.6, respectively. In general, a honeycomb/oval-like microvascular pattern of varying size was observed in NDBE OCTA datasets (Figures. 4.4(A-C)). While the size/shape of the honeycombs could vary along the longitudinal (pullback) direction due to motion artifacts, the distribution of the honeycombs was in general relatively regular. In the LGD/HGD datasets, OCTA exhibited microvasculature features of (1) abnormal vessel branching with crowding or corkscrew appearance, and (2) heterogeneous vessel size, i.e. presence of vessels with different calibers (Figures 4.4(D-F)), similar to those previously reported with magnification NBI [33, 34]. However, unlike NBI, OCTA enables volumetric visualization of the subsurface microvasculature.

4.2.6 Development of the OCTA criteria – initial learning phase

In the initial phase, a single investigator (who was not involved in validating the OCTA criteria in the later phase) reviewed the 54 OCTA datasets with corresponding histological diagnoses (NDBE: N=35; LGD: N=8; HGD: N=11). In this phase, three microvascular features were identified as associated with dysplasia in contrast to NDBE which were: (1) irregular honeycomb pattern, (2) abnormal vessel branching, and (3) heterogeneous vessel size. In establishing these features, existing NBI literature [33, 34, 172] was extensively studied which provided comprehensive descriptions of the vascular features that are associated with dysplasia.

The identified features were validated by an independent OCT expert with OCTA experience using a subset of the OCTA images (N=28) with corresponding histological diagnoses (NDBE: N=18; LGD: N=3; HGD: N=7). The presence of irregular honeycomb pattern was found to be highly overlapped with abnormal vessel branching and exhibited lower accuracy for differentiating dysplasia from NDBE (~70% sensitivity). Therefore, the irregular honeycomb pattern was removed, and the remaining two features of (1) abnormal vessel branching and (2) heterogeneous vessel were used to develop the OCTA criteria, which was validated by multiple readers (who were not involved in the development of the OCTA criteria) in the later phase.

4.2.7 Training/validation session

The two-feature OCTA reading criteria was developed based on these observations and independently validated by blinded readers with various levels of OCT/OCTA experience, including 3 OCT trainees, one gastroenterologist, and 2 gastroenterology (GI) fellows. Prior to the validation reading, each reader received a training session including a ~40 minute interactive presentation consisting of six volumetric OCTA datasets. During the training session, examples of OCTA datasets corresponding to NDBE and LGD/HGD that exhibited characteristic microvascular features, as well as datasets having minor artifacts from respiration or cardiac motion, or a slightly decreased imaging coverage from varying catheter-tissue contact were presented (Fig. 4.4).

The training session was followed by a pretest with seven volumetric OCTA datasets prior to the validation reading. During the pretest, each reader assessed the presence of abnormal microvascular features in the volumetric OCTA datasets using the software viewer ImageJ (National Institutes of Health) following the workflow described in the section 4.2.7. The pretest results of individual readers were immediately reviewed and discussed with an investigator to ensure that each reader understood the reading criteria before performing the validation reading. For the validation, the readers followed the same protocol as the pretest, but without discussion of results. In addition, after reading all volumetric OCTA datasets sequentially, each reader was asked to review the datasets and allowed to adjust their assessments made during the initial reading. This consolidated readers' understanding on the OCTA features from the initial reading and therefore reduced possible inconsistency in the assessment of features. Furthermore, during the review process (final reading), each reader was asked to rate the confidence level of his/her feature assessment in each dataset as "high" or "low." During the pretest and validation, readers were blinded to the endoscopic and histopathological findings. The reading time and individual readers' confidence level for each OCTA dataset were recorded.

4.2.8 Workflow of the OCTA reading protocol

(1) Read *en face* OCTA images in the superficial BE epithelium from 10 μm to 300 μm below the tissue surface. This allows readers to survey the microvasculature changes associated with depth as well as possible image artifacts near the tissue surface. (2) Evaluate the presence of

abnormal microvascular features down to a maximum depth of ~220 μm (excluding OCTA from depths located in the muscularis mucosa). (3) If a feature(s) is present, annotate the regions exhibiting the most prominent feature(s) in the *en face* OCTA image; then, proceed to next OCTA dataset.

4.2.9 Statistical analysis

Measures of the OCTA criteria accuracy including the sensitivity, specificity, positive predictive value (PPV), and negative predictive value (NPV) were calculated for each reader separately as well as all six readers combined, along with the binomial 95% confidence interval. The interobserver agreement for the assessment of abnormal microvascular features as well as the accuracy among six readers was calculated using unweighted kappa statistics [173]. The level of agreement was interpreted as a kappa value, where 0.41-0.60 was defined as moderate agreement, and 0.61-0.80 as substantial agreement [174].

4.3 Performance of the OCTA Criteria

4.3.1 Baseline characteristics

Table 4.1 presents the demographics and baseline characteristics of the patient enrollment. After excluding the datasets with inadequate image quality, 54 volumetric OCTA datasets remained from 32 patients (all male, age (y) 67±8). A median of 1 (range: 1-7) OCTA dataset was obtained per patient. 14 out of 35 NDBE OCTA datasets (40%) were from patients without a history of dysplasia or EET treatment. The number of the OCTA datasets corresponding to NDBE and LGD/HGD pathologies for the training/pretest/validation sessions were N=4, 4, 27, and N=2, 3, 14, respectively (Table 4.2).

4.3.2 Diagnostic performance of the OCTA criteria

The overall diagnostic performance of individual microvascular features associated with dysplasia is summarized in Table 4.3. A scoring index was used to assess the accuracy of the OCTA criteria by applying different thresholds. A score of 1 or 2 was assigned if one or two of the features were present, respectively. A score threshold of ≥1 resulted in an overall 94% (95% CI, 89-99) sensitivity, 69% (95% CI, 62-76) specificity and 96% (95% CI, 92-99) NPV. The

accuracies of the OCTA criteria for individual readers are summarized in Table 4.4. Table 4.5 lists the number of datasets corresponding to the histopathological diagnosis of NDBE/LGD/HGD assessed by readers with high confidence. The majority of the LGD/HGD pathologies were assessed with high confidence, and low confidence readings were mostly associated with the false positive assessment of NDBE as LGD/HGD. A low interobserver agreement (kappa 0.10) was observed among six readers on the datasets that were assessed with the low confidence level in the validation session. For the datasets that were read with high confidence, an overall 93% (95% CI, 87-99) sensitivity, 81% (95% CI, 75-88) specificity and 95% (95% CI, 92-99) NPV were obtained (Table 4.3).

Among the six readers, the interobserver agreement was moderate (kappa 0.58) using a threshold of ≥ 1. The inter-observer agreement was moderate for abnormal vessel branching (kappa 0.53) and heterogeneous vessel size (kappa 0.43). A subset analysis using only NDBE datasets from patients without a history of dysplasia showed similar diagnostic performance to using only NDBE datasets from patients with a history of dysplasia/EET (p=0.71, Table 4.6). The mean reading time per volumetric OCTA dataset was 45 ± 25 seconds, and breakdown of the overall time into initial and final reading times by individual readers is shown in Table 4.7.

A similar distribution of OCTA microvascular features was observed between LGD and HGD subgroups in the reading results (Table 4.8). For example, the presence of feature 1 (abnormal vessel branching) was identified in 83.3% and 90.5% of the LGD, and HGD OCTA datasets, respectively (p=0.33), and feature 2 (heterogeneous vessel size) was identified in 71.4% and 76.2 of the LGD and HGD OCTA datasets, respectively (p=0.62). Analysis of OCTA features associated with LGD and HGD subgroups shows 88.1% sensitivity and 69.1% specificity for differentiating LGD from NDBE and 100% sensitivity and 69.1% specificity for differentiating HGD from NDBE (Table 4.9).

Finally, the accuracy for differentiating dysplasia from NDBE after the initial reading (prior to reviewing the datasets (final reading)) by individual readers was 88.1% sensitivity and 67.3% specificity using a score threshold of ≥ 1 (Table 4.10). A moderate interobserver agreement (kappa: 0.46) was found on the initial readings among the six readers using a threshold of ≥ 1.

We also compared the accuracy of the final readings on the first half of datasets to the second half of the datasets to address if readers' fatigue affected the diagnostic accuracy. A comparable diagnostic accuracy (first half: sensitivity/specificity: 100%/67.9%, respectively; second half: sensitivity/specificity: 89.6%/69.2%, respectively) was observed ($p=0.13$), suggesting that this might not be a critical factor in the readings.

4.4 Discussion

The detection of early dysplastic progression towards adenocarcinoma is a major unmet need in the assessment of Barrett's esophagus. Among various advanced endoscopic imaging modalities, endoscopic OCTA has the unique advantage of visualizing subsurface microvasculature in three dimensions without contrast agents. Although previous endoscopic studies have demonstrated OCT vascular contrast using the Doppler effect, results were limited to measuring blood flow in large vessels either within or below the muscular layer [88, 119] and did not visualize microvasculature in the superficial BE mucosa [121]. It was challenging to perform OCTA using earlier-generation endoscopic OCT systems because of insufficient imaging speeds. Thus, most OCT studies focused on investigating tissue architectural features. To the best of our knowledge, this is the first study investigating *in vivo* microvasculature identified by OCTA as a potential marker for pathology. In particular, this study focused on identifying OCTA features associated with dysplasia vs. NDBE.

A recent study using commercial endoscopic OCT, volumetric laser endomicroscopy (VLE), investigated dysplasia detection performance in 27 patients by analyzing the architectural features in multiple cross-sectional images from volumetric OCT datasets [96]. This study achieved 86% sensitivity and 88% specificity for detecting dysplasia on *ex vivo* EMR specimens using a new algorithm based on OCT structural features. However, further validation on *in vivo* volumetric OCT datasets is still required. In our study, volumetric structural OCT datasets with higher sampling density than commercial endoscopic OCT technology, co-registered to the volumetric OCTA datasets, were also available. However, the optimal method for reading volumetric structural OCT data is complex and still under investigation [96, 175]. Therefore, our study focused on OCTA and investigated the accuracy for differentiating dysplasia from NDBE using microvascular features.

Given the difficulties in diagnosing LGD by imaging as well as histopathology, in the majority of previously reported endoscopic imaging studies, LGD was either categorized together with NDBE or was excluded from the study. During the development of the OCTA criteria, we observed that OCTA could differentiate LGD from NDBE in the cases collected for this study. We also observed that OCTA features associated with LGD were similar to those associated with HGD (Table 4.8). Furthermore, the pathological diagnosis of all LGD cases was made by a specialized pathologist with >15 years' experience in GI pathology. A third-party confirmation from expert referral centers, such as The Joint Pathology Center (Silver Spring, MD) or the Massachusetts General Hospital (Boston, MA), was obtained when necessary. Therefore, in this study, we have grouped LGD cases together with HGD, given the malignant potential of confirmed LGD that necessitates RFA treatment [176]. Nevertheless, we also investigated the accuracy of using OCTA to differentiate LGD from NDBE independently and showed comparable performance to HGD vs. NDBE (Table 4.9). However, the sample size is small, and further larger scale studies are warranted.

Due to the limited sample size and readers' varying OCT/OCTA experience, individual readers were also asked to review the datasets (final reading) after their initial reading and rate the confidence level in their assessment of features during the final reading, similar to previously reported NBI [177, 178] and CLE [179] imaging studies. Some of the low confidence readings might be associated with cases where features were less clear and thus more difficult to diagnose using the proposed two-feature OCTA criteria alone. Both the ambiguities in the OCTA datasets and the insufficient training on individual readers might result in the lower interobserver agreement (kappa 0.10) on the rating of confidence level in each OCTA dataset. We observed an increase in the overall accuracy (sensitivity/specificity: 88.1%/67.3% vs. 94%/69.1%, respectively) and interobserver agreement (0.46 vs. 0.58) between the initial and final readings (Tables 4.2 & 4.10). These results suggest a learning curve in the current study whereby the readers consolidated their understanding of the OCTA features from the initial reading. Nevertheless, the accuracy was comparable among the six readers including the two GI fellows who had no prior OCT/OCTA experience, suggesting that the capability to learn and implement the OCTA criteria did not vary with readers' baseline OCT/OCTA experience levels (Table 4.4).

We hypothesize that both the learning curve and interobserver agreement could be further improved with increased sample size.

In addition, since the effect of prior EET on the microvascular features has not been investigated completely, a subgroup analysis was performed to compare the assessment of NDBE OCTA datasets obtained from patients without a history of dysplasia versus NDBE datasets obtained from patients with a history of dysplasia/EET (Table 4.6). A comparable detection accuracy was observed (p=0.71).

Furthermore, individual readers were asked to assess the presence of abnormal features in the stack of depth resolved *en face* OCTA images in each OCTA dataset in both the initial and final readings. The features were scored based on their presence or absence, rather than introducing different degrees of severity for individual features. More complex scoring systems risk reducing the interobserver agreement and make it difficult to set a diagnostic scoring threshold achieving a detection accuracy of a high sensitivity and specificity for all readers.

Approximately 44% of the datasets (N=43) were not used for analysis due to inadequate image quality: (1) artifacts from respiration or cardiac motion, (2) decreased imaging coverage from varying tissue contact, and (3) excessive pressure exerted by the catheter over the tissue surface suppressing blood flow (Figure 4.3). The low yield of OCTA data occurred in part because our prototype instrument did not generate OCTA images in real time. Although structural OCT was displayed during endoscopy immediately as the images were acquired, OCTA images were generated offline in post-processing. The generation of OCTA images requires additional motion correction step to remove the nonuniform rotation distortion in the volumetric OCT dataset, which is a time-intensive computation process. State-of-the-art computation using Graphic Processing Units (GPU) with a large number of cores allows massively parallel processing and may enable generation of the volumetric OCTA datasets in real time. Therefore, real time OCTA display can potentially be implemented but requires significant software development efforts.

The imaging coverage of OCTA is currently limited by the small catheter size. In this study, we used an imaging catheter introduced into one instrument channel of a dual-channel endoscope so the second channel could be used for biopsy. In addition, the small size catheter equips a superior transverse resolution, higher rotation speed, and less non-uniform rotational distortion than the commercial endoscopic OCT instruments. On the contrary, commercial endoscopic OCT instruments use a balloon catheter which images a 6 cm circumference x 6 cm length of the esophagus in ~90 seconds. Our current prototype instrument could generate a comparable structural image ~10x faster, however since OCTA uses motion contrast to visualize blood flow, the same region must be scanned very densely, and there are trade-offs between imaging speed and area coverage. Our prototype instrument and catheter can perform OCTA of a 1 cm circumference x 1.6 cm length in 8 seconds. A recent study by our group using an ultrahigh speed OCT system and a micromotor balloon catheter demonstrated circumferential OCTA imaging of the swine esophagus over a 5 cm circumference x 2.6 cm length <18 seconds [140]. This result suggests that wide area OCTA in human subjects is feasible.

In conclusion, volumetric *en face* OCTA imaging enables rapid examination of depth resolved microvascular features with near-microscopic resolution. This study identifies microvascular features which are associated with dysplasia in Barrett's esophagus and suggests that OCTA information can serve as an adjunct to volumetric structural OCT. This new imaging modality also provides additional information on subsurface microvasculature, which could help the study of dysplasia pathogenesis. These promising results motivate the need for future technology improvements and larger scale prospective studies investigating the diagnostic accuracy of OCTA.

4.5 Figures

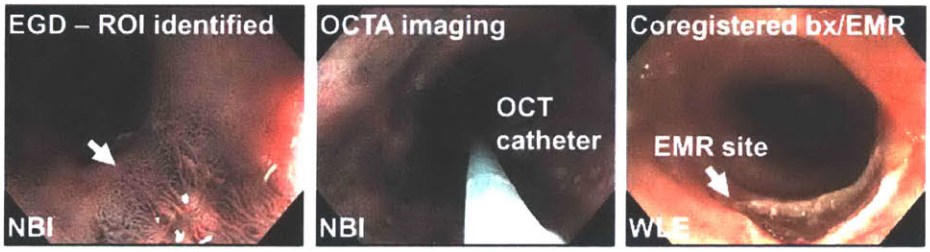

Figure 4.1. Flow chart illustrating the OCT/OCTA imaging procedure and collection of the corresponding histology.

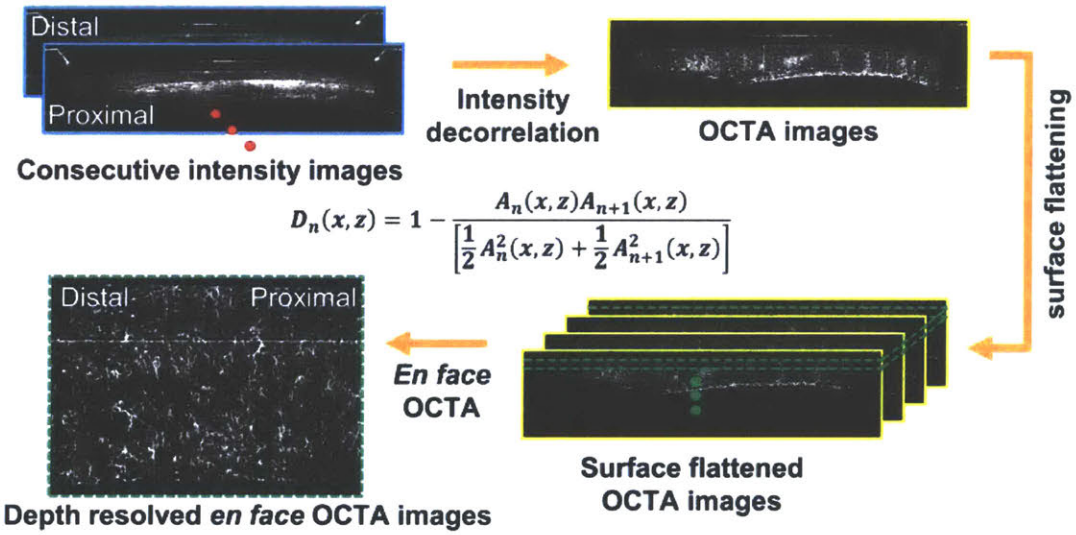

Figure 4.2. Flow chart summarizing the image processing steps for generating depth-resolved *en face* OCT angiography (OCTA) images from the structural volumetric OCT dataset. A_n is linear OCT signal amplitude in individual OCT frames. A nonuniform rotational distortion (NURD) correction algorithm was used prior to calculating decorrelation between consecutive cross-sectional OCT images.

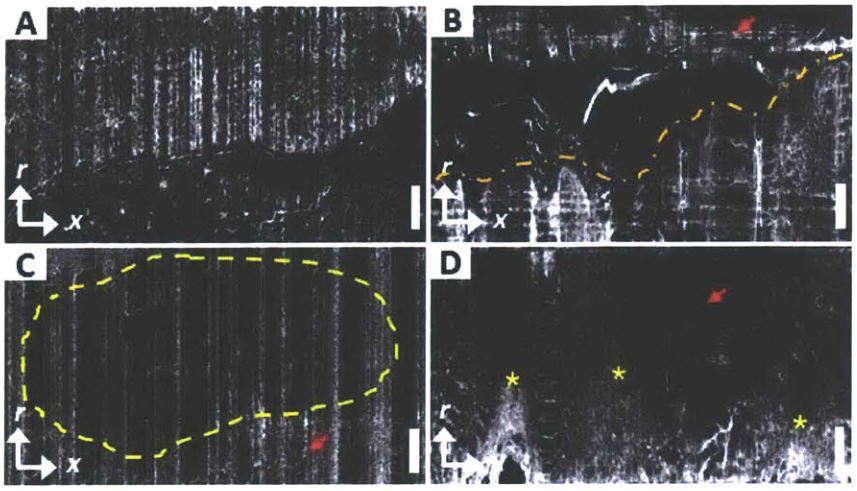

Figure 4.3. Example OCTA images being removed from the study due to inadequate image quality. (A) OCTA image exhibited high noise because of the motion artifacts. (B) OCTA image showed a limited contact between the tissue and the imaging catheter which decreases coverage over the imaged site. Also, the varying tissue contact along the pullback direction can be observed (dashed line) and might be related to the motion issue as well. (C) Low OCTA signals were observed in the middle of the FOV because of the excess pressures exerted by the imaging catheter, which suppresses blood flow of the imaged site. (D) OCTA image exhibited inadequate image quality due to motion issue (stars, high noise) and potentially the pressure issue (arrows, loss of the OCTA signals). Scale bars: 1 mm. r: rotary direction; x: longitudinal (pullback) direction.

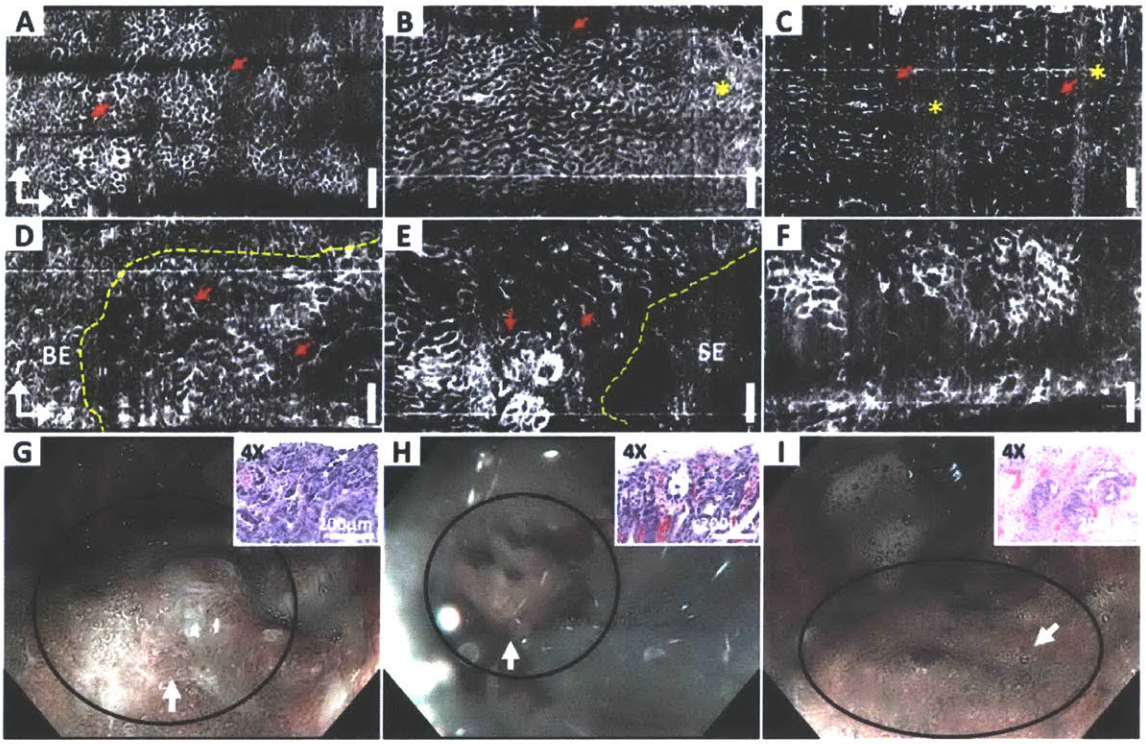

Figure 4.4. *En face* OCT angiography (OCTA) images of (A-C) non-dysplastic BE (NDBE) and (D-F) dysplastic BE (LGD: F; HGD: D, E) from ~180 μm beneath the tissue surface. NDBE exhibits regular honeycomb microvascular pattern (arrows, A-C), similar to previously reported with NBI. The shape of the honeycomb features may be compressed or stretched along the longitudinal direction due to motion artifacts. High decorrelation noise from physiological motion can also be observed (stars, B, C). Abnormal vascular features including (1) abnormal vessel branching (arrows, D), (2) heterogeneous vessel size (arrows, E) or both (F) were shown. OCTA allowed delineation of the boundary between abnormal microvasculature and neighboring non-dysplastic regions (dashed line, D, E). (G-I) NBI images near the imaged sites (D-F) respectively (circles). Scale bars: 1 mm. SE: squamous epithelium. Insets (G, H, I): H&E stained histopathology images of the specimens from the imaged sites corresponding to the histological diagnosis of HGD, HGD, and LGD, respectively. r: rotary direction; x: longitudinal (pullback) direction.

4.6 Tables

Table 4.1. Patient demographics and baseline characteristics.

Patient characteristics (N = 32)	
Age, mean (± SD)	67 (8)
Sex, male, no. (%)	32 (100)
BMI, mean (± SD)	29 (7.1)
Race, white, no. (%)	30 (94)
Baseline pathology	
NDBE, subjects, no. (%)	22 (68.8)
LGD/HGD, subjects, no. (%)	6/4 (31.2)
Length of BE (cm)	
circumferential extent (C), mean (± SD)	3.3 (4.0)
maximum extent (M), mean (± SD)	4.7 (4.0)
Presence of Hiatal Hernia (HH) (N=32)	
Subjects, no. (%)	28 (87.5)
HH length (cm), mean (± SD)	2.1 (2.2)
Number of biopsy/EMR-correlated OCTA dataset per subject	
median (range)	1 (1-7)
Biopsy/EMR specimen characteristics (N=54)	
NDBE, no. (%)	35 (64.8)
from patients with prior EET treatment history, no. (%)	21 (60)
from patients without prior EET treatment history, no. (%)	14 (40)
LGD/HGD, no. (%)	8/11 (35.2)

SD, standard deviation; EMR, endoscopic mucosal resection; EET: endoscopic eradication therapy (including EMR, radiofrequency ablation (RFA), and cryospray ablation (CSA)).

Table 4.2. Demographics of the OCTA datasets.

Histology-OCTA pairs, no.	NDBE	LGD/HGD	Overall
Training session	4	1/1	6
Pretest session	4	0/3	7
Validation session	27	7/7	41

Table 4.3. The performance of the OCTA features for detecting dysplasia in Barrett's esophagus.

Microvascular features	Sensitivity, % (95% CI)	Specificity, % (95% CI)	PPV, % (95% CI)	NPV, % (95% CI)
Feature 1 (branching)	86.9 (79.7-94.1)	77.2 (70.7-83.6)	66.4 (57.5-75.2)	91.9 (87.3-96.5)
Feature 2 (vessel size)	73.8 (64.4-83.2)	87.7 (82.6-92.7)	75.6 (66.3-84.9)	86.6 (81.3-91.8)
Overall				
score ≥2	66.7 (56.6-76.7)	95.7 (92.5-98.8)	88.9 (81.1-96.6)	84.7 (79.5-89.9)
score ≥1	94.0 (89.0-99.1)	69.1 (62.0-76.2)	61.2 (52.8-69.6)	95.7 (92.1-99.4)
High-confidence				
score ≥2	69.9 (59.3-80.4)	96.9 (93.9-99.9)	92.7 (85.9-99.6)	84.9 (79.1-90.7)
score ≥1	93.2 (87.4-98.9)	81.3 (74.5-88.0)	73.9 (64.9-82.9)	95.4 (91.5-99.3)

Overall = score (feature 1) + score (feature 2); PPV: positive predictive value; NPV: negative predictive value.

Table 4.4. The accuracy of individual readers using OCTA features to detect dysplasia in Barrett's esophagus.

score ≥1	Reader 1	Reader 2	Reader 3	Reader 4	Reader 5	Reader 6
Overall						
Sensitivity, %	92.9	92.9	92.9	100	92.9	92.9
Specificity, %	77.8	63	70.4	70.4	63	70.4
PPV, %	68.4	56.5	61.9	63.6	56.5	61.9
NPV, %	95.5	94.4	95	100	94.4	95
High-confidence						
Sensitivity, %	90.9	92.3	92.9	100	91.7	91.7
Specificity, %	80.8	85	89.5	73.1	81	81.3
PPV, %	66.7	80	86.7	61.1	73.3	78.6
NPV, %	95.5	94.4	94.4	100	94.4	92.9

PPV: positive predictive value; NPV: negative predictive value.

Table 4.5. Number of OCTA dataset with corresponding histopathological diagnosis that readers assess with high confidence

High confidence	Reader 1	Reader 2	Reader 3	Reader 4	Reader 5	Reader 6	Overall
Histopathology							
27 NDBE, no. (%)	26 (96.3)	20 (74.1)	19 (70.4)	26 (96.3)	21 (77.8)	16 (59.3)	128(79.0)
7 LGD, no. (%)	6 (85.7)	7 (100)	7 (100)	6 (85.7)	6 (85.7)	6 (85.7)	38(90.5)
7 HGD, no. (%)	5 (71.4)	6 (85.7)	7 (100)	5 (71.4)	6 (85.7)	6 (85.7)	35(83.3)
41 Combined, no. (%)	37 (90.2)	33 (80.5)	33 (80.5)	37 (90.2)	33 (80.5)	28 (68.3)	201 (81.7)

Table 4.6. The accuracy of the OCTA criteria including all NDBE datasets as well as datasets from patients without a history of dysplasia and history of dysplasia/EET.

Dysplasia hx (Score ≥1)	Sensitivity, % (95% CI)	Specificity, % (95% CI)	PPV, % (95% CI)	NPV, % (95% CI)
Combined (N=41)	94.0 (89.0-99.1)	69.1 (62.0-76.2)	61.2 (52.8-69.6)	95.7 (92.1-99.4)
NDBE (w/o EET hx, N=26)	94.0 (89.0-99.1)	66.7 (55.8-77.6)	76.7 (68.5-84.9)	90.6 (82.7-98.4)
NDBE (w/ EET hx, N=29)	94.0 (89.0-99.1)	71.1 (61.7-80.5)	75.2 (67.0-83.5)	92.8 (86.6-98.9)

NDBE (w/o EET hx) and NDBE (w/ EET hx): subset analysis where only NDBE datasets from patients without prior history of dysplasia vs. with a history of dysplasia/endoscopic eradication therapy, respectively. hx: history.

Table 4.7. Reading time per reader in the validation session.

score ≥1	Reader 1	Reader 2	Reader 3	Reader 4	Reader 5	Reader 6	Overall
Per OCTA dataset* mean (SD), secs	29 (19)	59 (26)	43 (26)	33 (14)	57 (26)	46 (23)	45 (25)
Overall reading time initial reading, mins	20	40	29	23	39	32	30.5 (7.5)
final reading, mins	19	22	21	15	31	30	23.0 (5.7)

*analysis based on the initial readings; SD: standard deviation; secs: seconds; mins: minutes.

Table 4.8. The overall distribution of the abnormal microvascular features on the subgroups of LGD and HGD pathologies.

	(1) Abnormal vessel branching		(2) Heterogeneous vessel size	
	LGD	HGD	LGD	HGD
Present, %	83.3	90.5	71.4	76.2
Absent, %	16.7	9.5	28.6	23.8
	p-value: 0.33		*p*-value: 0.62	

Table 4.9. The overall accuracy of using OCTA on the subgroups of LGD and HGD pathologies.

Score ≥ 1	Sensitivity, %	Specificity, %	PPV, %	NPV, %
LGD vs. NDBE	88.1	69.1	42.5	95.7
HGD vs. NDBE	100.0	69.1	45.7	100

PPV: positive predictive value; NPV: negative predictive value.

Table 4.10. The accuracy of individual readers using OCTA features to detect dysplasia in the OCTA datasets of BE from the initial reading.

score ≥1	Reader 1	Reader 2	Reader 3	Reader 4	Reader 5	Reader 6	Combined
Overall Sensitivity, %	71.4	92.9	85.7	100	92.9	85.7	88.1
Specificity, %	88.9	59.3	77.8	63	59.3	55.6	67.3
PPV, %	76.9	54.2	66.7	58.3	54.2	50	58.3
NPV, %	85.7	94.1	91.3	100	94.1	88.2	91.6

PPV: positive predictive value; NPV: negative predictive value.

4.7 Appendix – OCTA Reading Protocol (Training Materials)

En face OCTA image reading protocol

Hsiang-Chieh Lee

2016

1

Esophagus Pathology and BE Progression

- Normal Esophagus
  - Multilayer architecture comprises of squamous epithelium (SE), lamina propria (LP), muscularis mucosa (MM), and submucosa (SM)

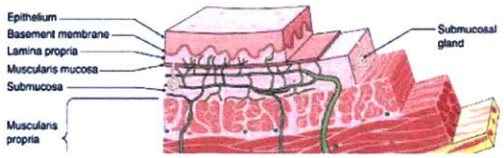

- Barret's Esophagus (BE):
  - Chronic gastroesophageal reflux disease (GERD)
  - Normal SE → Intestinal metaplasia
  - Increased risk of esophageal caner
  - Pathology features during BE progression
    - Increased cytological atypia (not visible on OCT)
    - Distorted glandular structures
    - ***Increased microvessel density (MVD)***

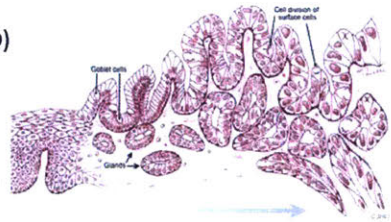

http://www.clevelandclinicmeded.com/medicalpubs/diseasemanagement/hematology-oncology/esophageal-cancer/Default.htm
http://pathology2.jhu.edu/beweb/cancer.cfm

2

Esophagus Pathology and BE Progression

- Normal Esophagus
  - Multilayer architecture comprises of squamous epithelium (SE), lamina propria (LP), muscularis mucosa (MM), and submucosa (SM)

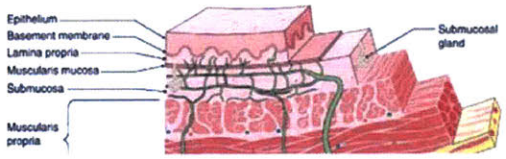

- Barret's Esophagus (BE):
  - Chronic gastroesophageal reflux disease (G
  - Normal SE → Intestinal metaplasia
  - Increased risk of esophageal caner
  - Pathology features during BE progression
    - Increased cytological atypia (not visible on
    - Distorted glandular structures
    - ***Increased microvessel density (MVD)***

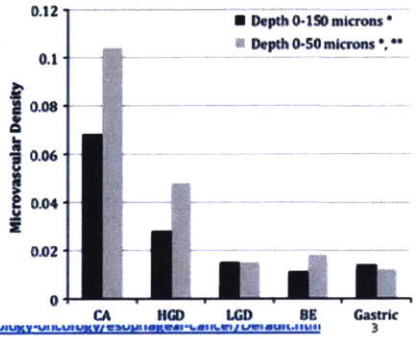

http://www.clevelandclinicmeded.com/medicalpubs/diseasemanagement/hematology-oncology/esophageal-cancer/Default.htm
http://pathology2.jhu.edu/beweb/cancer.cfm

Magnification Narrow Band Imaging (NBI) – I

- Principle:
  - Based on the characteristic that the penetration depth is a function of light wavelength. Blue light exhibits shorter penetration depth compared to green light → blue allows for optimal superficial imaging.

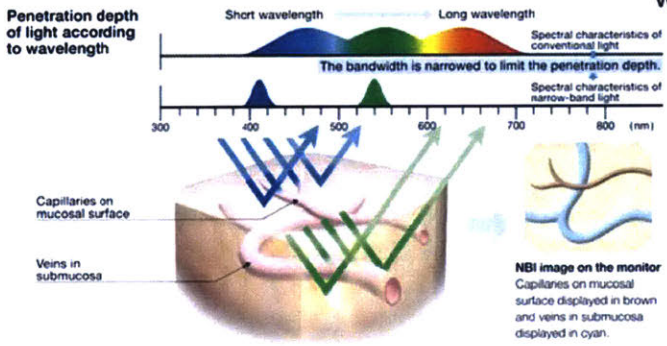

WLE: white light endoscopy

  - In addition, NBI reveals the superficial vasculature due to the strong absorption of the blue light by hemoglobin.

http://www.intechopen.com/books/endoscopy/narrow-band-imaging-nbi-endoscopic-method-for-detection-of-head-and-neck-cancer
http://www.sied.it/index.cfm?object=sp&spid=295

Magnification Narrow Band Imaging (NBI) – II

- Kara et al. GIE 2006

NDBE

HGD

5

Kara et al. 06 Gastrointestinal Endoscopy, "Detection and classification of the mucosal and vascular patterns (mucosal morphology) in Barrett's esophagus by using narrow band imaging."

Magnification Narrow Band Imaging (NBI) – II

- Kara et al. GIE 2006

NDBE

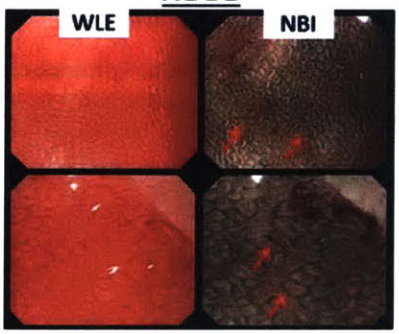

- Regular honeycomb patterns (vessels situated regularly along the mucosal folds (pits))
- Absence of abnormal vessels

HGD

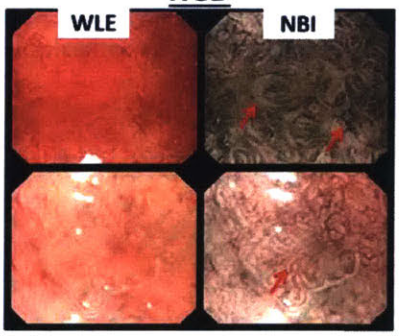

- Irregular/disorganized vessels not regularly along the mucosal folds (pits))
- Presence of abnormal vessels, e.g.
  - Different calibers
  - Small isolated vessel
  - Crowed vessels

Kara et al. 06 Gastrointestinal Endoscopy, "Detection and classification of the mucosal and vascular patterns (mucosal morphology) in Barrett's esophagus by using narrow band imaging."

6

Magnification Narrow Band Imaging (NBI) – II

- Kara et al. GIE 2006

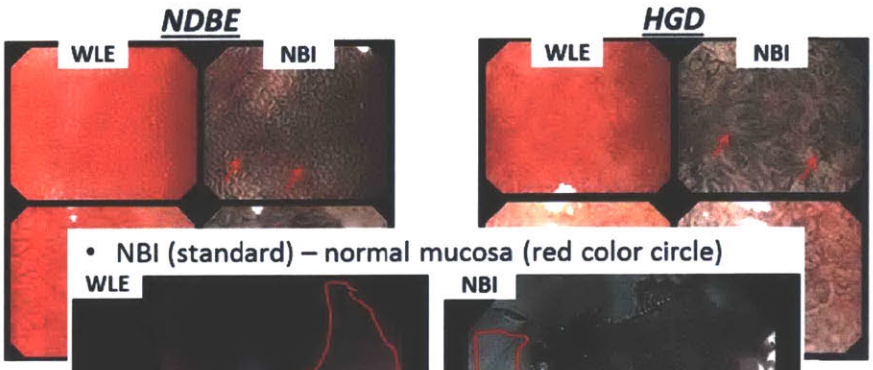

- NBI (standard) – normal mucosa (red color circle)

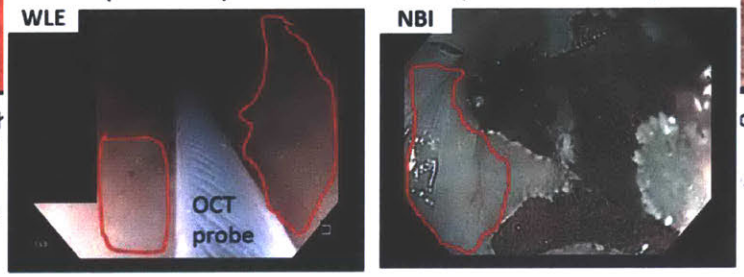

- Regular h … ot regularly situated (pits))
- Absence … .g.

Kara et al. 06 Gastroirtestinal Endoscopy, "Detection and classification of the mucosal and vascular patterns (mucosal morphology) in Barrett's esophagus by using narrow band imaging."

Magnification Narrow Band Imaging (NBI) – III

- Sharma et al. GIE 2006
  - **Normal vascularity**: presence of thin vessels with a uniform branching pattern
  - **Abnormal vascularity**: dilated, corkscrew vessels with increased vascularity and abnormal, non-uniform branching pattern.
  - Correlation between vascular pattern and histopathology:

NBI pattern	N	IM	LGD	HGD	CM
Normal vascularity	75	45	16	0	14
Abnormal vascularity	38	0	2	36	0

N, Number of areas evaluated with NBI; *IM*, intestinal metaplasia; *CM*, cardiac mucosa.

- Singh et al. Endoscopy 2011
  - **Regular vascular pattern**: blood vessels situated along or/between mucosal folds
  - **Irregular vascular pattern**: focally or diffusely irregularly distributed vessels

Key message from NBI literatures:
The "irregularity/non-uniformity" is more important than a specific vascular pattern for the detection/differentiation of dysplasia

Sharma et al. 06 Gastrointestinal Endoscopy, "The utility of a novel narrow band imaging endoscopy system in patients with BE."
Singh et al. 11 Endoscopy, "Observer agreement in the assessment of narrowband imaging system surface patterns in BE: a multicenter study."

(Magnification) Narrow Band Imaging (NBI) – IV

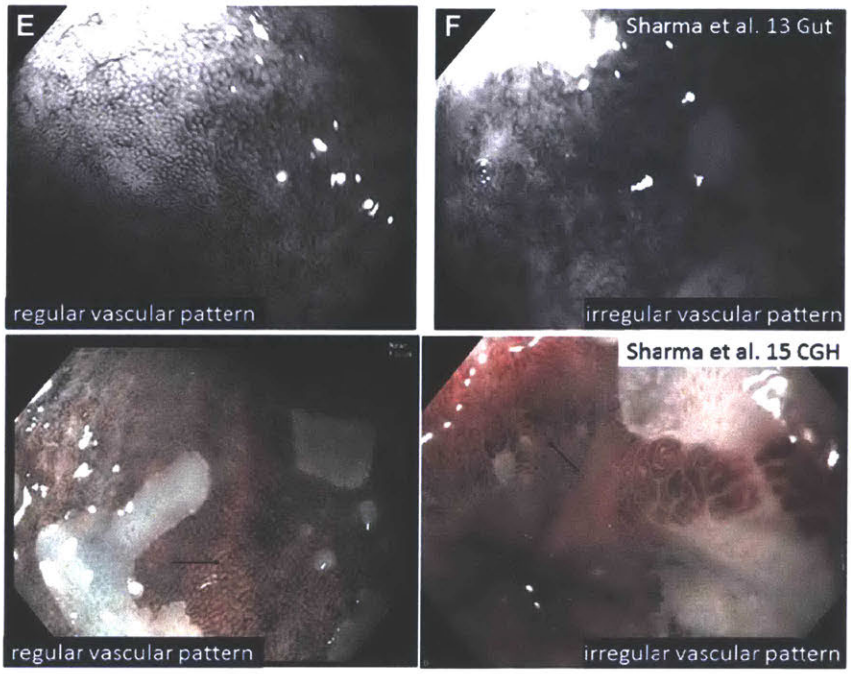

Endoscopic Optical Coherence Tomography (OCT)

- Optical coherence tomography is a non-invasive imaging technique that can provide two- and three-dimensional information of the tissue architectures with resolution close to histopathology in real time.
- The imaging principle of OCT is similar to ultrasound while OCT measures the echo time delay with light, enabling better imaging resolution.
- Using fiber-optic imaging catheter, endoscopic OCT can provide 3D images of the human gastrointestinal (GI) tract.

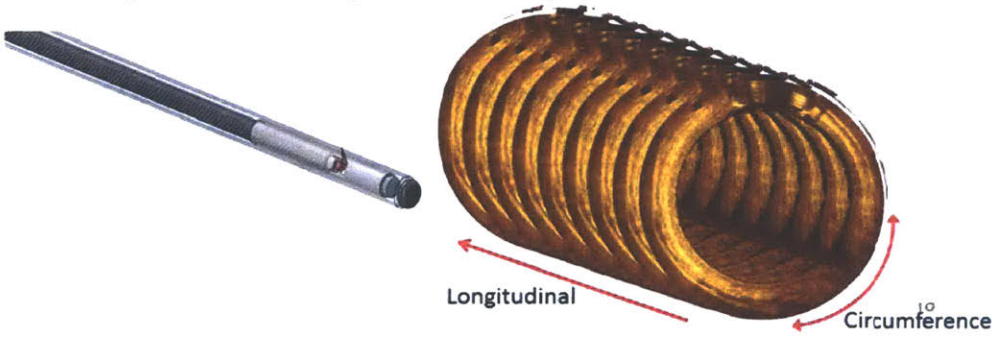

Microvasculature feature of BE pathologies – I

- Squamous epithelium:
  - Superficial (image number ≤ 30) pillar (papillary) like vascular pattern, which is an exclusive feature for normal SE.

Esophagus (HE stain)[1]

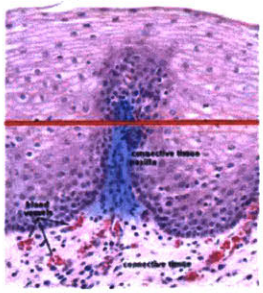

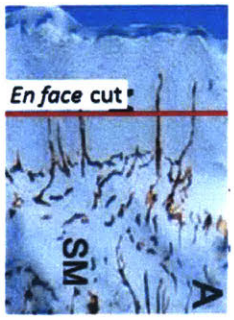

11

Microvasculature feature of BE pathologies – I

- Squamous epithelium:
  - Superficial (image number ≤ 30) pillar (papillary) like vascular pattern, which is an exclusive feature for normal SE.
- Non-dysplastic Barrett's esophagus :
  - Regularly distributed oval/honeycomb like vascular pattern (non distorted).
  - For different cases of NDBE, the size of individual oval/honeycombs might vary.

Examples (will be shown in the training sets later also):

Regular (no motion artifact)

(a) (b)

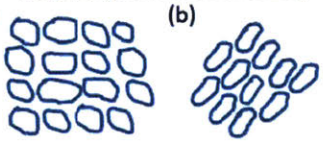

The size of individual honeycomb is similar to each within the FOV.

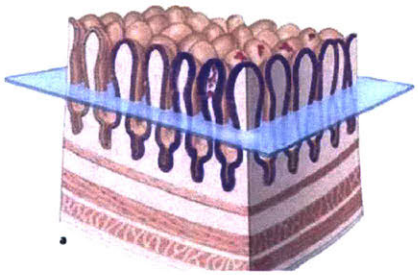

12

Microvasculature feature of BE pathologies – I

- Squamous epithelium:
  - Superficial (image number ≤ 30) pillar (papillary) like vascular pattern, which is an exclusive feature for normal SE.
- Non-dysplastic Barrett's esophagus :
  - Regularly distributed oval/honeycomb like vascular pattern (non distorted).
  - For different cases of NDBE, the size of individual oval/honeycombs might vary.
  - The size of ovals/honeycombs may vary slightly between different regions/zones in a single en face OCTA image due to motion artifacts.

Examples (will be shown in the training sets later also):

Regular (no motion artifact)

(a) (b)

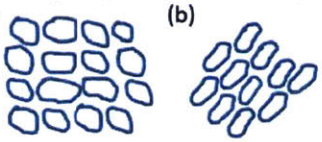

The size of individual honeycomb is similar to each within the FOV.

Regular (with motion artifact)

(c) (d)

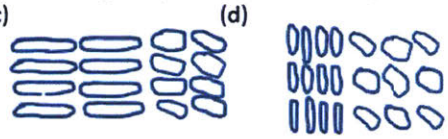

The shape of the honeycombs might be either stretched or compressed due to the motion artifacts but are still regular distributed.

13

Microvasculature feature of BE pathologies – II

- Distorted vascular patterns (superficial vasculature):
  1. **Abnormal vessel branching (disorganized vessels)**
  2. **Heterogeneous vessel size (wide variation in vessels size)**
- Large abnormal branching in the deep vasculature (image number > 30) is not characteristic feature of distorted vascular pattern.

Examples:

- Abnormal vessel branching

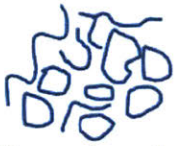

- Abnormal vessel branching

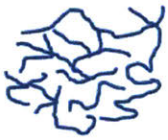

- Abnormal vessel branching

- Heterogeneous vessel size

- Heterogeneous vessel size

- Abnormal vessel branching
- Heterogeneous vessel size

14

Annotations

- Yellow color box: normal vascular pattern,
- Orange color box: motion/imaging artifacts
- Red color box: abnormal vascular patterns
- LP: lamina propria; MM: muscularis mucosa

Distal

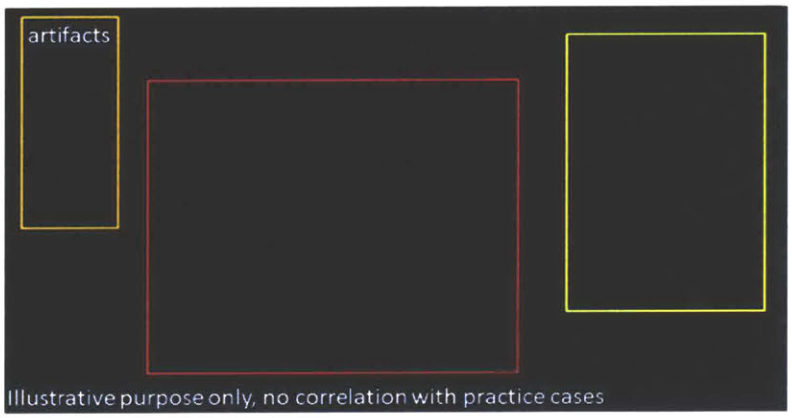

Proximal

15

Normal Squamous (SE)

Distal

Proximal

Image depth: 180 μm (OCTA_018.pgm)

16

Normal Squamous (SE, summary)

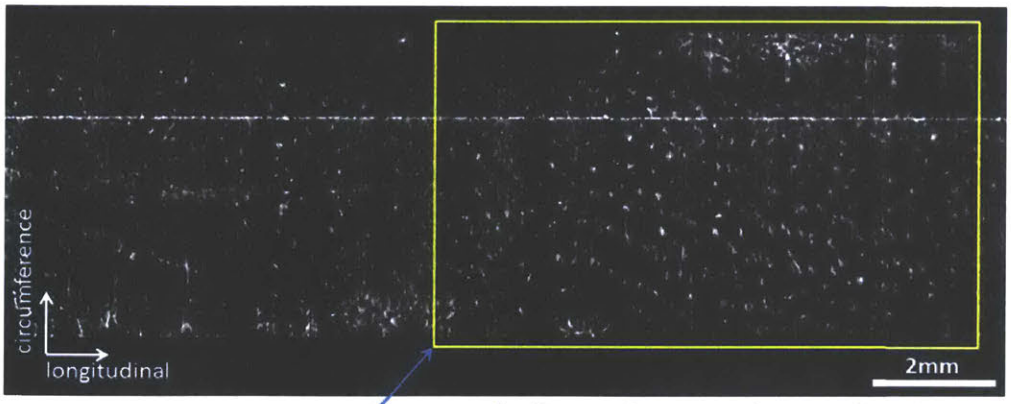

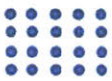

Pillar like pattern

- Pillar like vascular pattern elongating from the LP to the surface of the epithelium
- Reminiscent the distribution of lamina papillae in normal esophagus
- Patterns seen on OCTA dataset of SCJ (BE → SE) or BE island (SE → BE)

Image depth: 180 µm (OCTA_018.pgm)

17

En face OCTA image reviewing sequence

- **Read *en face* OCTA images <u>specifically in the superficial vasculature epithelium</u> from Set XX_OCTA_001.pgm → Set XX_OCTA_ 030.pgm (i.e. image numbers 01-30). <u>DO NOT read deep vasculature (i.e. image numbers 31-70) at this step, since this corresponds to the muscularis mucosa.</u>**

- **Evaluate the presence of 2 possible different vascular features around the medium depth level of the <u>superficial vasculature epithelium</u> (Set XX_OCTA_011.pgm → Set XX_OCTA_020 (+/-2).pgm).**
  1. **Abnormal vessel branching**
  2. **Heterogeneous vessel size**

18

Non-dysplastic BE (NDBE) – 01

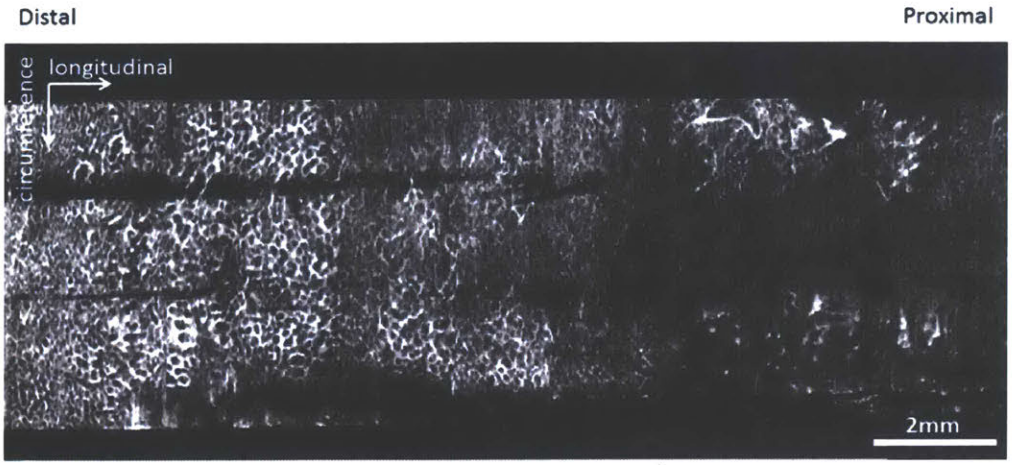

Image depth: 160 µm (OCTA_016.pgm)

19

NDBE – 01 (cont'd)

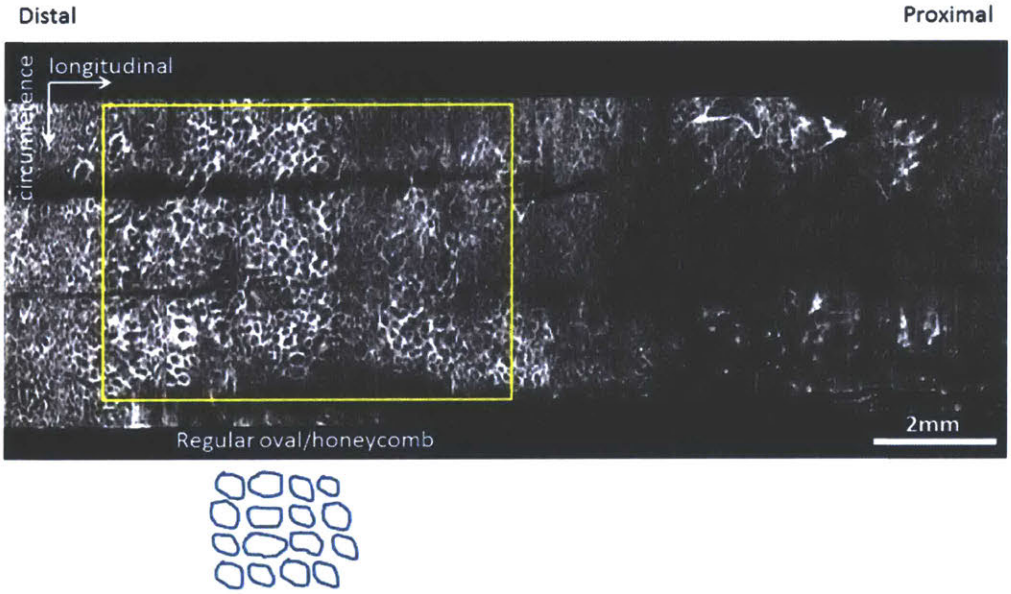

Image depth: 160 µm (OCTA_016.pgm)

20

NDBE – 01 (cont'd)

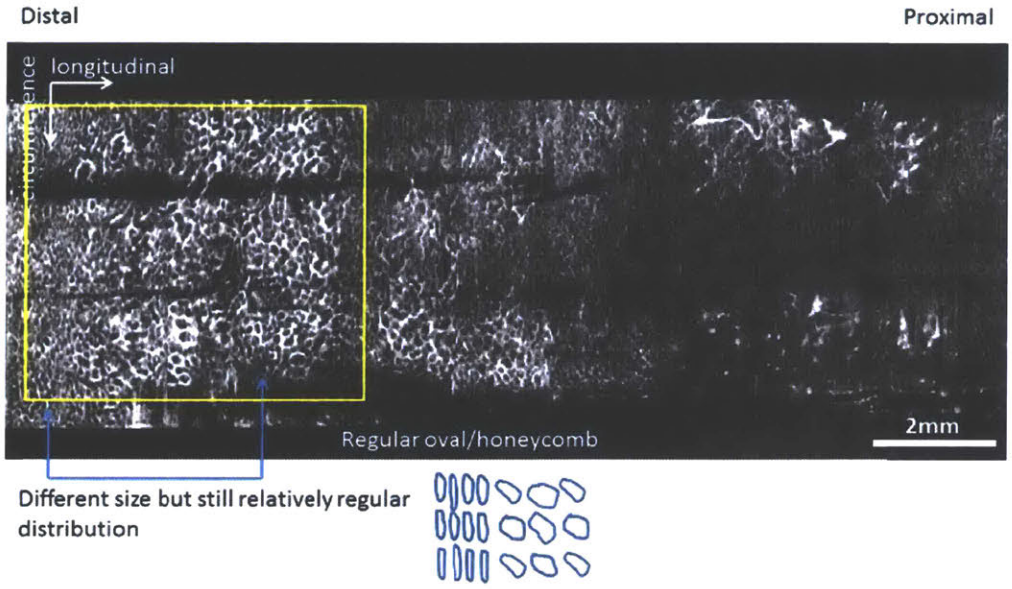

Image depth: 160 µm (OCTA_016.pgm)

21

NDBE – 01 (cont'd)

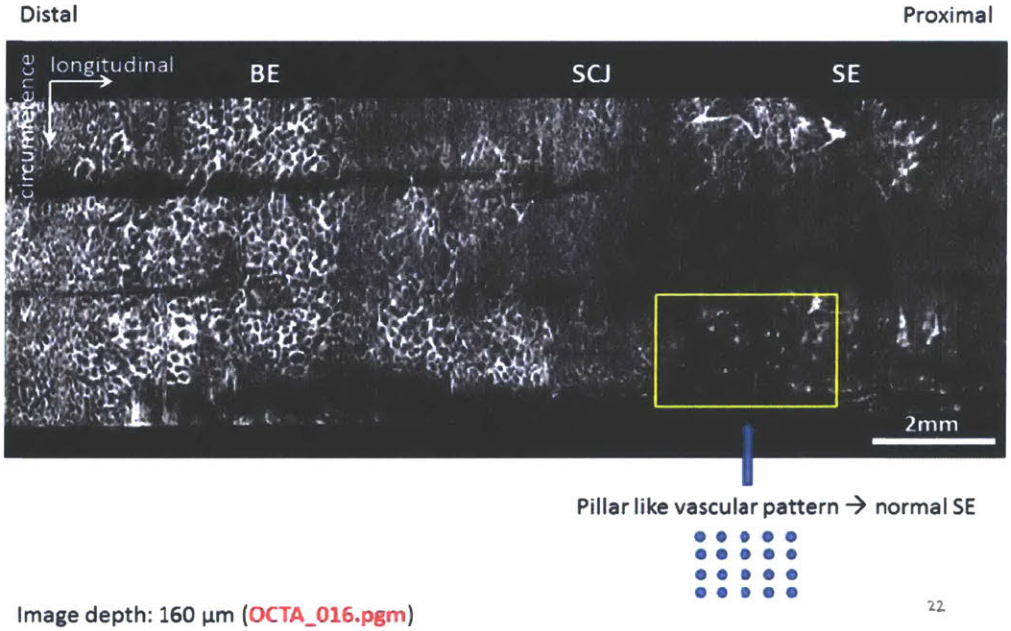

Image depth: 160 µm (OCTA_016.pgm)

22

NDBE – 01 (cont'd)

Distal Proximal

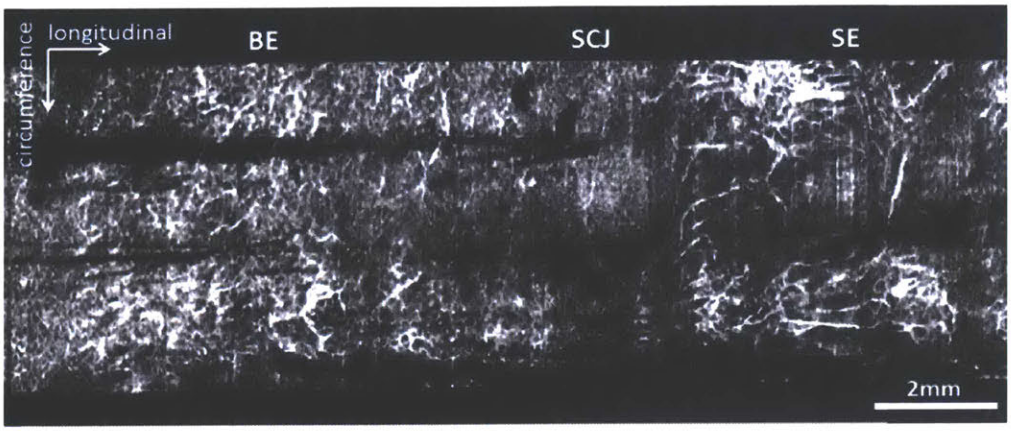

- Deep vasculature (image number 31-70) shows complex vasculature within the LP/MM layer. This is common feature across all OCTA sets.
- After scrolling through the top 30 frames (image number 1-30), please asses the presence of abnormal vascular features in the medium depth level (image number 11-20 +/-2 frames)

Image depth: 350 μm (OCTA_035.pgm)

23

NDBE – 01 (summary)

Distal Proximal

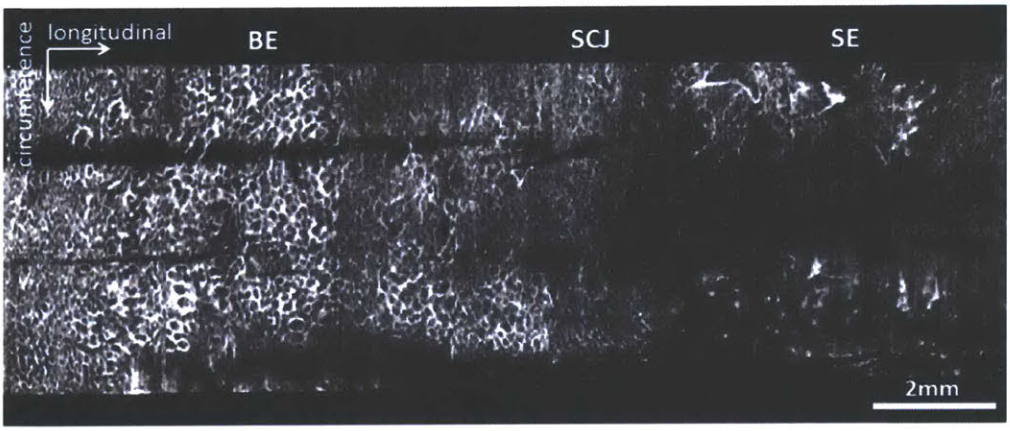

Key message from this set:

- Regular honeycomb vascular pattern
- Vascular feature of SCJ
- Variation of the honeycomb patterns due to motion

Image depth: 160 μm (OCTA_016.pgm)

24

NDBE – 02

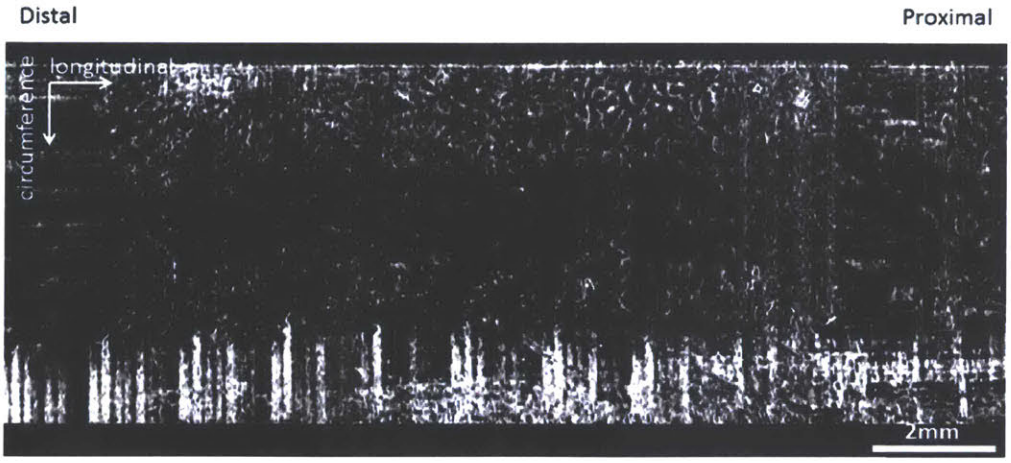

Image depth: 150 µm (OCTA_015.pgm)

25

NDBE – 02 (cont'd)

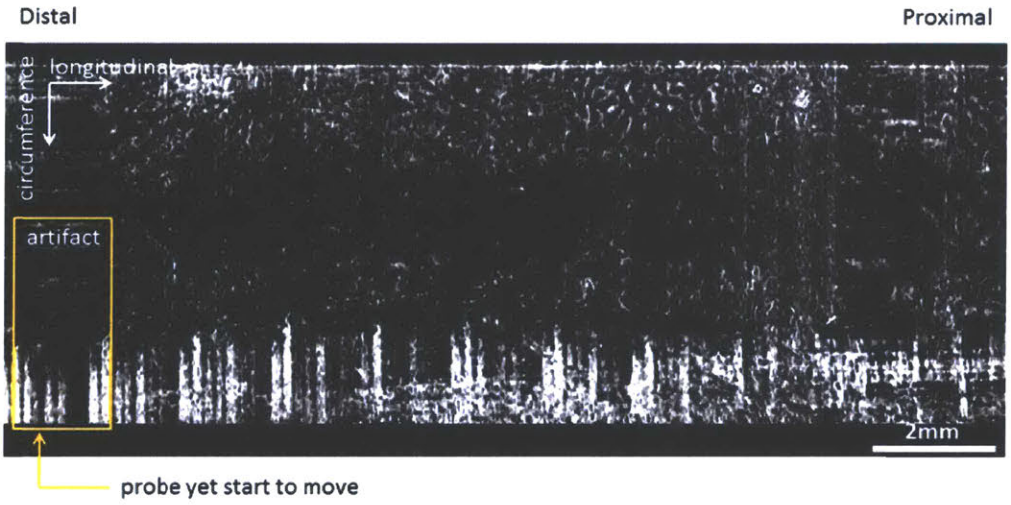

Image depth: 150 µm (OCTA_015.pgm)

26

NDBE – 02 (cont'd)

Distal Proximal

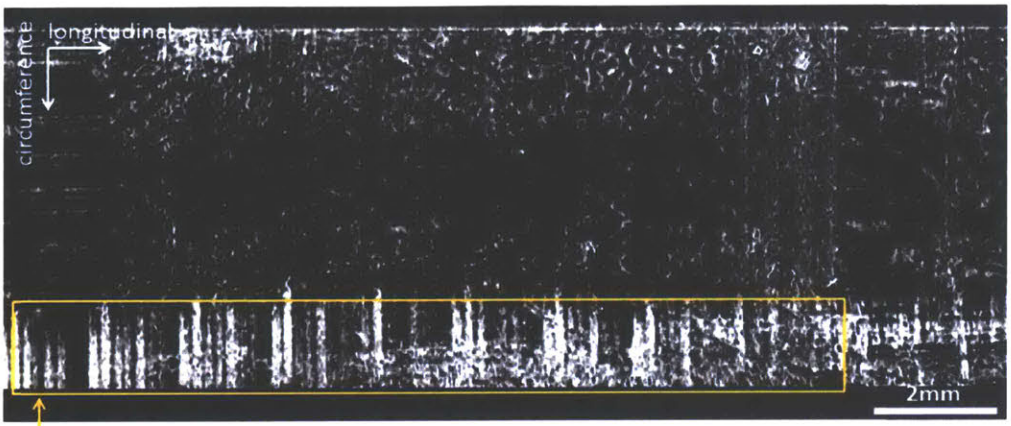

High signal in the very beginning of the dataset → light reflection from probe sheath

Image depth: 150 µm (OCTA_015.pgm)

27

NDBE – 02 (cont'd)

Distal Proximal

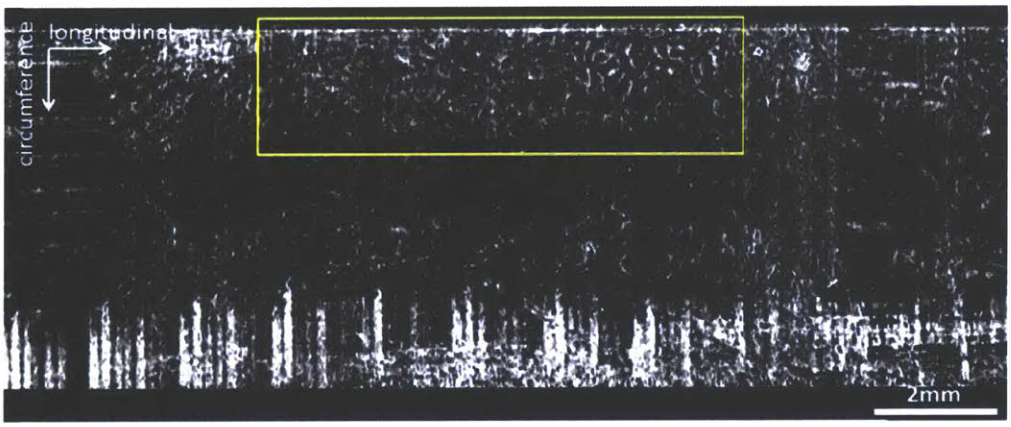

- Relatively regular honeycomb vascular pattern along a small fraction of the circumference

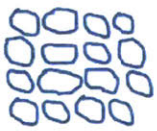

Image depth: 150 µm (OCTA_015.pgm)

28

NDBE – 02 (cont'd)

Distal Proximal

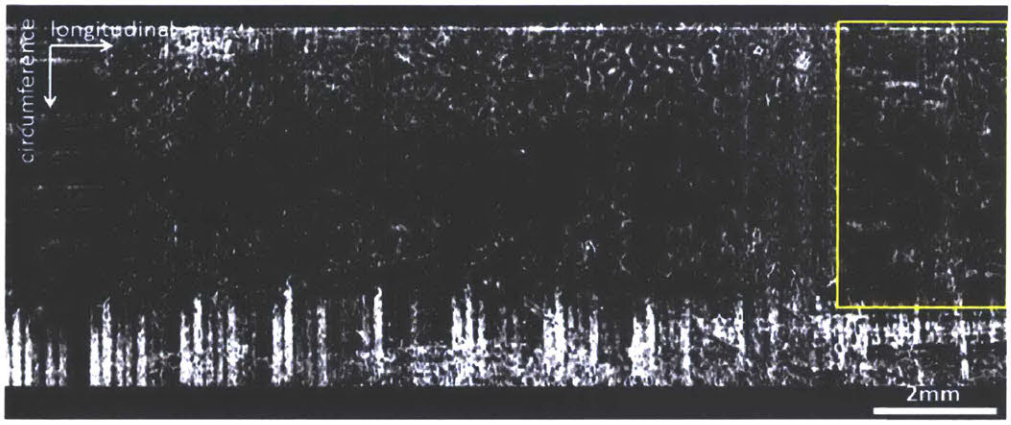

- Relatively regular honeycomb vascular pattern

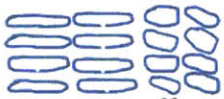

Image depth: 150 µm (OCTA_015.pgm)

29

NDBE – 02 (summary)

Distal Proximal

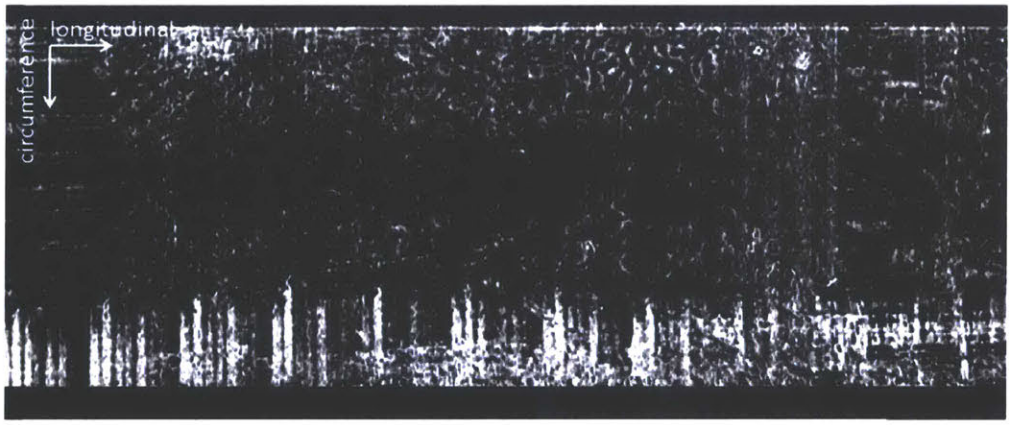

Key message from this set:

- Regular honeycomb vascular pattern
- Patterns where the probe yet start to move

Image depth: 150 µm (OCTA_015.pgm)

30

NDBE – 03

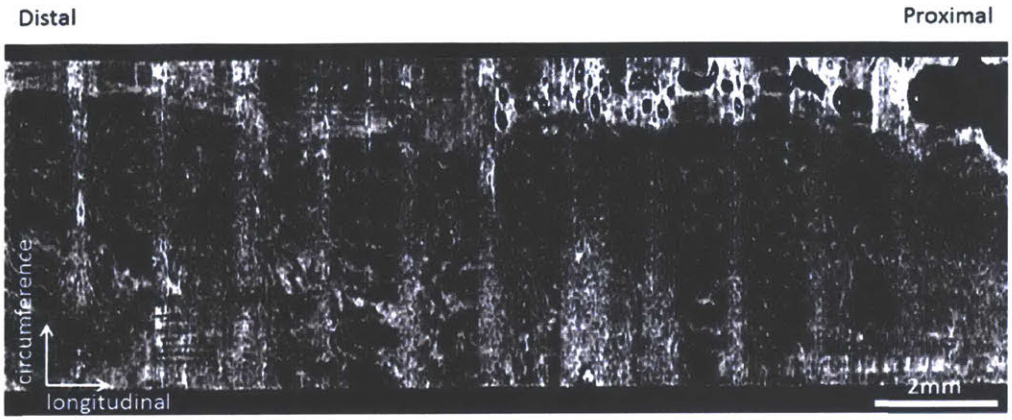

Image depth: 200 μm (OCTA_020.pgm)

31

NDBE – 03 (cont'd)

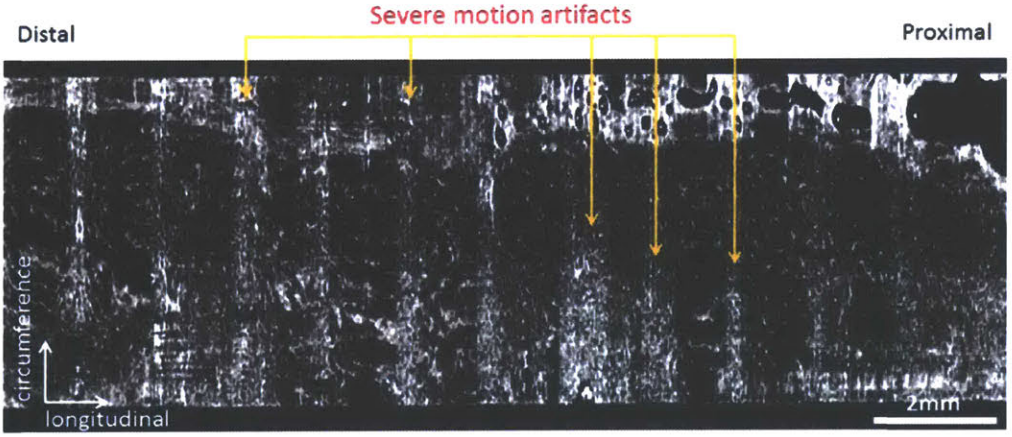

kind of periodic motion artifact here → from cardiac motion potentially

Image depth: 200 μm (OCTA_020.pgm)

32

NDBE – 03 (cont'd)

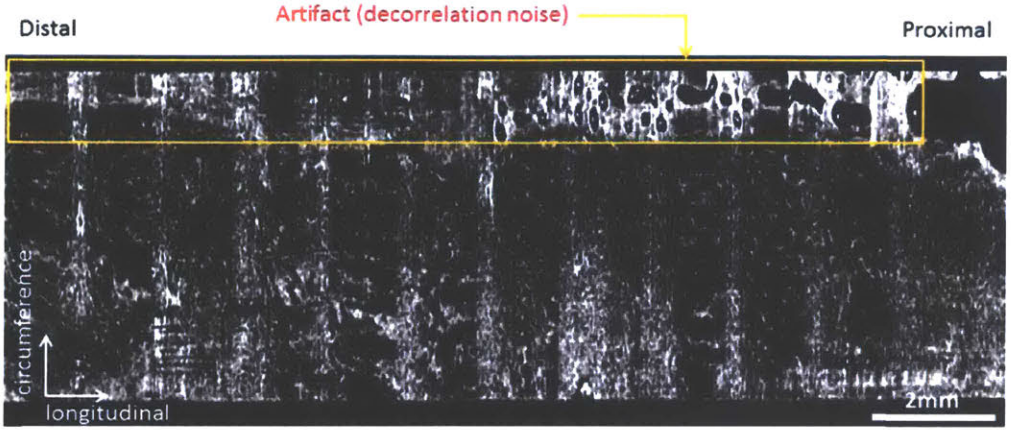

High decorrelation signal identified in the very beginning of the dataset:

- Region of tissue not fully in contact with the probe (tissue boundary)

Image depth: 200 µm (OCTA_020.pgm)

33

NDBE – 03 (cont'd)

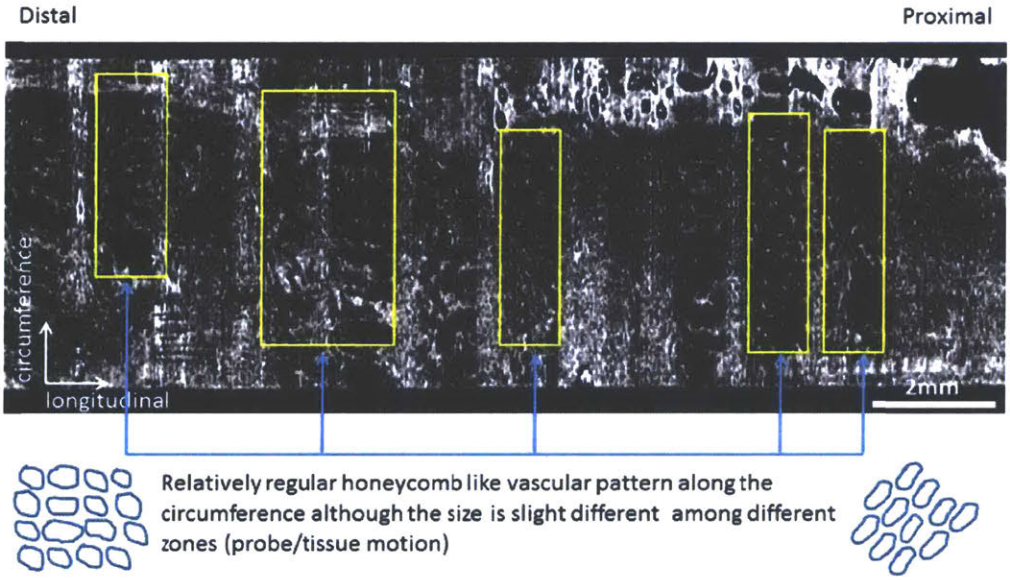

Relatively regular honeycomb like vascular pattern along the circumference although the size is slight different among different zones (probe/tissue motion)

Image depth: 200 µm (OCTA_020.pgm)

34

NDBE – 03 (summary)

Distal Proximal

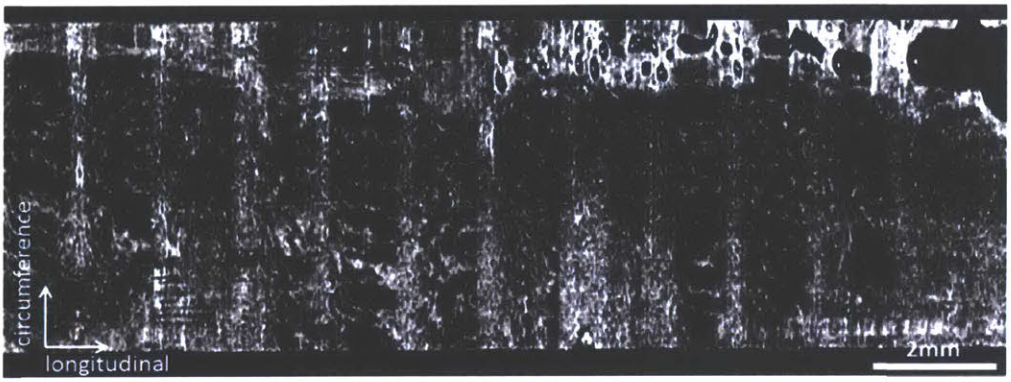

Key message from this set:

- Regular honeycomb vascular pattern
- Variation of honeycomb patterns due to motion
- the motion artifact is kind of periodic in this set

Image depth: 200 μm (OCTA_020.pgm)

35

NDBE – 04

Distal Proximal

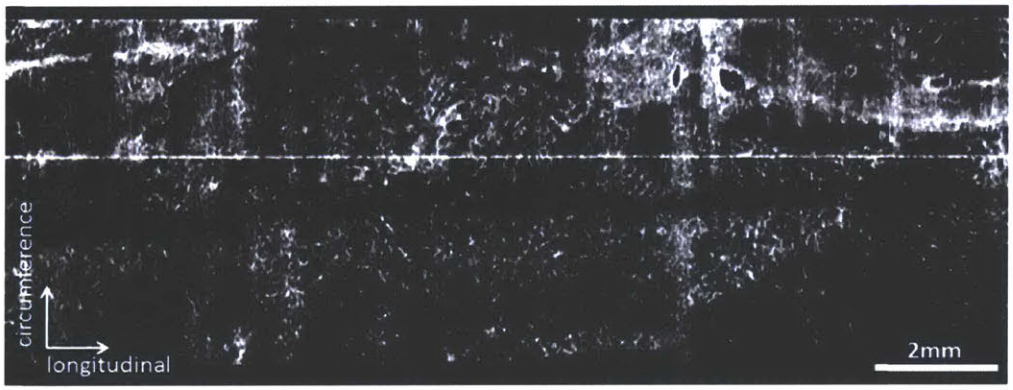

Image depth: 180 μm (OCTA_018.pgm)

36

NDBE – 04 (cont'd)

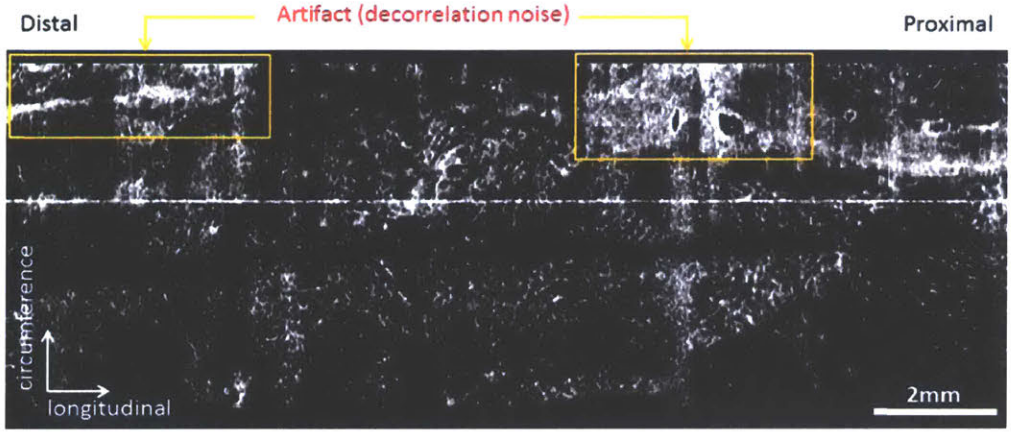

High decorrelation signal identified in the very beginning of the dataset:

- Region of tissue not fully in contact with the probe
- High light reflection signal from the sheath

Image depth: 180 µm (OCTA_018.pgm)

37

NDBE – 04 (cont'd)

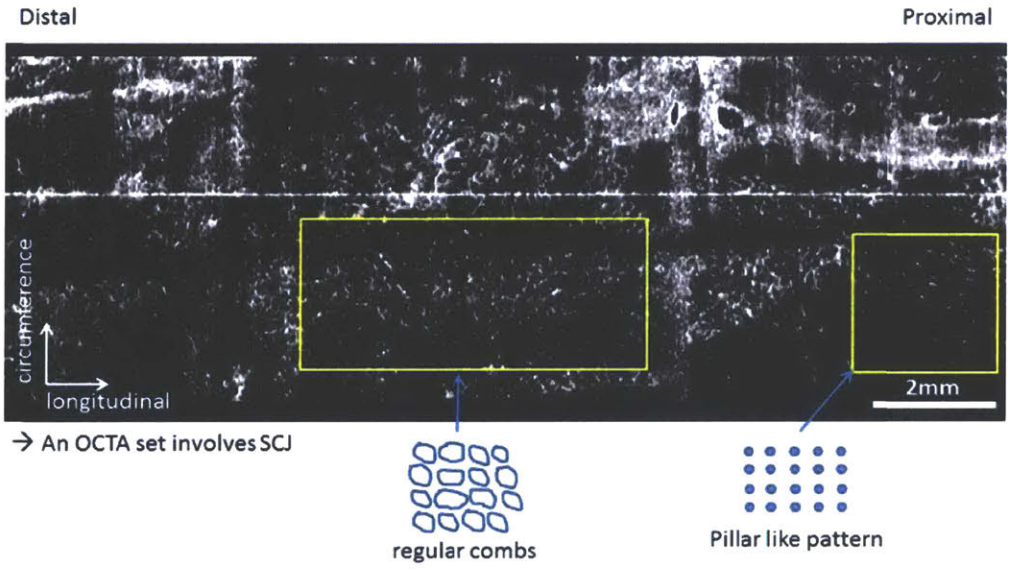

Image depth: 180 µm (OCTA_018.pgm)

38

NDBE – 04 (cont'd)

Distal Proximal

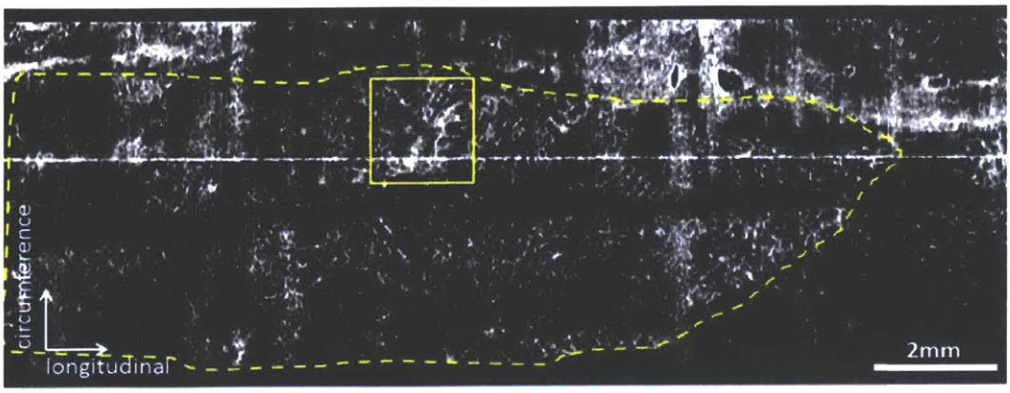

→ a small foci showing slightly abnormal branching and variation in vessel size

→ however, this single region and size is small, so this might be due to the nature in NDBE

Image depth: 180 μm (OCTA_018.pgm)

39

NDBE – 04 (summary)

Distal Proximal

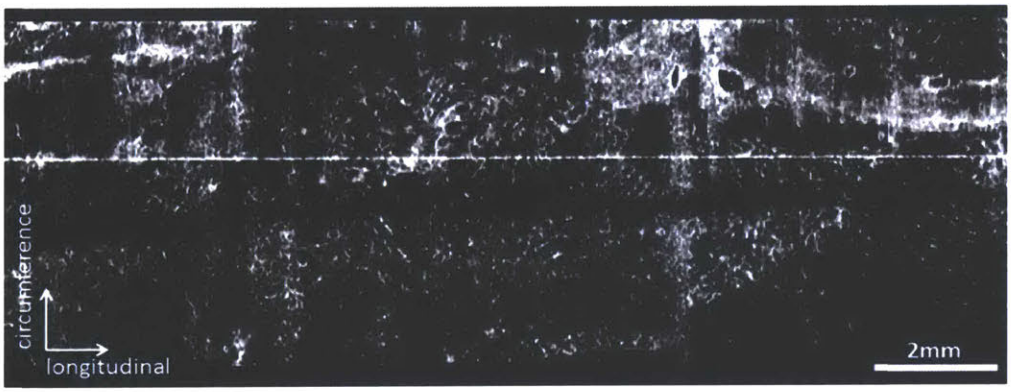

Key message from this set:

- Characteristic microvascular pattern of a benign SCJ (NDBE)
- Patterns where the tissue not fully in contact with the probe
- If only a small foci shows the presence of either features → consider as benign case,

Image depth: 180 μm (OCTA_018.pgm)

40

Low-grade Dysplasia (LGD) – 01

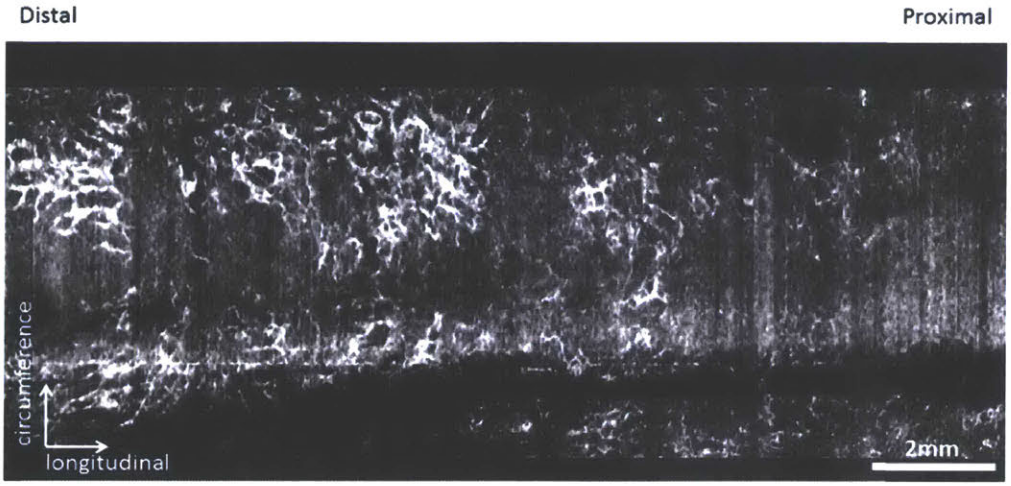

Image depth: 170 µm (OCTA_017.pgm)

41

LGD – 01 (cont'd)

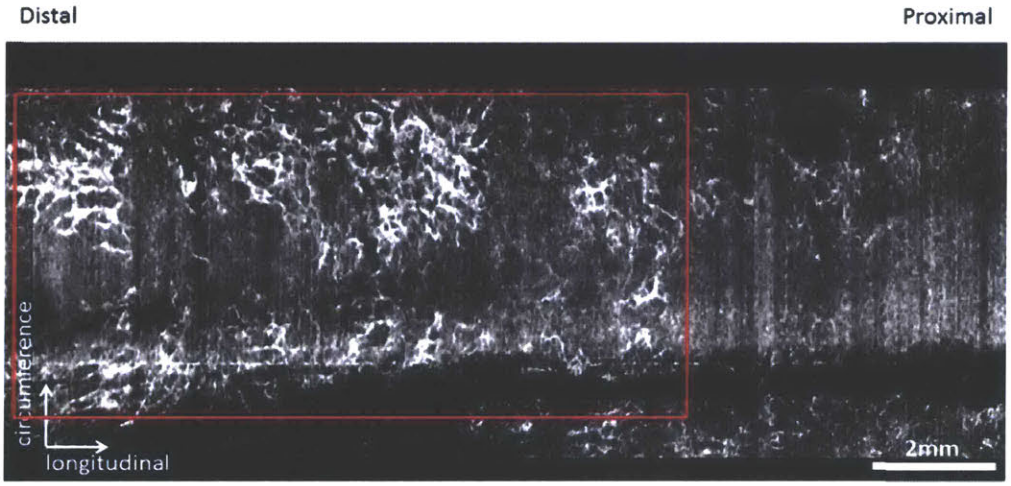

Distorted vascular pattern = abnormal vessel branching

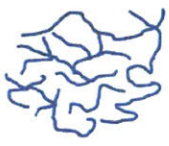

Image depth: 170 µm (OCTA_017.pgm)

42

LGD – 01 (cont'd)

Distal Proximal

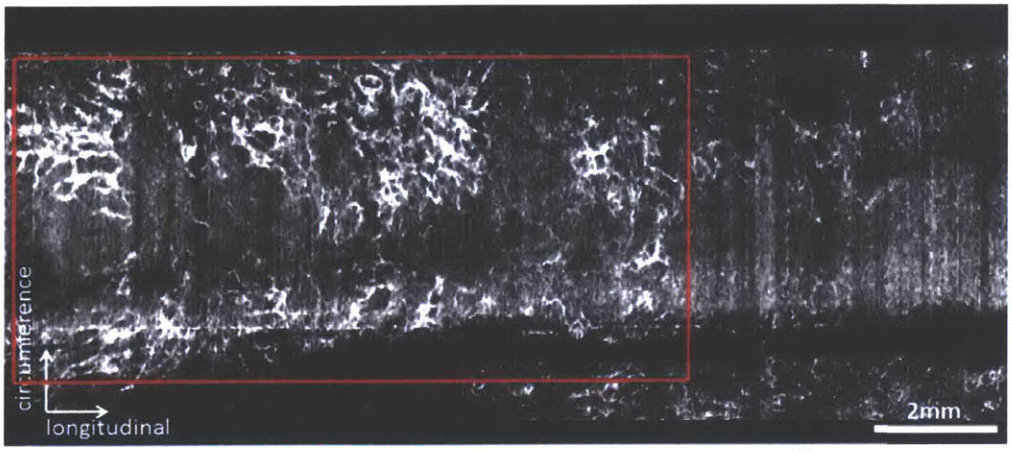

Distorted vascular pattern = heterogeneous vessel size

Image depth: 170 μm (OCTA_017.pgm)

43

LGD – 01 (summary)

Distal Proximal

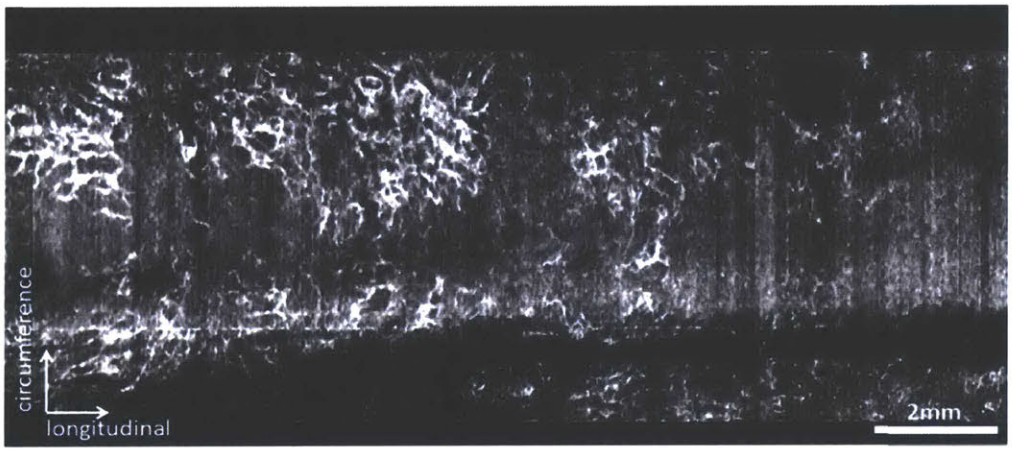

- **Distorted vascular pattern:** abnormal vessel branching (square box) + heterogeneous vessel size (elliptical box)
- When you **distorted vascular pattern,** mark regions of each vasculature feature

Image depth: 170 μm (OCTA_017.pgm)

44

High-grade Dysplasia (HGD) – 01

Distal Proximal

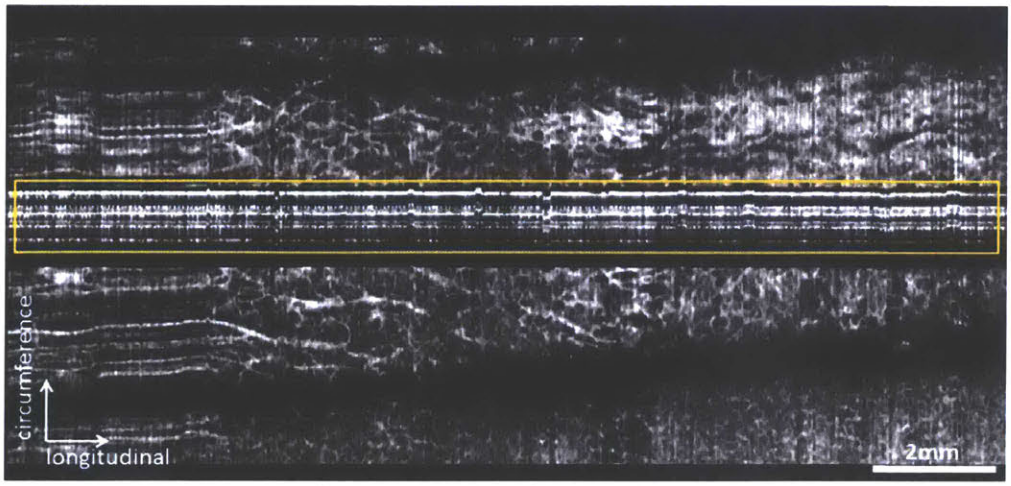

Horizontal lines in the middle of FOV: artifacts from the mechanical strut in the imaging probe. Ignore this part.

Image depth: 190 μm (OCTA_019.pgm)

45

HGD – 01 (cont'd)

Distal Proximal

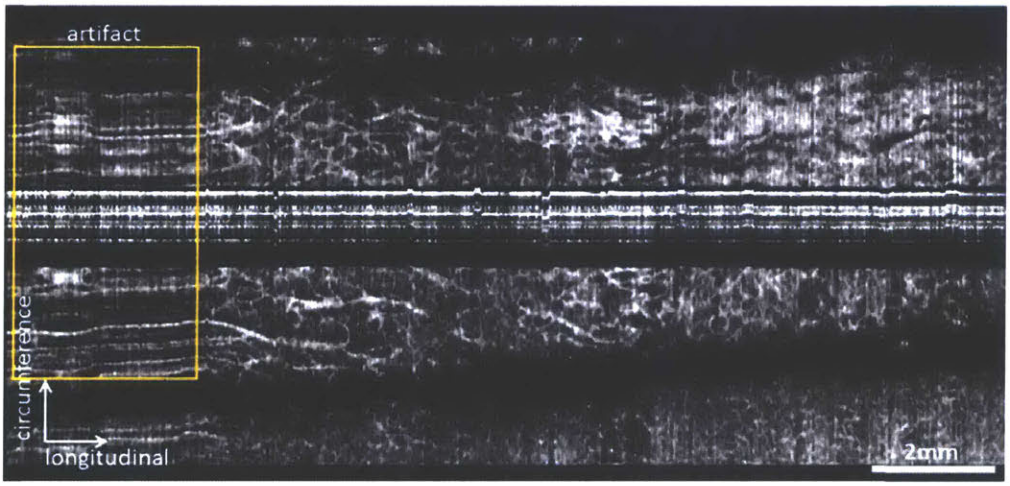

Horizontal lines in the middle of FOV: artifacts from the mechanical strut in the imaging probe. Ignore this part.

Image depth: 190 μm (OCTA_019.pgm)

46

HGD – 01 (cont'd)

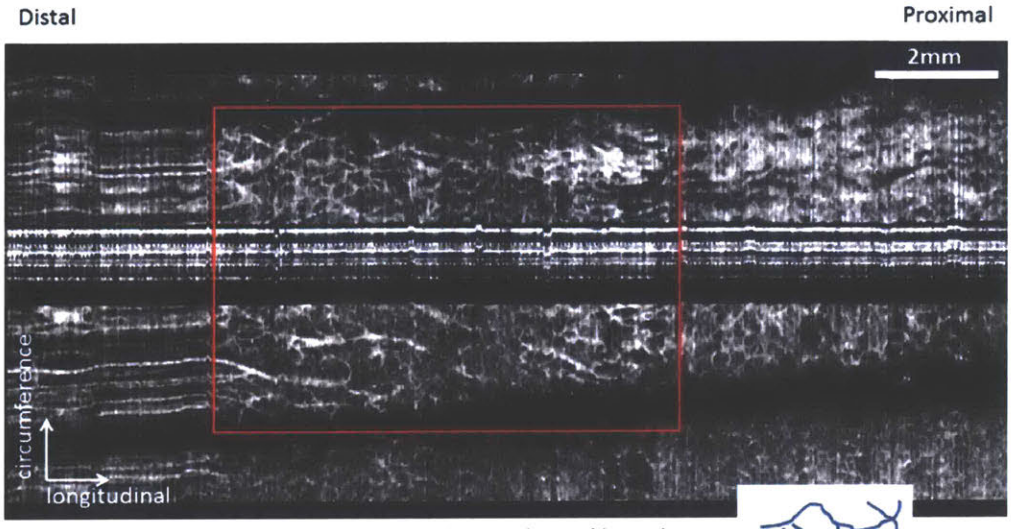

Distorted vascular pattern = abnormal vessel branching

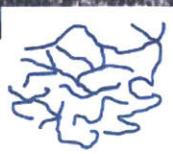

Image depth: 190 µm (OCTA_019.pgm)

47

HGD – 01 (summary)

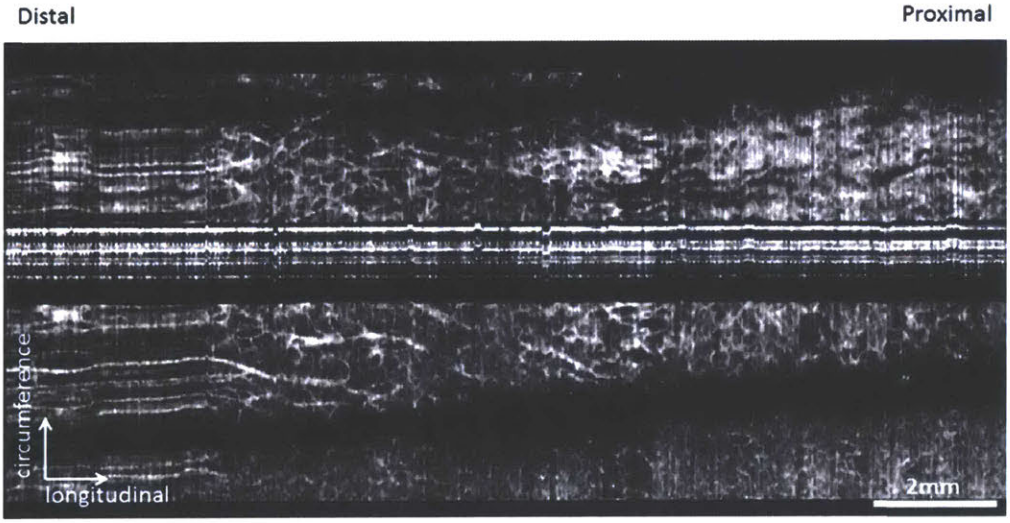

- **Distorted vascular pattern**: abnormal vessel branching (square box)

Image depth: 190µm (OCTA_019.pgm)

48

Reading instructions – I

- **Read *en face* OCTA images specifically in the superficial vasculature epithelium from Set XX_OCTA_001.pgm → Set XX_OCTA_ 030.pgm (i.e. image numbers 01-30). DO NOT read deep vasculature (i.e. image numbers 31-70) at this step, since this corresponds to the muscularis mucosa.**

- **Evaluate the presence of 2 possible different vascular features around the medium depth level of the superficial vasculature epithelium (Set XX_OCTA_011.pgm → Set XX_OCTA_020 (+/-2).pgm).**
  1. **Abnormal vessel branching (square, blank=0, 1)**
  2. **Heterogeneous vessel size (elliptical, blank=0, 1)**

- **If a features(s) is present, record the frame number (depth) exhibited most of distorted vascular features.**

- **Mark the outlines around the regions of these features with box of specific shape (feature 1: square; feature 2: elliptical)**

49

Reading instructions – II

- **For each OCTA dataset, mark the regions of each feature (if present) in the score sheet. Leave the score as blank if no feature is present.**

- **After reading all OCTA set, please review your reads through all the reading sets again to confirm your feature assessment. Mark the OCTA dataset where your confidence level in the assessment of features is low. (MIT staff)**

- **Please record the reading time for each set. (facilitated by the MIT staff)**

- **Summary of the work flow:**

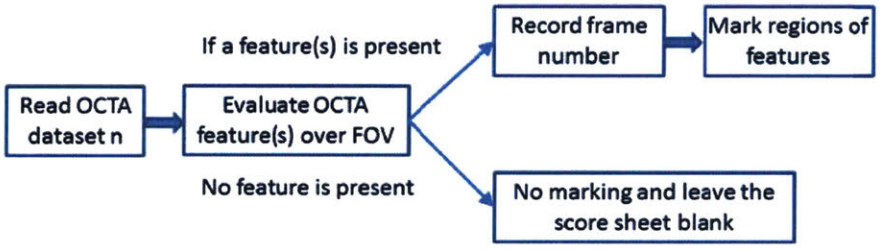

50

CHAPTER 5

5.0 Comprehensive Assessment of Radiofrequency Ablation Dynamics with Optical Coherence Tomography

5.1 Motivation

Compared to various existing modalities for treating esophageal neoplasm, RFA has been demonstrated as a safe and effective treatment for the eradication of dysplasia and early stage esophageal carcinoma in the patients with Barrett's esophagus (BE) [31, 51, 55]. The commercially available RFA devices (Barrx series, Medtronic (formerly BARRX Medical, CA), MN), comprising a thin layer of bipolar electrode arrays, can be generally divided into two categories based on the treatment area: (1) circumferential ablation catheters which consists of an inflatable balloon with a variety of balloon sizes to accommodate the varying diameter of the esophagus among individuals (18-31 mm in diameters), and (2) focal ablation catheters which can be mounted to the distal end of the endoscope and target specific lesions inside the esophagus under the guidance of the endoscopic view [180, 181].

To date, various clinical studies have demonstrated the efficacy and durability of RFA toward the complete eradication of dysplasia (CE-D) in patients with BE [58]. Among the patients who received RFA treatments for either non-dysplastic BE (intestinal metaplasia, IM) or any grade of the dysplasia, 78% and 91% of the patients achieved complete eradication of IM (CE-IM) and CE-D, respectively, based on a recent large scale, meta-analysis study [58]. In addition, CE-IM was achieved in 92% of patients at the five-year follow-up [56]. Furthermore, a low stricture rate (<6%) was reported among the patients treated with RFA compared to previous treatment methods [31, 59].

However, repetitive RFA sessions were required to achieve CE-IM or CE-D. On average, 3.4 and 3.5 sessions were required for patients with IM alone [60] or any grade of dysplasia to achieve CE-IM [31], respectively. Current practice requires multiple RFA applications, with abrasion and sloughing off the coagulum between sequential applications, to ensure sufficient RF energy is delivered over the BE epithelium [56]. These multi-step RFA procedures are recommended by the manufacturer because of the limited penetration of RF energy into superficially ablated tissue. In addition, a good tissue contact with the RFA catheter is essential to achieve optimal ablation depth. Lastly, the assessment of the effectiveness of each RFA application mainly relied on visual inspection, which might be challenging due to bleeding from the ablated sites. Recently, a high recurrence rate of IM has been reported in 13% [31] and

25.9% [61] of the patients received RFA treatment for dysplasia at 1 year after CE-IM was achieved, suggesting the current RFA practice might not be optimal. An endoscopic imaging modality can provide subsurface architectural information of the targeted site either before or immediately after the RFA application might be helpful for treatment planning and guidance.

Optical coherence tomography (OCT) can provide, cross-sectional or three-dimensional (3D) imaging of the tissue architectures in real time, and is well suited for the assessment of RFA application. In a previous study of 33 patients undergoing RFA treatment, our group reported a strong correlation between the presence of residual BE glands or BE epithelium in the post-RFA OCT images with inferior RFA efficacy [182]. More importantly, a threshold of BE epithelium thickness of 333 μm measured in the pre-RFA OCT images had a predictive value of 92.3% sensitivity and 85% specificity on the presence of BE in the follow up visit, suggesting the potential of using OCT to improve the efficacy in current RFA practice, and further develop an image-guided RFA procedure with OCT.

The concept of using OCT to guide the RFA procedure was first demonstrated to target the application of cardiac arrhythmia treatment. Real time monitoring of the changes of cardiac tissue architectures during the RFA application was reported using a forward imaging catheter on *ex vivo* [183] and *in vivo* [184] swine heart tissue, demonstrating the feasibility of image-guided RFA. In addition, due to the rich birefringent nature of the myocardium, studies have demonstrated polarization-sensitive OCT (PS-OCT) imaging with a fiber-optic forward imaging catheter for cardiac RFA monitoring [185]. A later study reported a novel RFA catheter enabling simultaneous RFA application and polarization-sensitive low coherence interferometry measurement on *ex vivo* swine heart tissue [186]. However, a comprehensive and systematic investigation using OCT to identify and monitor the changes of esophageal tissue architecture during the RFA application in real time has not been demonstrated yet.

In this study, we developed a high speed OCT system to identify or monitor the changes in the esophageal tissue architectures due to RFA application with the commercially available RFA catheters. Two different OCT imaging/RFA application protocols were performed using *ex vivo* swine esophagus specimens: (1) post-RFA volumetric OCT imaging to quantitatively measure

the thickness of the coagulum due to the RFA application with different energy settings (dosages), and (2) M-mode OCT imaging for real time monitoring of the dynamics of changes in tissue architectures during the RFA application. The quantitative analysis of the *ex vivo* esophagus tissue in response to the RFA applications in response to different energy settings was reported.

The FDML light source used in the high speed OCT system in this study was developed by Tsung-Han Tsai, and the high speed OCT engine was designed and built by Jonathan J. Liu and myself. Jonathan Liu and Tsung-Han Tsai participated the discussion of the study design and experiment plan of the study. The OCT imaging of the *ex vivo* swine esophagus was performed by Jonathan J. Liu and myself. All the data processing, specimen handling and preservation, and the statistical analysis were performed by the author of the thesis work.

5.2 Experimental Setup and Study Design

5.2.1 High speed swept-source OCT system

Figure 5.1 shows the schematic diagram of the high speed swept-source OCT system used in this study. The system employed a double-buffered Fourier domain mode-locked (FDML) laser with an output optical power of ~60 mW, a sweep range of ~140 nm and a bandwidth of ~90 nm full width at half-maximum (FWHM) centered at 1.3 μm wavelength. The configuration of the FDML light source was similar to the recently reported studies, enabling an effective Ascan rate of ~240 kHz with the double-buffered configuration [187, 188].

Light exiting from the FDML laser was split and coupled into a Mach-Zehnder interferometer (MZI) and an OCT interferometer. The interference fringes from the MZI were detected by a dual-balanced detector (PDB430C, Thorlabs, Inc., NJ) with a 350 MHz detection bandwidth and acquired once prior to the OCT imaging session to recalibrate the OCT interference signals. The OCT interferometer comprised of a 90/10 fiber-optic coupler, an optical isolator (AC Photonics, CA), a sample arm with a scanning confocal microscope [189], and a single-pass reference arm. In the confocal microscope, a pair of closely spaced galvanometer scanners with 5 mm mirrors (6215H, Cambridge Technology, Inc., MA) was used to provide

two-dimensional (2D) optical beam scanning over the specimen surface. Light exiting the fiber terminal was collimated onto the scanner using a near-infrared (IR) achromatic lens (f = 18 mm) and relayed to the objective afterward through a pair of identical near-IR achromatic doublets (f1 = f2 = 75 mm, AC254-075-C, Thorlabs, Inc., NJ). A long working distance, near-IR objective (WD = 37.5 mm, M Plan Apo NIR 5X, Mitutoyo, Japan) was used to provide sufficient space for the RFA catheter and other essential mounting tools.

Light returned from the sample arm and the reference arm was interfered in the 50/50 fiber-optic coupler (AC Photonics, CA) and detected using a dual-balanced detector with identical specifications to the MZI detector. Both the detected calibration (MZI) and OCT signals were digitized using a high speed A/D card (ATS9350, Alazar Tech, Canada) at a sampling speed of 500 MS/s. The measured sensitivity of the OCT system was 107 dB, and the 6 dB sensitivity roll-off imaging depth was ~2.5 mm (in air). The high speed OCT system enabled imaging with an axial resolution of 7.4 μm (in tissue, assuming a tissue refractive index of 1.38 at 1310 nm wavelength regime) and a transverse resolution of 12.1 μm (FWHM, in tissue) characterized using the knife edge method, which is close to the theoretical value of 11.9 μm (FWHM). The relatively high transverse resolution resulted in a small confocal parameter of ~253.3 μm.

5.2.2 Radiofrequency ablation (RFA) setup

A commercial RFA instrument with focal RFA catheters (Barrx 90, Medtronic, MN) was used in this study. The energy generator (Barrx Flex, Model 90-9000, Medtronic, MN) allowed a variation of the RF energy settings between 12 – 15J/cm^2 (power density: 40 W/cm^2; frequency: 460 kHz; duration: ~0.3 seconds) for the Barrx 90 catheter. The ablation paddle (electrode dimension) located on the distal end of the Barrx 90 catheter was 13 x 20 mm^2, which was covered by an electrode array of 24 electrodes. Each electrode was 250 μm in width with a separation of 250 μm from each other. To decrease the attenuation of the light transmitted through the ablation paddle, a small region (~4 x 4 mm^2) on the back side of the ablation paddle was machined to partially remove the overlying supporting plastic material without affecting the mechanical integrity and electrical connection of the catheter. As shown in the lower right inset in Fig. 5.1, a small depressed region (red arrow) can be observed on the back of the ablation paddle allowing simultaneous OCT imaging during the RFA application.

5.2.3 Specimen handling, imaging, and RFA protocol

Fresh swine esophagus was excised and stored in the Dulbecco's Modified Eagle's Media (DMEM, Cellgro, Corning, VA) at 4 degrees Celsius. Before the RFA application, the swine esophagus was cut into pieces with an adequate size (~ 2 x 3 cm^2) to ensure sufficient contact between the focal RFA catheter and the specimen. In this study, two OCT imaging protocols with different RFA settings were performed to systematically investigate the characteristics of the coagulum formation due to RFA application. In addition, as reported in an *ex vivo* study of the human colon tissues, the epithelium thickness measured in the OCT images decreased with the increasing pressure exerted by the imaging catheter.[190] Therefore, during the OCT imaging, an identical pressure was applied on the different specimens in individual protocols to reduce the variability in the thickness measurements. In practice, the force exerted by the endoscope through the distally mounted focal ablation catheter was measured to be ~100 grams over a surface area the same as the ablation paddle size (~1.3 x 2 cm^2) during the RFA application.

(1) Post-RFA volumetric OCT imaging: This protocol investigated the feasibility of using OCT for quantitatively assessing the coagulum due to the RFA applications with different energy settings. In this protocol, RFA (single application only) was applied on individual specimens with the energy settings of 12, 13, 14, or 15 J/cm^2 as designated where the range of energy settings was limited by the commercial RFA instrument. Then, a thin cover glass (2.4 x 3 cm^2) was gently pressed over the ablated specimen to create a flat imaging plane and maintain a constant pressure (~220 grams/6 cm^2), consistent with the value exerted by the RFA paddle over the tissue surface in practice (100 grams/2.6 cm^2). By adjusting the distance of the cover glass with respect to the specimen, the pressure (i.e. pressing force) can be measured through the weight scale below the specimen (top right inset, Fig 5.1). In this study, although the imaging field was relatively limited, the use of a 5X objective allowed high resolution imaging of the swine esophagus specimen *ex vivo*, which promised to facilitate the visualization of the coagulum formation due to the RFA applications. In addition, the coagulum was not uniform across the entire ablated area (~ 2 x 3 cm^2). Therefore, post-RFA volumetric OCT imaging was

performed on a surface area of 3 x 3 mm^2 with 1000 x 1000 Ascans over the ablated region with the most prominent coagulum formation.

(2) M-mode OCT imaging: This protocol investigated the feasibility of using OCT for real time monitoring of the changes in tissue architecture during the RFA application. In this protocol, a modified focal RFA catheter was placed over the *ex vivo* swine esophagus specimen with a controlled pressure (100 grams/2.6 cm^2), following the similar procedure as described in the protocol (1). Repetitive B-scan OCT images of the *ex vivo* swine esophagus specimen (M-mode OCT imaging through the electrode spacing of the RFA catheter) was acquired during the RFA application (lower right inset, Fig. 5.1). In addition, rather than single application, two consecutive RFA applications with the energy settings of either 12 J/cm^2 or 15 J/cm^2 were applied to individual specimens where M-mode OCT imaging was performed during both applications. Furthermore, the coagulum resulted from the 1st RFA application was not removed before the 2nd RFA application, which allows us to investigate the ablation efficacy of the 2nd RFA application under the presence of existing coagulum.

5.2.4 Histology processing and coagulated tissue analysis

Following the RFA application and OCT imaging, the specimens were ink marked to indicate the OCT imaged area. Then, the specimens were placed inside standard tissue cassettes and fixed in 10% formalin prior to histology processing. Standard hematoxylin and eosin (H&E) staining protocol was used to assess the coagulum resulted from the RFA application [180, 181]. Digital pathology images were captured from the H&E histology slides using a slide scanner (Aperio AT2, Leica Biosystems, IL) with 20X magnification. Both the OCT images and the representative H&E histology images were analyzed to identify the characteristics of the coagulum including the coagulum thickness measurement.

The post-RFA OCT images were examined to manually segment the coagulum, residual epithelium (EP), and the underlying lamina propria (LP) layer based on the difference in the scattering properties. The thickness of the coagulum and the coagulum + residual EP layer was calculated accordingly in individual cross-sectional OCT images. A 2D thickness map was generated afterward if volumetric post-RFA OCT imaging was performed. To ensure sufficient

sampling, ~4-5 histology sections with a step interval of 200 μm were collected from the region including the OCT imaged site for each specimen sent for histology processing. For the histology image analysis, the thickness of the coagulum and residual EP layer was manually marked and measured using the digital pathology viewer (Aperio ImageScope v.11, Leica Biosystems, IL).

5.3 Results

5.3.1 RFA coagulum thickness analysis

Figure 5.2 shows the cross-sectional OCT images and representative H&E histology image from a swine esophagus specimen receiving a single RFA application with the energy setting of 14 J/cm^2 as an example to describe the coagulum thickness measurement/analysis performed in this study. Volumetric OCT images were acquired after the RFA application. As shown in Fig. 5.2(a), a three-layer tissue architecture—a homogenous hyperscattering layer near tissue surface corresponding to the coagulum (Co), a thin hyposcattering layer corresponding to the residual EP layer, and a hyperscattering layer corresponding to the LP layer—was identified and manually segmented afterward (Fig. 5.2(b)). This three-layer tissue architecture was consistent with the observations in the representative histology image (Fig. 5.2(c)). In the zoomed in histology image (Fig. 5.2(d)), the coagulum was characterized as layers of squamous cells with void intracellular space, which might have resulted in the hyperscattering characteristic of the coagulum identified in the OCT images. 2D thickness maps of the coagulum and the coagulum + residual EP (Figs. 5.2(e, f)) were generated from the manually segmented volumetric OCT datasets. The varying thickness of the coagulum and coagulum + residual EP layer can be observed across the imaging field. The comparison of the thickness of the coagulum and the coagulum + residual EP layer measured between the OCT the histology measurements will be discussed and summarized in the subsequent section.

5.3.2 Volumetric OCT imaging of the RFA coagulum at different energy settings

In this aspect of the study, we aimed to investigate the feasibility of using OCT to identify and measure the changes of coagulum thickness in response to RFA applications with different energy settings. A collection of *ex vivo* swine esophagus specimens were treated with RFA applications and imaged with volumetric OCT afterward following the protocol described in

section 2.3. The number of specimens treated with individual energy settings was: 12 J/cm^2 (N = 4), 13 J/cm^2 (N = 3), 14 J/cm^2 (N = 2), and 15 J/cm^2 (N = 4). Figure 5.3 shows the (a, b) cross-sectional OCT images, as well as thickness map of the (c, d) coagulum and (e, f) coagulum + residual EP from two RFA treated specimens with the energy settings of 12 J/cm^2 and 15 J/cm^2, respectively. Similar to Fig. 5.2(a), a three-layer tissue architecture can be observed in Fig. 5.3(a) with the energy setting of 12 J/cm^2. The fraction of the residual EP layer decreased on the specimen treated with a higher energy setting (15 J/cm^2), as shown in Fig. 5.3(b). The difference of the coagulum thickness in response to RFA applications with different energy settings can also be observed in the 2D coagulum thickness maps (Figs. 5.3(c, d)). Figs. 5.3(e, f) show the histology images acquired from the locations close to the cross-sectional OCT images (Figs. 5.3(a, b)) where the boundary between the coagulum and the residual EP layer in Fig. 5.3(e) was less clearly discernible compared to that with a higher energy setting (15J/cm^2) as shown in Fig. 5.3(f).

A quantitative analysis of the average coagulum thickness with respect to different RFA energy settings was performed subsequently. The average coagulum thickness in individual specimens was calculated based on the segmented coagulum layer in the post-RFA volumetric OCT dataset. A gradual increase in the coagulum thickness was identified in response to the increasing energy settings (Fig. 5.4). In addition, a significant difference ($p < 0.01$, student t-test) in the coagulum thickness was observed in the specimens treated with the energy settings of 15 J/cm^2 vs. 12 J/cm^2. We also compared the thickness of the coagulum and coagulum + residual EP layer measured in the OCT images with the representative H&E histology images using a subset of the RFA treated specimens (12 J/cm^2: N = 2; 15 J/cm^2: N = 2) including the two specimens showed in Fig. 5.3. The comparison results were summarized in Table 5.1. An increase in the average coagulum thickness was identified in the OCT measurements of the specimens treated with a higher energy setting. In addition, a variation of the thickness of the coagulum + residual EP layer, reminiscent the thickness of the EP layer prior to the RFA application, was observed in the OCT measurements. This thickness variation was because the specimens were collected from different swine esophagus and different longitudinal locations of individual esophagus afterward. As for the histology image analysis, one of the specimens treated with a higher energy setting (specimen C) showed comparable or thinner coagulum

thickness measurement like the ones with a lower energy setting (Specimens A and B). This disagreement might be related to the specimen handling and fixation, and histology processing steps. For example, the specimen might be shrunk during tissue fixation, which makes the comparison of the absolute thickness measurement between the OCT and histology images difficult. Therefore, the scale factor between the OCT and the histology measurement of the coagulum and the coagulum + residual EP layer thickness was used. As shown in Table 5.1, the scale factor (OCT/H&E) is similar for the coagulum and coagulum + residual EP among all four specimens listed, suggesting the shrinkage was comparable for different tissue types, e.g. the coagulum vs. residual EP layer. The incidence of a thicker coagulum observed in the histology image might be related to the tissue handling and the fixation aforementioned as well as the orientation of the histology section with respect to the OCT imaging planes.

5.3.3 Concurrent OCT imaging of the RFA process

Another important aspect of the study was to demonstrate the capability of using OCT for real time monitoring of the changes in tissue architectures during the RFA application. Commercially available focal RFA catheters were slightly modified as described in section 5.2.3 to enable concurrent OCT imaging during the RFA application. Two consecutive RFA applications were applied to individual specimens with the energy settings of 12 J/cm^2 (N = 5) or 15 J/cm^2 (N = 6).

Figure 5.5 shows the dynamics of architectural changes in the specimen during the (a-f) 1st and (g-l) 2nd RFA application with the 12 J/cm^2 energy setting. During the 1st RFA application at time T = 0.00 s, regular esophageal structures (EP, LP, and part of the muscularis mucosa (MM)) could be observed beneath the RFA ablation electrodes (AE). At time T = 0.1 - 0.25 s, hyperscattering regions were observed due to the thermal energy delivery. Also, the vaporization of water either over or within the specimen due to the thermal energy delivery, resulted in the variation in the locations of the ablation electrodes (AE) and the underlying specimen (diamond arrows, Fig. 5.5(d)) as noticed in the M-mode OCT images. The blurring of the tissue speckle pattern was also related to the tissue motion induced by the water vaporization (Figs. 5.5(c-e)). Starting at time T = 0.30 s (Fig. 5.5(f)), the boundary of the hyperscattering layer became constant (arrows) and can be delineated clearly, which allowed a coagulum thickness measurement similar to section 5.3.2. A thin hyposcattering layer representing the residual EP

layer can be observed as well (Fig. 5.5(f)). Without removing the coagulum, the 2nd RFA application was applied subsequently (Figs. 5.5(g-l)). At time T = 0.10 - 0.25 s, the slight loss of catheter-tissue contact and blurring of tissue speckle pattern similar to the findings during the 1st RFA application were observed (Figs. 5.5(i-k)). In addition, the depth of the hyperscattering layer further increased and became more uniformly distributed after the 2nd RFA application. However, the coagulum due to the 1st RFA application decreased the efficiency of the thermal energy delivery from the ablation catheter to the residual EP layer. After the 2nd RFA application, the boundary of the hyposcattering layer (the coagulum) was nearly overlapped with the initial EP/LP boundary in 2/3 of the imaging field suggesting the EP layer should have already been fully ablated over these regions. However, no significant architectural changes in the superficial LP layer can be identified in the OCT image after the 2nd RFA application.

Figure 5.6 shows the representative H&E histology image (a) near the OCT imaged site of Fig. 5.5 and (b) from a location ~5 mm away from (a) but still within the ablated regions. Similar to the observation in Fig. 5.2(b), the coagulum was characterized by layers of squamous cells with void intracellular space. In addition, in particular, the superficial LP layer near the OCT imaged site exhibited a different architectural appearance (arrows, Fig. 5.6(a)) compared to that away from the OCT imaged site (arrows, Fig. 5.6(b)), which can also be identified by comparing the tissue architectures of the superficial (arrows) and the deep LP layer (stars) in Fig. 5.6(a). Both observations confirmed that the ablation was extended from the EP into superficial LP layer over the OCT imaged site where the boundary of the coagulum was nearly overlapped with the initial EP/LP boundary in the 2/3 of the OCT imaging field. In addition, although both histology images were acquired within the regions treated with two consecutive RFA applications, the difference in the appearance of the superficial LP layer suggested the thermal energy delivery was not uniform across the ablated regions. Noted that the coagulum thickness observed in Fig. 5.6(a) was thinner compared to the coagulum + residual EP in Fig. 5.6(b), which might be due to the sloughing of the coagulum during either the removal of the ablation catheter or the fixation process.

Figure 5.7 shows the dynamics of changes in the tissue architectures from an *ex vivo* swine esophagus specimen treated with two consecutive RFA applications using the energy setting of

15 J/cm^2. The architectural changes observed during the (a-f) 1st and (g-l) 2nd RFA application were similar to those identified in Fig. 5.5 in general. However, due to a higher energy setting, the hyperscattering layer corresponding to the coagulum was thicker after the 1st RFA application. In some regions (red arrow, Fig. 5.7(f)), the boundary of the coagulum was already nearly overlapped with the initial EP/LP boundary, suggesting a complete EP ablation over these regions as described in Figs 5.5 and 5.6. After the 2nd RFA application (Figs. 5.6(g-l)), the boundary of the hyperscattering layer was overlapped with the initial EP/LP boundary in nearly the entire OCT image. In addition, no significant architectural changes within the LP layer with respect to RFA application can be identified in the OCT image even though a higher energy setting was used, which limits the capability to measure the increase in coagulum thickness from the 2nd RFA application with OCT.

Table 5.2 summarized the coagulum thickness measured in the single M-mode OCT image of individual specimens after the 1st RFA application. Similar to the findings reported in Fig. 5.4, the specimens treated with higher energy RFA applications (15 J/cm^2) showed thicker coagulum than those treated with a lower energy setting (12 J/cm^2). In addition, although the coagulum thickness after the 1st RFA application seems to be higher than those reported in the previous section (Fig. 5.4 and Table 5.1), noted that only single OCT image rather than volumetric OCT dataset over a surface area of 3 x 3mm^2 was used in the analysis. Lastly, as mentioned in Figs 5.5 and 5.7, no changes in the tissue scattering properties within the LP layer with respect to the RFA application was identified in the OCT images. Therefore, it was difficult to assess the increase in the coagulum thickness due to the 2nd RFA application alone with OCT.

5.4 Discussion

Although RFA has demonstrated a high eradication rate of dysplasia in BE, multiple studies have reported the recurrence of BE and progression to esophageal adenocarcinoma (EAC) afterward in the post treatment period [191-194]. In addition, due to the limited ablation depth, multiple RFA applications and cycles of sloughing off the coagulum between successive applications are required in individual RFA sessions, which increase the complexity and labors of current RFA procedures. Unfortunately, the maximum ablation depth in the RFA procedure is governed by the narrow spacing between the electrodes [180, 181] and the energy settings where the

adjustment range is limited in the current instrument for safety reasons. Our recent study of 33 patients reported that a BE epithelium thickness of $\geq$ 333 μm measured in the pre-RFA OCT images had a 92.3% sensitivity and 85% specificity in predicting the presence of endoscopically visible BE at the following visit after the RFA treatments [182]. This result suggested the existing RFA procedure might be suboptimal, and the RFA energy settings might not be sufficient to accommodate the variation of BE thickness among individuals. However, there is no image guidance in existing RFA procedures to assess *in situ* RFA efficacy over the treated region except visual inspection with WLE, which is limited to imaging tissue surface but not the underlying tissue architectures. In addition, the bleeding from the treated region after individual RFA applications obscures the visual examination with WLE.

In this study, we demonstrated the feasibility of using OCT to quantitatively measure the coagulum thickness after the RFA application with respect to different energy settings using an *ex vivo* swine esophagus model. In protocol (1), post-RFA volumetric OCT images were acquired over the regions exhibiting the most prominent coagulum formation under the guidance of the OCT preview, which was nearly equivalent to measure the maximum coagulum thickness over the ablated region of individual specimens. A 2D coagulum thickness map was generated from the manually segmented volumetric OCT images afterward, enabling a more robust measurement of the coagulum thickness of the individual specimens compared to single OCT image. We observed an increase in the coagulum thickness after the RFA application with increasing energy settings, ultimately limited by the approved energy settings in the commercially available RFA instrument. The results of the protocol (1) demonstrated the feasibility of controlling the coagulum thickness (i.e. the ablation depth) by adjusting the energy setting of the RFA application.

In protocol (2), we showed the capability of using OCT to identify the changes in tissue architectures during the RFA application in real time with respect to different energy settings, which might enable future use of OCT for real time planning and guidance of the RFA application. In addition, the concurrent OCT imaging and RFA application platform developed in this study allows *in situ* measurement/assessment of the coagulum and the residual EP after the RFA application with respect to different RF energy settings. Table 5.2 summarized *in situ*

coagulum thickness measurement after the 1st RFA application using the energy settings of 12 J/cm^2 and 15 J/cm^2. Note the analysis was performed using a single cross-sectional OCT image from each individual specimen where the imaged site might not correspond to the region exhibiting the most prominent coagulum formation. Nevertheless, similar findings as those reported with post-RFA volumetric OCT images were observed. The results of protocols (1) and (2) suggest the potential to achieve a controlled full-epithelium ablation by adjusting the energy setting and the feasibility of using OCT to monitor the changes of tissue architectures during the RFA application or confirming the RFA efficacy in the post-RFA settings.

Due to the unique advantages of OCT and existing issues of RFA procedure aforementioned, an OCT-integrated RFA device might promise to simplify the RFA procedure and improve the efficacy of RFA. Recently, our group has developed an ultrahigh speed endoscopic OCT system and a micromotor balloon catheter, enabling circumferential imaging coverage of the esophagus using an *in vivo* swine esophagus model over a surface area of 13 cm^2 in <18 seconds [140]. This balloon-based endoscopic OCT platform can be potentially integrated with existing circumference ablation catheters (Barrx 360, Medtronic, MN). Unlike focal ablation catheters, the thickness of the supporting materials beneath the active electrodes is thin enough to ensure OCT imaging with sufficient contrast. The OCT-integrated RFA device allowing treatment planning and real-time monitoring can produce a controlled ablation depth and area, which could ultimately improve the existing RFA procedures.

There were several limitations in this study. First, as a preliminary feasibility study, although the 5X objective allowed high resolution OCT imaging of different architectural features within the swine esophagus due to the RFA application, both the imaging field and the confocal parameter were relatively limited. Due to the varying tissue contact between the targeted region and the RFA catheter, the thermal energy delivery (i.e. the coagulum formation) might not be uniform over the entire ablated region. Therefore, given the limited imaging field and the nonuniform coagulum formation, in the protocol (1), post-RFA volumetric OCT imaging was performed over the regions exhibiting most prominent coagulum formation other than the entire ablated region, which allows the assessment of the coagulum uniformity including the maximum and minimum coagulum thickness over the ablated region. The limited imaging field and the

short confocal parameter can be improved by replacing the 5X objective with a low numerical aperture, achromatic scan lens.

In addition, as shown in Table 5.1, there existed disagreement on the thickness of the coagulum and coagulum + residual EP layer between the OCT and the histology measurement. Although the scale factor between the OCT and histology measurement was similar for the coagulum and coagulum + residual EP layer, it varied among different specimens because the specimen was not handled and fixed in the same configuration as it was imaged. For example, a controlled pressure was applied to the specimen during the OCT imaging session. However, the specimen might be pressed with a different pressure or no pressure at all while being stored inside the tissue cassettes and fixed in the formalin solution depending on the thickness of specimen relative to the cassette height. Even though the surface area of the individual specimen was trimmed first according to the size of the ablation paddle aforementioned, the specimen thickness was hard to adjust. Therefore, for specimen thinner than the cassette height, the specimen can be shrunk along any axes and resulted in a large variation in the specimen size post fixation (i.e. a large scale factor (OCT/H&E)). Mechanical mounting of the specimen prior to the fixation process or the use of frozen section analysis as reported in the previous studies [195, 196] might mitigate the variation of the specimen size during the tissue preservation process. Hence, it might promise to facilitate correlating the coagulum thickness measurement in the OCT images with the representative histology images as a function of different energy settings. Nevertheless, the coagulum might be sloughed off during the tissue preservation process, and affect the correlation afterward as observed in Fig. 5.6(a).

Third, identifying the architectural changes within the LP layer due to the RFA applications was difficult using structural OCT signal alone (Figs 5.5 and 5.7). LP is a thin layer mixed with connective tissue and the glandular tissues/microvascular network in between. Due to the presence of collagen, which exhibits strong birefringence in the connective tissue, the contrast of the LP layer was enhanced in the PS-OCT images [146, 197, 198]. Therefore, it is possible to differentiate the ablated and non-ablated LP layer using PS-OCT based on the loss of birefringence from thermally-induced collagen denaturation [199]. Furthermore, similar to previous studies [180, 181, 200], a histology processing protocol with H&E staining was used to

assess the tissue architectural changes in response to the RFA application. Although H&E staining allows the identification of immediate physical tissue damage from the protein coagulation, it might not reflect the status of the cell viability in response to the injury from the RFA application, i.e. the apoptosis/necrosis afterward which are of biological importance, in particular, the *in vivo* animal model. Thus, future studies incorporating the cell viability stain such as nitroblue tetrazolum chloride (NBTC) histology [195, 196] should be considered to perform in parallel with the conventional H&E staining. Lastly, an *ex vivo* normal swine esophagus model was used in this study to investigate the ablation depth due to the RFA application with OCT. However, it should be noted that the tissue ablation depth in the squamous mucosa in *ex vivo* swine esophagus might differ from *in vivo* swine esophagus or human BE mucosa. As reported in the application of RFA for the treatment of liver tumors, the thermal lesion size decreases as the lesion blood perfusion rate increases [201], suggesting the significance of the blood flow on the RFA efficacy, which is absent in the *ex vivo* swine esophagus model. Therefore, it is important to perform *in vivo* studies in the future to confirm these findings as the physiological factors will likely affect the RFA dynamics.

5.5 Figures

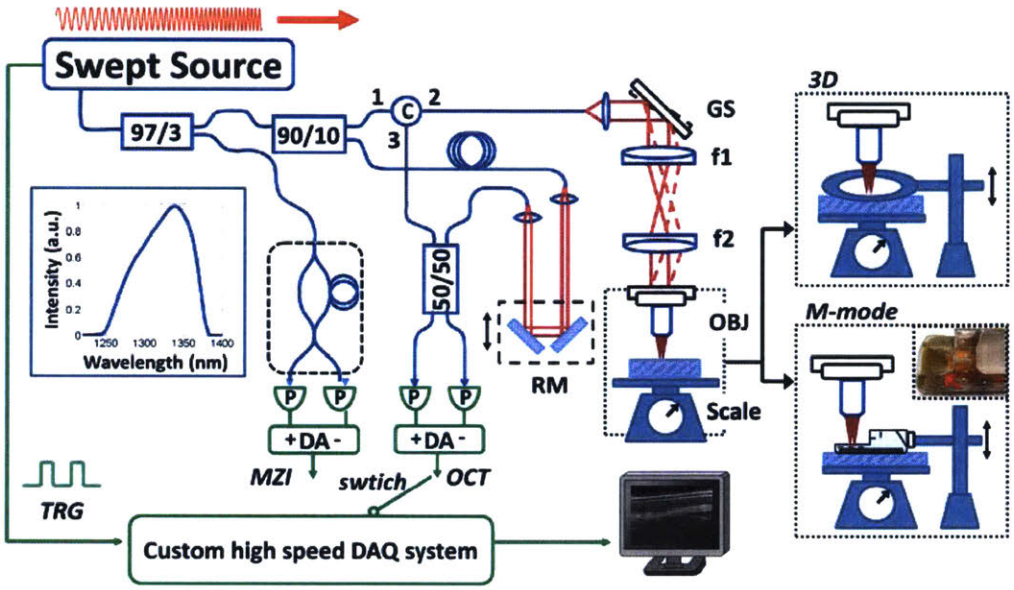

Figure 5.1. Schematic diagram of the high speed swept-source OCT system (blue: optics; green: electronics). Inset (left): optical spectrum of the wavelength swept light source showing a Gaussian spectral shape. Inset (top right): imaging setup showing volumetric (3D) OCT imaging over the specimen where a cover glass was pressed over the specimen with a controlled pressure measured by the scale below. Inset (lower right): imaging setup of M-mode OCT imaging where the optical beam was scanned through the ablation device. MZI: Mach-Zehnder interferometer; TRG: trigger signal; DA: differential amplifier; RM: reference mirror; GS: galvanometer scanner; C: circulator; OBJ: objective; f1, f2: scan lens and tube lens of the relay optics. DAQ: data acquisition.

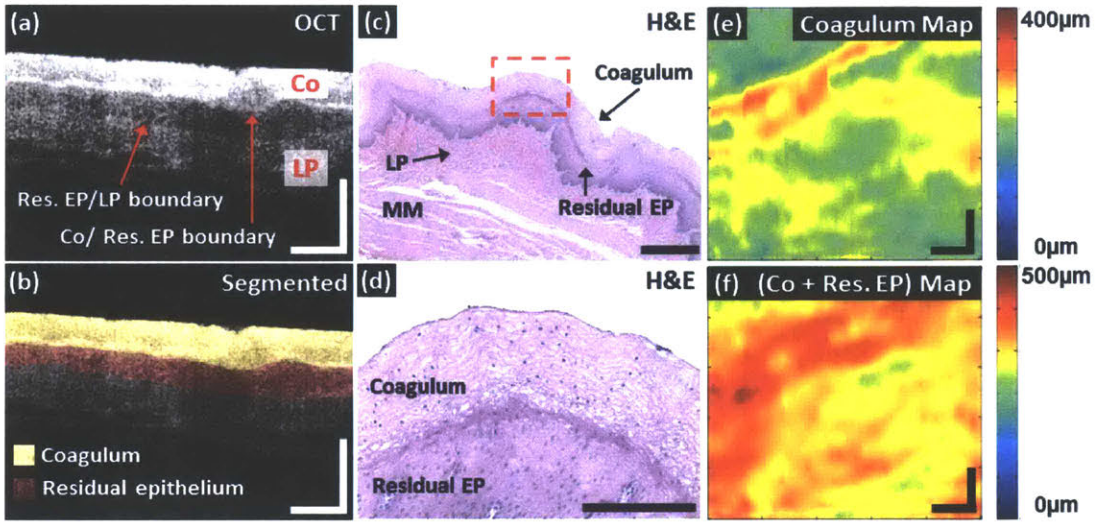

Figure 5.2. Coagulated tissue analysis. (a, b) Cross-sectional OCT images and (c, d) the representative histology images from an RFA treated *ex vivo* swine esophagus specimen showed the tissue architectures of the coagulum (Co), the residual epithelium (Res. EP), and the underlying lamina propria (LP) layer. (d) The zoomed-in histology image over the region of interest (red dashed box) marked in (c) showed the architectural characteristic of the coagulum. The coagulum and residual EP layer observed in the OCT images were manually segmented to generate two-dimensional thickness maps of the (e) coagulum and (f) coagulum + residual EP layer, respectively. Scale bars: (a-c, e, f): 500 μm; (d): 200 μm.

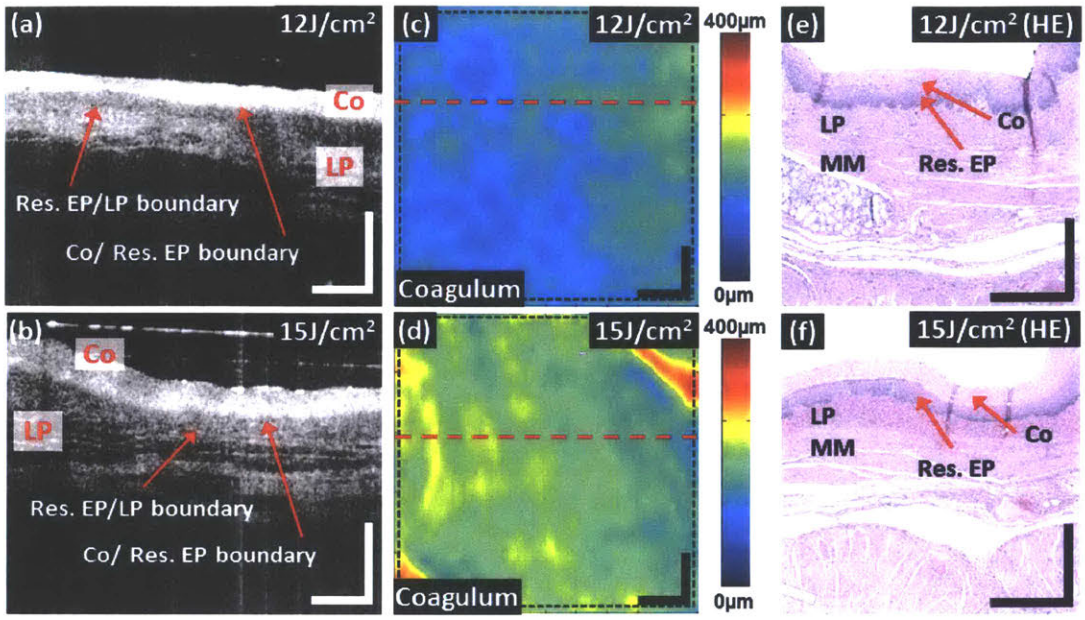

Figure 5.3. Coagulum thickness analysis from the RFA treated specimens with different RF energy settings (12 J/cm^2 and 15 J/cm^2). (a, b) Cross-sectional OCT images corresponding to the indicated location in the (c, d) coagulum thickness map from the specimens with the RFA applications of the energy settings of 12 J/cm^2 and 15 J/cm^2, respectively. (e, f) H&E stained histology images close to the locations of the (a, b) cross-sectional OCT images, respectively. Scale bars: (a-f): 500 μm. Res. EP: residual epithelium; Co: coagulum; LP: lamina propria; MM: muscularis mucosa.

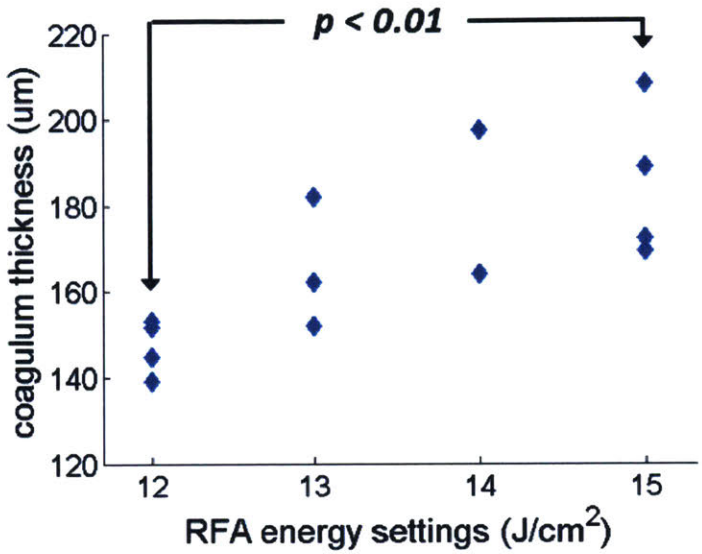

Fig. 5.4. Quantitative analysis of the coagulum thickness measured in the OCT images after the RFA application with different energy settings.

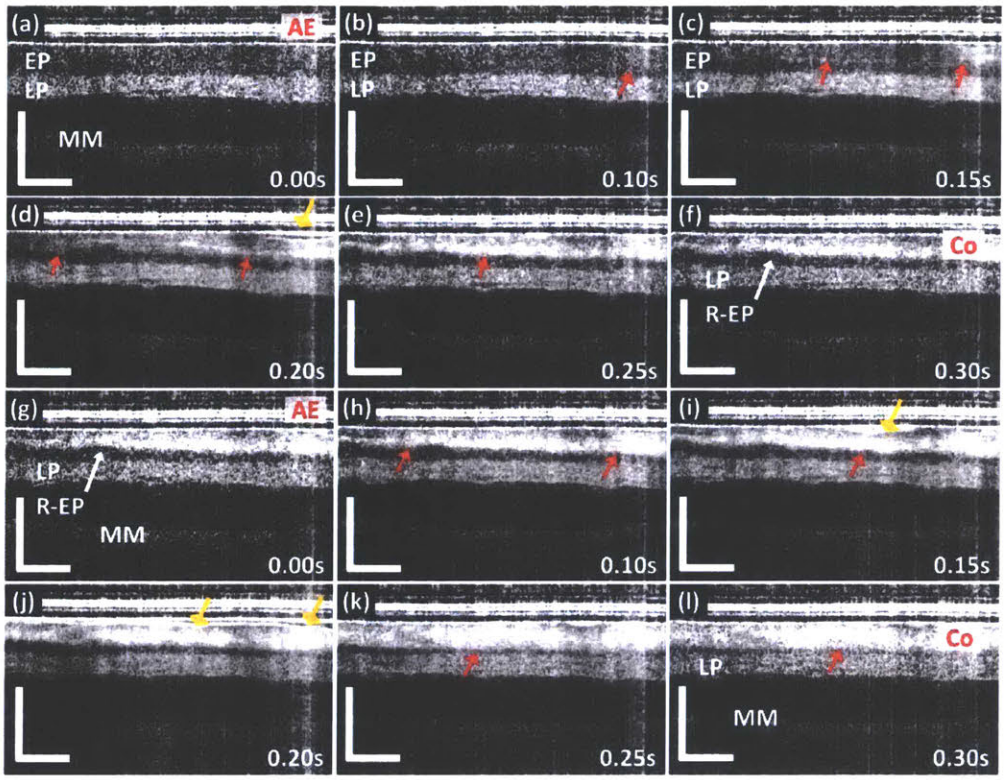

Figure 5.5. Dynamics of RFA process with the energy density setting of 12 J/cm^2 during the 1st and subsequent 2nd RFA application. (a) The distinctive layered structure of swine esophagus, including the epithelium (EP), lamina propria (LP), muscularis mucosa (MM), and the ablation electrode (AE) of the RFA catheter can be observed clearly at time T = 0 s. (b-e) Changes in the tissue architectures due to the RFA application including the emergence of a hyperscattering layer (red arrows), variations of the specimen location and tissue contact (diamond arrows) were observed starting at time T = 0.05 s to 0.3 s. (f) At time T = 0.3 s, the changes in tissue architectures stopped, and residual non-ablated EP layer (R-EP) can be observed. (g-k) During the 2nd RFA application, the tissue architectural changes were similar to the observations in (a-e). (l) At time T = 0.3 s, the tissue architectural changes stopped, and the boundary of the hyperscattering layer was overlapped with the initial EP/LP boundary in most of the regions (red arrow). s: second. Scale bars: 500 μm.

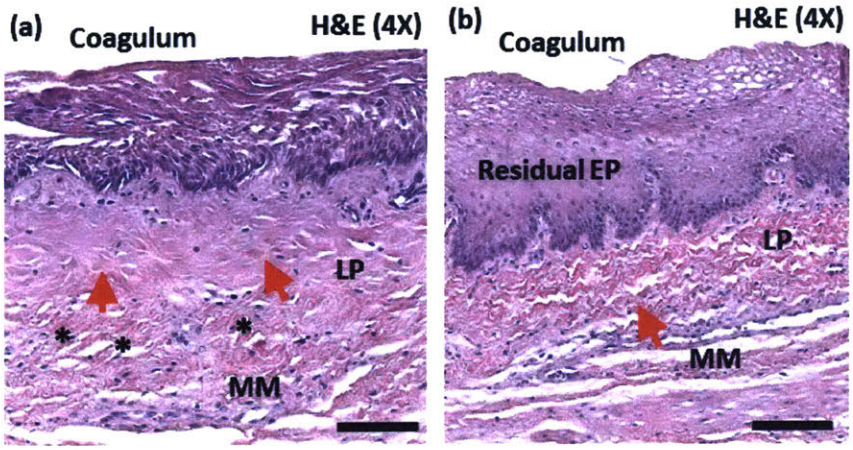

Figure 5.6. Representative H&E stained histology images (a) near the imaged site as Figure 5.4 and (b) from a location ~5 mm away from (a). (a, b) Layers of squamous cells with a void intracellular space corresponding to the coagulum from the RFA application can be identified. Alternation of the architectural appearance in the superficial LP layer (red arrows) was observed in (a) compared to the deep LP layer (stars, a) and (b) the LP layer from a different location suggesting the thermal energy delivery was fully extended into the LP layer in (a). Scale bars: 200 μm.

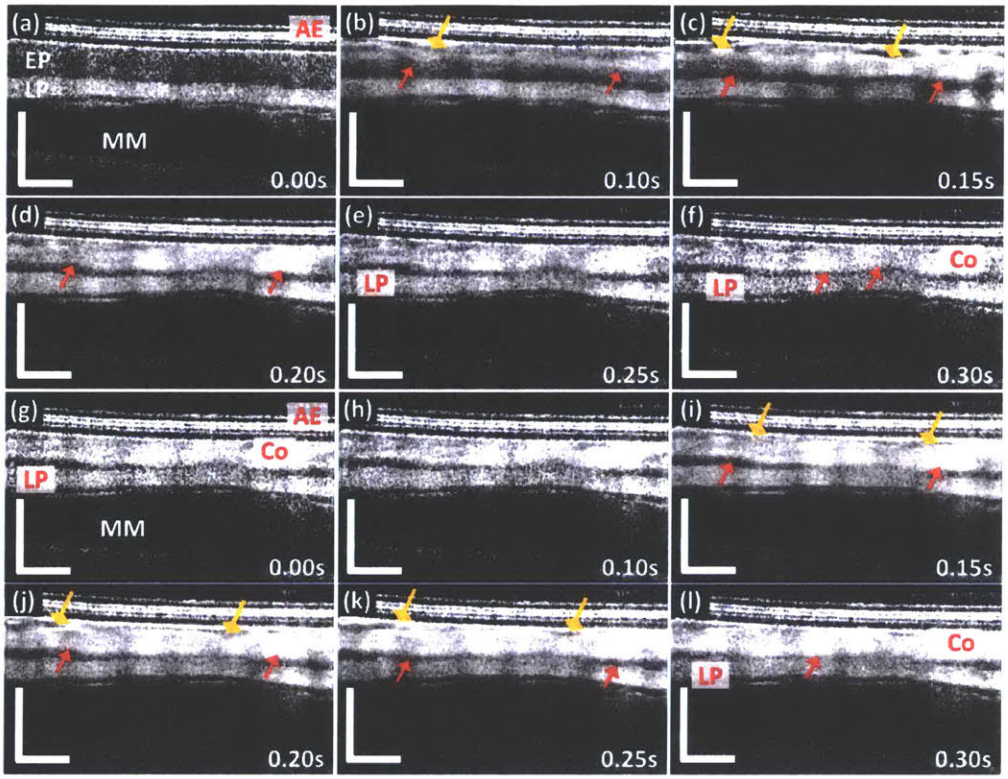

Figure 5.7. Dynamics of RFA process with the energy density setting of 15 J/cm^2 during the 1st and subsequent 2nd RFA application. (a) The distinctive layered structure of swine esophagus, including the epithelium (EP), lamina propria (LP), muscularis mucosa (MM), and the ablation electrode (AE) of the RFA catheter can be clearly differentiated. (b-e) Changes in the tissue architectures due to the RFA application including the emergence of a hyperscattering layer (red arrows), a variation of the specimen location and tissue contact (diamond arrows) were observed starting at time T = 0.05 s to 0.3 s. (f) At time T = 0.3 s, the changes in tissue architectures stopped, and only a limited fraction of residual non-ablated EP (R-EP) can be observed, due to higher RF energy. (g-k) The architectural changes during the 2nd application were similar to (a-e). (l) At time T = 0.3 s, the tissue architectural changes stopped, and the boundary of the hyperscattering layer was overlapped with the initial EP/LP boundary in the majority of the regions (red arrow). s: second. Scale bars: 500 μm.

5.6 Tables

Table 5.1. Comparison of the coagulum and coagulum + residual epithelium thickness measurements between the OCT and H&E histology images

	Coagulum			Coagulum + residual epithelium		
	OCT (μm)	H&E (μm)	OCT/HE	OCT (μm)	H&E (μm)	OCT/HE
Specimen A (12 J/cm^2)	140.3	117.7	1.19	220.8	176.7	1.25
Specimen B (12 J/cm^2)	147.8	144.1	1.03	251	264.4	0.95
Specimen C (15 J/cm^2)	207.3	117.5	1.76	362.3	219.1	1.65
Specimen D (15 J/cm^2)	184.7	177.8	1.04	202.9	206.7	0.98

Table 5.2. Quantitative comparison of the coagulum thickness between two different energy settings measured in the M-mode OCT images after the 1st RFA application.

	12 J/cm^2 (N=5)	15 J/cm^2 (N=6)	*p*-value
Max. coagulum thickness (μm), mean	195.2	229.4	0.012
Ave. coagulum thickness (μm), mean	168.3	201.5	0.015
Max. coagulum thickness (μm), mean	122.6	167.8	0.012

CHAPTER 6

6.0 Conclusion and Future Work

6.1 Summary of Thesis Work

This thesis work involved a combination of the development of next generation OCT imaging catheters, pre-clinical feasibility study of OCT imaging in animal models, and collaborative clinical studies on OCT imaging in patients. In collaboration with Praevium Research / Thorlabs Inc., an ultrahigh speed swept source OCT system was developed with a MEMS tunable vertical cavity surface-emitting laser (VCSEL) in a team effort lead by a previous Ph.D. student, Tsung-Han Tsai. In combination with the development of prototype small size micromotor imaging catheters, this next generation enables high quality volumetric endoscopic OCT imaging in the human gastrointestinal (GI) tract. More importantly, this next generation endoscopic OCT first successfully demonstrated volumetric imaging of subsurface microvasculature in the human GI using endoscopic OCT angiography (OCTA) technique without requiring exogenous contrast agents. However, the reliability of performance of the endoscopic OCT and OCTA imaging is yet optimal as well as the robustness of the prototype micromotor imaging catheter. In addition, the clinical utility of this next generation ultrahigh speed OCT and OCTA platform has not been validated.

Therefore, in this thesis, in addition to solely improving the performance in the reliability, robustness and imaging coverage of the prototype micromotor imaging catheters, two different types of the micromotor imaging catheters were developed and subsequently demonstrated the unique advantages of either catheter design for future clinical applications. In one catheter design, a new micromotor imaging catheter successfully enabled high speed, 360-degree, unobstructed OCT imaging along circumferential/rotary directions using a novel DC brushless, hollow shaft micromotor. This catheter design showed promises to simplify the catheter assembly process and the imaging procedure of the prototype micromotor imaging catheters and potentially endoscopic OCM imaging in the human GI tract in the near future. Albeit the relatively imaging coverage due to the small catheter size, it allows high resolution imaging of the tissue surface, which can be used to guide the biopsy or assess treatment efficacy.

In the other catheter design, a micromotor balloon catheter was developed to overcome the limitation of the imaging coverage with small size catheters. Compared to conventional proximally actuated balloon catheters, in combination with ultrahigh speed OCT system

aforementioned, it allows high quality, wide field, *en face* OCT imaging of the swine esophagus in a depth resolved fashion. In addition, it promises to enable an integrated platform combining high speed OCT imaging with other endoscopic capabilities with future development. Most importantly, leveraging the ultrahigh speed OCT imaging and the development of nonuniform rotation correction algorithms, subsurface microvasculature over the entire circumference of the swine esophagus was first demonstrated using balloon catheters.

In addition to the technical development of the micromotor imaging catheters, a clinical study focused on the clinical utility of using the endoscopic OCTA technique on the pathologies of Barrett's Esophagus (BE) and dysplasia in BE was performed in collaboration with Dr. Hiroshi Mashimo, MD. PhD. in the GI clinics at the Veterans Affairs Boston Healthcare System (VHBHS, Jamaica campus). Using the ultrahigh speed endoscopic OCT system and prototype micromotor imaging catheters with improved imaging performance and mechanical robustness, patients undergoing BE surveillance program were enrolled and imaged with the OCT and OCTA techniques. This study involving 32 patients showed an overall 94% sensitivity and 69% specificity in differentiating dysplasia from BE without dysplasia using the OCTA features of abnormal vessel branching and heterogeneous vessel size.

Lastly, a laboratory study using *ex vivo* swine esophagus model was performed to investigate the feasibility of using high speed OCT for real time monitoring of the changes in tissue architectures in response to radiofrequency ablation with different RF energy settings. A linear increase of the coagulum thickness in response RFA application with increased energy setting was identified and measured by OCT imaging. This study demonstrated the potential to tailor a controlled RFA regimen under the guidance of real time OCT imaging. Leveraging the developed micromotor balloon platform, an OCT integrated RFA balloon catheter promises to improve the complexity in current RFA procedure where multiple cycles of RFA application and coagulum abrasion were required. Collectively, this thesis not only demonstrated the feasibility of using OCT to facilitate the detection of dysplasia but also the capability of OCT for real time monitoring of the RFA process, promising to advance the endoscopic management of esophageal neoplasia through the ultrahigh speed OCT platform developed.

6.2 Future Work

In continual of this thesis work, future efforts should be focused the following three different aspects: (1) improvement of the endoscopic OCT system, (2) implementation of the computer-aided diagnosis in the endoscopic OCTA images, (3) and clinical utility studies of other vascular related GI diseases.

6.2.1 Future improvement of the endoscopic OCT system.

In this thesis, a first generation of the ultrahigh speed endoscopic OCT system was developed and deployed in the GI clinics at VABHS to perform a series of clinical studies. In this system, a prototype MEMS tunable VCSEL light source was used as the light source, which requires a manual tuning process to start the laser. In addition, as a result of the sinusoidal driving waveform, the frequency sweep is not linear in time. Although the nonlinear frequency sweep can be corrected by external clocking the A/D sampling using optical clock generator from the MZI signal, the maximum imaging range becomes limited. Therefore, it is desirable to further improve the light source with an auto-tuning function to facilitate the user friendliness of the endoscopic OCT system. In addition, the VCSEL light source driving waveform can be modified to provide a linearized frequency sweep and hence improve the imaging range. Furthermore, multiple diode current drivers and the temperature controller required in the prototype VCSEL light source might not be required if a fully integrated OEM, next generation VCSEL light source was used, which promises to significantly decrease the footprint the of the endoscopic OCT system deployed in the GI clinics.

In addition, although the polarization artifact might be less severe in the endoscopic OCT images acquired using the micromotor catheters, it is difficult to keep the illumination beam with the same polarization state at different angular directions of the rotating beam. This might result in a low OCT signal intensity over regions corresponding to a particular angular location. In the commercial endoscopic OCT system, a polarization diversity detection scheme involving two separate photodetectors for individual polarization channels were used to mitigate the polarization artifact in the OCT images. However, in the current generation of the ultrahigh speed endoscopic OCT system, the polarization diversity detection was not implemented. Therefore, in some of the OCT datasets, polarization artifacts can still be observed, which might

affect the assessment of OCT or OCTA features with the corresponding tissue pathologies. Therefore, it is desirable to update the detection unit in the current system with the polarization diversity detection module to suppress the polarization artifacts potentially presented in the OCT images.

Lastly, although the structural OCT images were generated in real time as the images acquired in the current generation of the endoscopic OCT system, OCTA images were computed in post processing. As described in previous Chapters, a correction algorithm needs to be performed to remove or suppress the nonuniform rotation distortion (NURD) in the OCT images prior to computing the OCTA datasets, which is a time-intensive computation process. The limitation of real time OCTA display in the current system directly affected the yield of the OCTA datasets. Recently, several groups have demonstrated real time processing and visualization of the OCTA images immediately after the OCT acquisition using the state-of-the-art computation with Graphic Processing Units (GPU). Leveraging the large amount of cores inside the GPU, it is possible to perform both the NURD correction and OCTA computation in separate threading. In addition, rather than processing the entire large size volumetric OCT dataset, it might be more computational efficient by dividing the entire volumetric dataset into several smaller size datasets and generate the OCTA images of individual dataset afterward.

6.2.2 Computer-aided diagnosis in the endoscopic OCTA imaging

Recently, several studies have demonstrated the automatic algorithm to quantify the microvascular information in the OCTA images of the human retina. For example, in collaboration with the Friedrich-Alexander University Erlangen-Nürnberg (FAU) in Germany, our group has recently demonstrated an automatic intercapillary area-based algorithm for quantifying diabetes-related capillary dropout using OCTA. In this thesis, to validate the clinical utility of OCTA for dysplasia detection in BE, multiple readers were asked to review the OCTA images and identified the presence of either abnormal microvascular features in the OCTA images. Although a high accuracy was reported in identifying dysplasia in BE using the OCTA features, it is desirable to develop an automatic imaging analysis algorithm based the OCTA features and compare its performed with the blinded OCTA readings from multiple. An

automatic computation algorithm allows an objective assessment and promise to facilitate the future large scale studies

6.2.3 Clinical studies of GI diseases

In this thesis, we demonstrated the feasibility of using OCTA to identify microvascular features a potential marker for BE associated dysplasia. These initial results suggest the feasibility of applying OCTA technique on other vascular-related diseases to assess the efficacy of the endoscopic treatment accordingly in patients with long term follow-up. For example, Figure 6.1 shows the coregistered en face OCT/OCTA from a GAVE patient before and immediately after RFA treatment. Features of diffuse-type GAVE were observed endoscopically. Distorted surface mucosa pattern can be observed in OCT over the GAVE region (Fig. 6.1(A)), while OCTA shows ectatic vessels (Fig. 6.1(B)). Immediately post RFA, the tissue surface is obscured by coagulum (Fig. 6.1(C)), and microvasculature cannot be visualized due to signal attenuation (Fig. 6.1(D)).

6.3 Figures

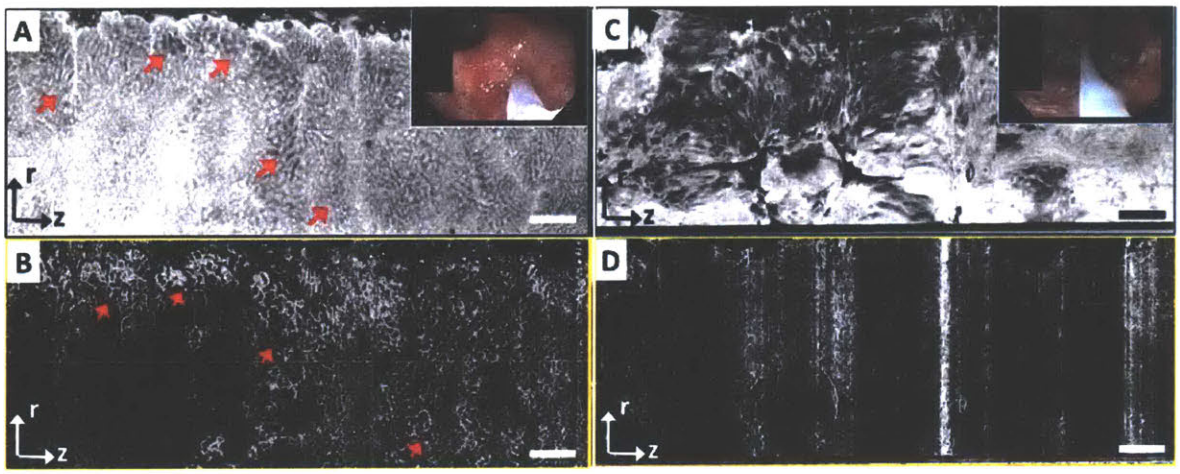

Figure 6.1. *En face* OCT and OCT angiography (OCTA) images from a patient with diffuse-type GAVE before radiofrequency ablation (RFA) (A, B) and immediately after RFA (C, D). (A) *En face* OCT image over the GAVE region at a depth of 260 μm showed distorted surface mucosal pattern (arrows). (B) *En face* OCTA at 260 μm depth showed ectatic vessels (red arrows), which are associated with erythematous spots as shown in the endoscopy image (inlet, A). (C) *En face* OCT image over the GAVE region immediately after RFA at a depth of 260 μm where tissue surface was obscured by coagulum, as shown in the corresponding white light endoscopy image (inlet, C). (D) OCTA at the same depth as (C) showed no microvasculature in regions of coagulum due to signal attenuation. Scale bars: 1 mm.

6.4 Publications Produced During Thesis Work

Publications [1-12] were produced between September 2012 – December 2016 during work on the PhD thesis.

[1] Z. Wang, B. Potsaid, L. Chen, C. Doerr, H. C. Lee, T. Nielson, V. Jayaraman, A. E. Cable, E. Swanson, and J. G. Fujimoto, "Cubic meter volume optical coherence tomography," *Optica,* vol. 3, pp. 1496-1503, Dec 20 2016.

[2] H. C. Lee, O. O. Ahsen, K. C. Liang, Z. Wang, C. Cleveland, L. Booth, B. Potsaid, V. Jayaraman, A. E. Cable, H. Mashimo, R. Langer, G. Traverso, and J. G. Fujimoto, "Circumferential optical coherence tomography angiography imaging of the swine esophagus using a micromotor balloon catheter," *Biomedical Optics Express,* vol. 7, pp. 2927-2942, Aug 1 2016.

[3] K. Liang, O. O. Ahsen, H. C. Lee, Z. Wang, B. M. Potsaid, M. Figueiredo, V. Jayaraman, A. E. Cable, Q. Huang, H. Mashimo, and J. G. Fujimoto, "Volumetric Mapping of Barrett's Esophagus and Dysplasia With en face Optical Coherence Tomography Tethered Capsule," *Am J Gastroenterol,* vol. 111, pp. 1664-1666, Nov 2016.

[4] Z. Wang, H. C. Lee, D. Vermeulen, L. Chen, T. Nielsen, S. Y. Park, A. Ghaemi, E. Swanson, C. Doerr, and J. Fujimoto, "Silicon photonic integrated circuit swept-source optical coherence tomography receiver with dual polarization, dual balanced, in-phase and quadrature detection," *Biomedical Optics Express,* vol. 6, pp. 2562-2574, Jul 1 2015.

[5] K. Liang, G. Traverso, H. C. Lee, O. O. Ahsen, Z. Wang, B. Potsaid, M. Giacomelli, V. Jayaraman, R. Barman, A. Cable, H. Mashimo, R. Langer, and J. G. Fujimoto, "Ultrahigh speed en face OCT capsule for endoscopic imaging," *Biomed Opt Express,* vol. 6, pp. 1146-63, Apr 1 2015.

[6] T. H. Tsai, H. C. Lee, O. O. Ahsen, K. C. Liang, M. G. Giacomelli, B. M. Potsaid, Y. K. K. Tao, V. Jayaraman, M. Figueiredo, Q. Huang, A. E. Cable, J. Fujimoto, and H. Mashimo, "Ultrahigh speed endoscopic optical coherence tomography for gastroenterology," *Biomedical Optics Express,* vol. 5, pp. 4387-4404, Dec 2014.

[7] O. O. Ahsen, H.-C. Lee, M. G. Giacomelli, Z. Wang, K. Liang, T.-H. Tsai, B. Potsaid, H. Mashimo, and J. G. Fujimoto, "Correction of rotational distortion for catheter-based en face OCT and OCT angiography," *Optics Letters,* vol. 39, pp. 5973-5976, 2014.

[8] T.-H. Tsai, O. O. Ahsen, H.-C. Lee, K. Liang, M. Figueiredo, Y. K. Tao, M. G. Giacomelli, B. M. Potsaid, V. Jayaraman, Q. Huang, A. E. Cable, J. G. Fujimoto, and H. Mashimo, "Endoscopic Optical Coherence Angiography Enables Three Dimensional Visualization of Subsurface Microvasculature," *Gastroenterology,* vol. 147, pp. 1219-1221, 2014.

[9] Z. Wang, H. C. Lee, O. O. Ahsen, B. Lee, W. Choi, B. Potsaid, J. Liu, V. Jayaraman, A. Cable, M. F. Kraus, K. C. Liang, J. Hornegger, and J. G. Fujimoto, "Depth-encoded all-fiber swept source polarization sensitive OCT," *Biomedical Optics Express,* vol. 5, pp. 2931-2949, Sep 1 2014.

[10] N. Zhang, T. H. Tsai, O. O. Ahsen, K. Liang, H. C. Lee, P. Xue, X. Li, and J. G. Fujimoto, "Compact piezoelectric transducer fiber scanning probe for optical coherence tomography," *Opt Lett,* vol. 39, pp. 186-8, Jan 15 2014.

[11] H. C. Lee, J. J. Liu, Y. Sheikine, A. D. Aguirre, J. L. Connolly, and J. G. Fujimoto, "Ultrahigh speed spectral-domain optical coherence microscopy," *Biomed Opt Express,* vol. 4, pp. 1236-54, 2013.

[12] T. H. Tsai, C. Zhou, Y. K. Tao, H. C. Lee, O. O. Ahsen, M. Figueiredo, T. Kirtane, D. C. Adler, J. M. Schmitt, Q. Huang, J. G. Fujimoto, and H. Mashimo, "Structural markers observed with endoscopic 3-dimensional optical coherence tomography correlating with Barrett's esophagus radiofrequency ablation treatment response (with videos)," *Gastrointest Endosc,* vol. 76, pp. 1104-12, Dec 2012.

7.0 Bibliography

[1] R. M. Zagari, L. Fuccio, M. A. Wallander, S. Johansson, R. Fiocca, S. Casanova, B. Y. Farahmand, C. C. Winchester, E. Roda, and F. Bazzoli, "Gastro-oesophageal reflux symptoms, oesophagitis and Barrett's oesophagus in the general population: the Loiano-Monghidoro study," *Gut,* vol. 57, pp. 1354-9, Oct 2008.

[2] A. Rustgi and H. B. El-Serag, "Esophageal carcinoma," *N Engl J Med,* vol. 372, pp. 1472-3, Apr 09 2015.

[3] N. J. Shaheen, "Advances in Barrett's esophagus and esophageal adenocarcinoma," *Gastroenterology,* vol. 128, pp. 1554-1566, May 2005.

[4] H. Pohl and H. G. Welch, "The role of overdiagnosis and reclassification in the marked increase of esophageal adenocarcinoma incidence," *J Natl Cancer Inst,* vol. 97, pp. 142-6, Jan 19 2005.

[5] S. J. Spechler, "Barrett esophagus and risk of esophageal cancer: a clinical review," *JAMA,* vol. 310, pp. 627-36, Aug 14 2013.

[6] J. B. Taylor and J. H. Rubenstein, "Meta-analyses of the effect of symptoms of gastroesophageal reflux on the risk of Barrett's esophagus," *Am J Gastroenterol,* vol. 105, pp. 1729, 1730-7; quiz 1738, Aug 2010.

[7] S. J. Spechler, "Dysplasia in Barrett's esophagus: limitations of current management strategies," *American Journal of Gastroenterology,* vol. 100, pp. 927-935, Apr 2005.

[8] F. Hvid-Jensen, L. Pedersen, A. M. Drewes, H. T. Sorensen, and P. Funch-Jensen, "Incidence of Adenocarcinoma among Patients with Barrett's Esophagus," *New England Journal of Medicine,* vol. 365, pp. 1375-1383, Oct 13 2011.

[9] T. K. Desai, K. Krishnan, N. Samala, J. Singh, J. Cluley, S. Perla, and C. W. Howden, "The incidence of oesophageal adenocarcinoma in non-dysplastic Barrett's oesophagus: a meta-analysis," *Gut,* vol. 61, pp. 970-6, Jul 2012.

[10] B. J. Reid, D. S. Levine, G. Longton, P. L. Blount, and P. S. Rabinovitch, "Predictors of progression to cancer in Barrett's esophagus: Baseline histology and flow cytometry identify low- and high-risk patient subsets," *American Journal of Gastroenterology,* vol. 95, pp. 1669-1676, Jul 2000.

[11] N. S. Buttar, K. K. Wang, T. J. Sebo, D. M. Riehle, K. K. Krishnadath, L. S. Lutzke, M. A. Anderson, T. M. Petterson, and L. J. Burgart, "Extent of high-grade dysplasia in Barrett's esophagus correlates with risk of adenocarcinoma," *Gastroenterology,* vol. 120, pp. 1630-1639, Jun 2001.

[12] A. J. Cameron and H. A. Carpenter, "Barrett's esophagus, high-grade dysplasia, and early adenocarcinoma: A pathological study," *American Journal of Gastroenterology,* vol. 92, pp. 586-591, Apr 1997.

[13] O. Pech, L. Gossner, H. Manner, A. May, T. Rabenstein, A. Behrens, M. Berres, J. Huijsmans, M. Vieth, M. Stolte, and C. Ell, "Prospective evaluation of the macroscopic types and location of early Barrett's neoplasia in 380 lesions," *Endoscopy,* vol. 39, pp. 588-593, Jul 2007.

[14] P. Sharma, J. Dent, D. Armstrong, J. J. G. H. M. Bergman, L. Gossner, Y. Hoshihara, J. A. Jankowski, O. Junghard, L. Lundell, G. N. J. Tytgat, and M. Vieth, "The Development and Validation of an Endoscopic Grading System for Barrett's Esophagus: The Prague C & M Criteria," *Gastroenterology,* vol. 131, pp. 1392-1399, 2006.

[15] R. C. Fitzgerald, I. T. Saeed, D. Khoo, M. J. Farthing, and W. R. Burnham, "Rigorous surveillance protocol increases detection of curable cancers associated with Barrett's esophagus," *Digestive Diseases and Sciences,* vol. 46, pp. 1892-8, Sep 2001.

[16] D. Das, S. Ishaq, R. Harrison, K. Kosuri, E. Harper, J. Decaestecker, R. Sampliner, S. Attwood, H. Barr, P. Watson, P. Moayyedi, and J. Jankowski, "Management of Barrett's esophagus in the UK: overtreated and underbiopsied but improved by the introduction of a national randomized trial," *Am J Gastroenterol,* vol. 103, pp. 1079-89, May 2008.

[17] W. L. Curvers, F. P. Peters, B. Elzer, A. J. Schaap, L. C. Baak, A. van Oijen, R. M. Mallant-Hent, F. Ten Kate, K. K. Krishnadath, and J. J. Bergman, "Quality of Barrett's surveillance in The Netherlands: a standardized review of endoscopy and pathology reports," *Eur J Gastroenterol Hepatol,* vol. 20, pp. 601-7, Jul 2008.

[18] M. I. Canto, "Vital staining and Barrett's esophagus," *Gastrointest Endosc,* vol. 49, pp. S12-6, Mar 1999.

[19] V. R. Muthusamy, S. Kim, and M. B. Wallace, "Advanced Imaging in Barrett's Esophagus," *Gastroenterology Clinics of North America,* vol. 44, pp. 439-+, Jun 2015.

[20] M. I. F. Canto, S. Setrakian, J. E. Willis, A. Chak, R. E. Petras, and M. V. Sivak, "Methylene blue staining of dysplastic and nondysplastic Barrett's esophagus: An in vivo and ex vivo study," *Endoscopy,* vol. 33, pp. 391-400, May 2001.

[21] P. Sharma, M. Topalovski, M. S. Mayo, and A. P. Weston, "Methylene blue chromoendoscopy for detection of short-segment Barrett's esophagus," *Gastrointest Endosc,* vol. 54, pp. 289-93, Sep 2001.

[22] J. M. Wo, M. B. Ray, S. Mayfield-Stokes, G. Al-Sabbagh, F. Gebrail, S. P. Slone, and M. A. Wilson, "Comparison of methylene blue-directed biopsies and conventional biopsies in the detection of intestinal metaplasia and dysplasia in Barrett's esophagus: a preliminary study," *Gastrointest Endosc,* vol. 54, pp. 294-301, Sep 2001.

[23] L. Gossner, O. Pech, A. May, M. Vieth, M. Stolte, and C. Ell, "Comparison of methylene blue-directed biopsies and four-quadrant biopsies in the detection of high-grade intraepithelial neoplasia and early cancer in Barrett's oesophagus," *Dig Liver Dis,* vol. 38, pp. 724-9, Oct 2006.

[24] C. H. Lim, O. Rotimi, S. P. L. Dexter, and A. T. R. Axon, "Randomized crossover study that used methylene blue or random 4-quadrant biopsy for the diagnosis of dysplasia in Barrett's esophagus," *Gastrointestinal Endoscopy,* vol. 64, pp. 195-199, Aug 2006.

[25] S. Ngamruengphong, V. K. Sharma, and A. Das, "Diagnostic yield of methylene blue chromoendoscopy for detecting specialized intestinal metaplasia and dysplasia in Barrett's esophagus: a meta-analysis," *Gastrointestinal Endoscopy,* vol. 69, pp. 1021-1028, May 2009.

[26] J. R. Olliver, C. P. Wild, P. Sahay, S. Dexter, and L. J. Hardie, "Chromoendoscopy with methylene blue and associated DNA damage in Barrett's oesophagus," *Lancet,* vol. 362, pp. 373-4, Aug 2 2003.

[27] R. Lambert, J. F. Rey, and R. Sankaranarayanan, "Magnification and chromoscopy with the acetic acid test," *Endoscopy,* vol. 35, pp. 437-45, May 2003.

[28] M. Guelrud, I. Herrera, H. Essenfeld, and J. Castro, "Enhanced magnification endoscopy: a new technique to identify specialized intestinal metaplasia in Barrett's esophagus," *Gastrointestinal Endoscopy,* vol. 53, pp. 559-565, May 2001.

[29] G. Longcroft-Wheaton, M. Duku, R. Mead, D. Poller, and P. Bhandari, "Acetic Acid Spray Is an Effective Tool for the Endoscopic Detection of Neoplasia in Patients With

Barrett's Esophagus," *Clinical Gastroenterology and Hepatology,* vol. 8, pp. 843-847, Oct 2010.

[30] J. Pohl, O. Pech, A. May, H. Manner, A. Fissler-Eckhoff, and C. Ell, "Incidence of Macroscopically Occult Neoplasias in Barrett's Esophagus: Are Random Biopsies Dispensable in the Era of Advanced Endoscopic Imaging?," *American Journal of Gastroenterology,* vol. 105, pp. 2350-2356, Nov 2010.

[31] N. J. Shaheen, P. Sharma, B. F. Overholt, H. C. Wolfsen, R. E. Sampliner, K. K. Wang, J. A. Galanko, M. P. Bronner, J. R. Goldblum, A. E. Bennett, B. A. Jobe, G. M. Eisen, M. B. Fennerty, J. G. Hunter, D. E. Fleischer, V. K. Sharma, R. H. Hawes, B. J. Hoffman, R. I. Rothstein, S. R. Gordon, H. Mashimo, K. J. Chang, V. R. Muthusamy, S. A. Edmundowicz, S. J. Spechler, A. A. Siddiqui, R. F. Souza, A. Infantolino, G. W. Falk, M. B. Kimmey, R. D. Madanick, A. Chak, and C. J. Lightdale, "Radiofrequency Ablation in Barrett's Esophagus with Dysplasia," *New England Journal of Medicine,* vol. 360, pp. 2277-2288, 2009.

[32] K. Gono, T. Obi, M. Yamaguchi, N. Ohyama, H. Machida, Y. Sano, S. Yoshida, Y. Hamamoto, and T. Endo, "Appearance of enhanced tissue features in narrow-band endoscopic imaging," *J Biomed Opt,* vol. 9, pp. 568-77, May-Jun 2004.

[33] M. A. Kara, M. Ennahachi, P. Fockens, F. J. W. ten Kate, and J. J. G. H. M. Bergman, "Detection and classification of the mucosal and vascular patterns (mucosal morphology) in Barrett's esophagus by using narrow band imaging," *Gastrointestinal Endoscopy,* vol. 64, pp. 155-166, 2006.

[34] P. Sharma, A. Bansal, S. Mathur, S. Wani, R. Cherian, D. McGregor, A. Higbee, S. Hall, and A. Weston, "The utility of a novel narrow band imaging endoscopy system in patients with Barrett's esophagus," *Gastrointestinal Endoscopy,* vol. 64, pp. 167-175, 2006.

[35] P. Sharma, R. H. Hawes, A. Bansal, N. Gupta, W. Curvers, A. Rastogi, M. Singh, M. Hall, S. C. Mathur, S. B. Wani, B. Hoffman, S. Gaddam, P. Fockens, and J. J. Bergman, "Standard endoscopy with random biopsies versus narrow band imaging targeted biopsies in Barrett's oesophagus: a prospective, international, randomised controlled trial," *Gut,* vol. 62, pp. 15-21, Jan 2013.

[36] R. Kiesslich, L. Gossner, M. Goetz, A. Dahlmann, M. Vieth, M. Stolte, A. Hoffman, M. Jung, B. Nafe, P. R. Galle, and M. F. Neurath, "In vivo histology of Barrett's esophagus and associated neoplasia by confocal laser endomicroscopy," *Clin Gastroenterol Hepatol,* vol. 4, pp. 979-87, Aug 2006.

[37] M. B. Wallace and P. Fockens, "Probe-Based Confocal Laser Endomicroscopy," *Gastroenterology,* vol. 136, pp. 1509-1513, 2009.

[38] M. Goetz, T. Toermer, M. Vieth, K. Dunbar, A. Hoffman, P. R. Galle, M. F. Neurath, P. Delaney, and R. Kiesslich, "Simultaneous confocal laser endomicroscopy and chromoendoscopy with topical cresyl violet," *Gastrointest Endosc,* vol. 70, pp. 959-68, Nov 2009.

[39] M. Wallace, G. Y. Lauwers, Y. Chen, E. Dekker, P. Fockens, P. Sharma, and A. Meining, "Miami classification for probe-based confocal laser endomicroscopy," *Endoscopy,* vol. 43, pp. 882-891, May 2011.

[40] M. I. Canto, S. Anandasabapathy, W. Brugge, G. W. Falk, K. B. Dunbar, Z. Zhang, K. Woods, J. A. Almario, U. Schell, J. Goldblum, A. Maitra, E. Montgomery, and R. Kiesslich, "In vivo endomicroscopy improves detection of Barrett's esophagus-related

neoplasia: a multicenter international randomized controlled trial (with video)," *Gastrointest Endosc,* vol. 79, pp. 211-21, Feb 2014.

[41] K. B. Dunbar, P. Okolo, 3rd, E. Montgomery, and M. I. Canto, "Confocal laser endomicroscopy in Barrett's esophagus and endoscopically inapparent Barrett's neoplasia: a prospective, randomized, double-blind, controlled, crossover trial," *Gastrointest Endosc,* vol. 70, pp. 645-54, Oct 2009.

[42] T. J. Muldoon, S. Anandasabapathy, D. Maru, and R. Richards-Kortum, "High-resolution imaging in Barrett's esophagus: a novel, low-cost endoscopic microscope," *Gastrointestinal Endoscopy,* vol. 68, pp. 737-744, 2008.

[43] J. S. Louie, R. Richards-Kortum, and S. Anandasabapathy, "Applications and advancements in the use of high-resolution microendoscopy for detection of gastrointestinal neoplasia," *Clin Gastroenterol Hepatol,* vol. 12, pp. 1789-92, Nov 2014.

[44] H. Inoue, M. Endo, K. Takeshita, K. Yoshino, Y. Muraoka, and H. Yoneshima, "A new simplified technique of endoscopic esophageal mucosal resection using a cap-fitted panendoscope (EMRC)," *Surg Endosc,* vol. 6, pp. 264-5, Sep-Oct 1992.

[45] S. V. Kantsevoy, D. G. Adler, J. D. Conway, D. L. Diehl, F. A. Farraye, R. Kwon, P. Mamula, S. Rodriguez, R. J. Shah, L. M. Wong Kee Song, and W. M. Tierney, "Endoscopic mucosal resection and endoscopic submucosal dissection," *Gastrointest Endosc,* vol. 68, pp. 11-8, Jul 2008.

[46] F. P. Peters, M. A. Kara, W. L. Curvers, W. D. Rosmolen, P. Fockens, K. K. Krishnadath, F. J. Ten Kate, and J. J. Bergman, "Multiband mucosectomy for endoscopic resection of Barrett's esophagus: feasibility study with matched historical controls," *Eur J Gastroenterol Hepatol,* vol. 19, pp. 311-5, Apr 2007.

[47] A. May, L. Gossner, O. Pech, H. Muller, M. Vieth, M. Stolte, and C. Ell, "Intraepithelial high-grade neoplasia and early adenocarcinoma in short-segment Barrett's esophagus (SSBE): curative treatment using local endoscopic treatment techniques," *Endoscopy,* vol. 34, pp. 604-10, Aug 2002.

[48] O. Pech, A. May, L. Gossner, T. Rabenstein, H. Manner, J. Huijsmans, M. Vieth, M. Stolte, M. Berres, and C. Ell, "Curative endoscopic therapy in patients with early esophageal squamous-cell carcinoma or high-grade intraepithelial neoplasia," *Endoscopy,* vol. 39, pp. 30-5, Jan 2007.

[49] C. Ell, A. May, O. Pech, L. Gossner, E. Guenter, A. Behrens, L. Nachbar, J. Huijsmans, M. Vieth, and M. Stolte, "Curative endoscopic resection of early esophageal adenocarcinomas (Barrett's cancer)," *Gastrointest Endosc,* vol. 65, pp. 3-10, Jan 2007.

[50] R. E. Pouw, S. Seewald, J. J. Gondrie, P. H. Deprez, H. Piessevaux, H. Pohl, T. Rösch, N. Soehendra, and J. J. Bergman, "Stepwise radical endoscopic resection for eradication of Barrett's oesophagus with early neoplasia in a cohort of 169 patients," *Gut,* vol. 59, pp. 1169-1177, September 1, 2010 2010.

[51] R. E. Pouw, K. Wirths, P. Eisendrath, C. M. Sondermeijer, F. J. Ten Kate, P. Fockens, J. Deviere, H. Neuhaus, and J. J. Bergman, "Efficacy of radiofrequency ablation combined with endoscopic resection for barrett's esophagus with early neoplasia," *Clin Gastroenterol Hepatol,* vol. 8, pp. 23-9, Jan 2010.

[52] S. Wani, S. C. Mathur, W. L. Curvers, V. Singh, L. A. Herrero, S. B. Hall, O. Ulusarac, R. Cherian, D. H. McGregor, A. Bansal, A. Rastogi, B. Ahmed, M. Singh, S. Gaddam, F. J. Ten Kate, J. Bergman, and P. Sharma, "Greater Interobserver Agreement by Endoscopic

Mucosal Resection Than Biopsy Samples in Barrett's Dysplasia," *Clinical Gastroenterology and Hepatology,* vol. 8, pp. 783-788.e2, 2010.

[53] H. Sayana, S. B. Wani, J. D. Keighley, A. Bansal, A. Rastogi, S. C. Mathur, and P. Sharma, "Endoscopic mucosal resection (EMR)as a diagnostic tool in Barrett's esophagus (Be)patients with high-grade dysplasia (HGD)and early esophageal adenocarcinoma (EAC): A systematic review," *Gastroenterology,* vol. 134, pp. A724-A724, Apr 2008.

[54] A. Larghi, C. J. Lightdale, L. Memeo, G. Bhagat, N. Okpara, and H. Rotterdam, "EUS followed by EMR for staging of high-grade dysplasia and early cancer in Barrett's esophagus," *Gastrointest Endosc,* vol. 62, pp. 16-23, Jul 2005.

[55] S. J. Spechler, P. Sharma, R. F. Souza, J. M. Inadomi, and N. J. Shaheen, "American Gastroenterological Association Technical Review on the Management of Barrett's Esophagus," *Gastroenterology,* vol. 140, pp. e18-e52, 2011.

[56] N. J. Shaheen, B. F. Overholt, R. E. Sampliner, H. C. Wolfsen, K. K. Wang, D. E. Fleischer, V. K. Sharma, G. M. Eisen, M. B. Fennerty, J. G. Hunter, M. P. Bronner, J. R. Goldblum, A. E. Bennett, H. Mashimo, R. I. Rothstein, S. R. Gordon, S. A. Edmundowicz, R. D. Madanick, A. F. Peery, V. R. Muthusamy, K. J. Chang, M. B. Kimmey, S. J. Spechler, A. A. Siddiqui, R. F. Souza, A. Infantolino, J. A. Dumot, G. W. Falk, J. A. Galanko, B. A. Jobe, R. H. Hawes, B. J. Hoffman, P. Sharma, A. Chak, and C. J. Lightdale, "Durability of Radiofrequency Ablation in Barrett's Esophagus With Dysplasia," *Gastroenterology,* vol. 141, pp. 460-468, 2011.

[57] W. J. Bulsiewicz and N. J. Shaheen, "The role of radiofrequency ablation in the management of Barrett's esophagus," *Gastrointest Endosc Clin N Am,* vol. 21, pp. 95-109, Jan 2011.

[58] E. S. Orman, N. Li, and N. J. Shaheen, "Efficacy and Durability of Radiofrequency Ablation for Barrett's Esophagus: Systematic Review and Meta-analysis," *Clinical Gastroenterology and Hepatology,* vol. 11, pp. 1245-1255, Oct 2013.

[59] P. Sharma, S. Wani, and A. Rastogi, "Endoscopic therapy for high-grade dysplasia in Barrett's esophagus: ablate, resect, or both?," *Gastrointestinal Endoscopy,* vol. 66, pp. 469-474, Sep 2007.

[60] D. E. Fleischer, B. F. Overholt, V. K. Sharma, A. Reymunde, M. B. Kimmey, R. Chuttani, K. J. Chang, R. Muthasamy, C. J. Lightdale, N. Santiago, D. K. Pleskow, P. J. Dean, and K. K. Wang, "Endoscopic radiofrequency ablation for Barrett's esophagus: 5-year outcomes from a prospective multicenter trial," *Endoscopy,* vol. 42, pp. 781,789, 30.09.2010 2010.

[61] B. Vaccaro, S. Gonzalez, J. Poneros, P. Stevens, K. Capiak, C. Lightdale, and J. Abrams, "Detection of Intestinal Metaplasia After Successful Eradication of Barrett's Esophagus with Radiofrequency Ablation," *Digestive Diseases and Sciences,* vol. 56, pp. 1996-2000, 2011.

[62] J. G. Baust and A. A. Gage, "The molecular basis of cryosurgery," *BJU Int,* vol. 95, pp. 1187-91, Jun 2005.

[63] M. H. Johnston, J. A. Eastone, J. D. Horwhat, J. Cartledge, J. S. Mathews, and J. R. Foggy, "Cryoablation of Barrett's esophagus: a pilot study," *Gastrointestinal Endoscopy,* vol. 62, pp. 842-848, 2005.

[64] B. D. Greenwald, J. A. Dumot, J. D. Horwhat, C. J. Lightdale, and J. A. Abrams, "Safety, tolerability, and efficacy of endoscopic low-pressure liquid nitrogen spray cryotherapy in the esophagus," *Diseases of the Esophagus,* vol. 23, pp. 13-19, 2010.

[65] N. J. Shaheen, B. D. Greenwald, A. F. Peery, J. A. Dumot, N. S. Nishioka, H. C. Wolfsen, J. S. Burdick, J. A. Abrams, K. K. Wang, D. Mallat, M. H. Johnston, A. M. Zfass, J. O. Smith, J. S. Barthel, and C. J. Lightdale, "Safety and efficacy of endoscopic spray cryotherapy for Barrett's esophagus with high-grade dysplasia," *Gastrointestinal Endoscopy,* vol. 71, pp. 680-685, 2010.

[66] K. D. Halsey, J. W. Chang, A. Waldt, and B. D. Greenwald, "Recurrent disease following endoscopic ablation of Barrett's high-grade dysplasia with spray cryotherapy," *Endoscopy,* vol. 43, pp. 844,848, 07.10.2011 2011.

[67] D. W. Scholvinck, H. T. Kunzli, C. Kestens, P. D. Siersema, F. P. Vleggaar, M. I. Canto, H. Cosby, J. A. Abrams, C. J. Lightdale, E. Tejeda-Ramirez, S. R. DeMeester, C. L. Greene, B. A. Jobe, J. Peters, J. J. Bergman, and B. L. Weusten, "Treatment of Barrett's esophagus with a novel focal cryoablation device: a safety and feasibility study," *Endoscopy,* vol. 47, pp. 1106-12, Dec 2015.

[68] D. Huang, E. A. Swanson, C. P. Lin, J. S. Schuman, W. G. Stinson, W. Chang, M. R. Hee, T. Flotte, K. Gregory, C. A. Puliafito, and J. G. Fujimoto, "Optical Coherence Tomography," *Science,* vol. 254, pp. 1178-1181, Nov 22 1991.

[69] W. Drexler, U. Morgner, R. K. Ghanta, F. X. Kärtner, J. S. Schuman, and J. G. Fujimoto, "Ultrahigh-resolution ophthalmic optical coherence tomography," *Nature Medicine,* vol. 7, pp. 502-507, Apr 2001.

[70] G. J. Tearney, M. E. Brezinski, S. A. Boppart, B. E. Bouma, N. Weissman, J. F. Southern, E. A. Swanson, and J. G. Fujimoto, "Catheter-based optical imaging of a human coronary artery," *Circulation,* vol. 94, p. 3013, 1996.

[71] J. G. Fujimoto, S. A. Boppart, G. J. Tearney, B. E. Bouma, C. Pitris, and M. E. Brezinski, "High resolution in vivo intra-arterial imaging with optical coherence tomography," *Heart,* vol. 82, pp. 128-33, Aug 1999.

[72] G. J. Tearney, M. E. Brezinski, J. F. Southern, B. E. Bouma, S. A. Boppart, and J. G. Fujimoto, "Optical biopsy in human gastrointestinal tissue using optical coherence tomography," *The American journal of gastroenterology,* vol. 92, pp. 1800-4, Oct 1997.

[73] B. E. Bouma, G. J. Tearney, C. C. Compton, and N. S. Nishioka, "High-resolution imaging of the human esophagus and stomach in vivo using optical coherence tomography," *Gastrointestinal Endoscopy,* vol. 51, pp. 467-474, 2000.

[74] M. V. Sivak, Jr., K. Kobayashi, J. A. Izatt, A. M. Rollins, R. Ung-Runyawee, A. Chak, R. C. Wong, G. A. Isenberg, and J. Willis, "High-resolution endoscopic imaging of the GI tract using optical coherence tomography," *Gastrointestinal endoscopy,* vol. 51, pp. 474-9, Apr 2000.

[75] G. J. Tearney, M. E. Brezinski, J. F. Southern, B. E. Bouma, S. A. Boppart, and J. G. Fujimoto, "Optical biopsy in human urologic tissue using optical coherence tomography," *The Journal of urology,* vol. 157, pp. 1915-9, May 1997.

[76] M. C. Pierce, J. Strasswimmer, B. H. Park, B. Cense, and J. F. de Boer, "Advances in optical coherence tomography imaging for dermatology," *Journal of Investigative Dermatology,* vol. 123, pp. 458-463, SEP 2004.

[77] T. Gambichler, G. Moussa, M. Sand, D. Sand, P. Altmeyer, and K. Hoffmann, "Applications of optical coherence tomography in dermatology," *J Dermatol Sci,* vol. 40, pp. 85-94, Nov 2005.

[78] C. Pitris, A. Goodman, S. A. Boppart, J. J. Libus, J. G. Fujimoto, and M. E. Brezinski, "High-resolution imaging of gynecologic neoplasms using optical coherence tomography," *Obstetrics and gynecology,* vol. 93, pp. 135-9, Jan 1999.

[79] P. F. Escobar, J. L. Belinson, A. White, N. M. Shakhova, F. I. Feldchtein, M. V. Kareta, and N. D. Gladkova, "Diagnostic efficacy of optical coherence tomography in the management of preinvasive and invasive cancer of uterine cervix and vulva," *International Journal of Gynecological Cancer,* vol. 14, pp. 470-474, MAY-JUN 2004.

[80] L. P. Hariri, G. T. Bonnema, K. Schmidt, A. M. Winkler, V. Korde, K. D. Hatch, J. R. Davis, M. A. Brewer, and J. K. Barton, "Laparoscopic optical coherence tomography imaging of human ovarian cancer," *Gynecologic Oncology,* vol. 114, pp. 188-194, Aug 2009.

[81] G. J. Tearney, M. E. Brezinski, B. E. Bouma, S. A. Boppart, C. Pitvis, J. F. Southern, and J. G. Fujimoto, "In vivo endoscopic optical biopsy with optical coherence tomography," *Science,* vol. 276, pp. 2037-2039, 1997/06/27 1997.

[82] A. M. Sergeev, V. M. Gelikonov, G. V. Gelikonov, F. I. Feldchtein, R. V. Kuranov, N. D. Gladkova, N. M. Shakhova, L. B. Suopova, A. V. Shakhov, I. A. Kuznetzova, A. N. Denisenko, V. V. Pochinko, Y. P. Chumakov, and O. S. Streltzova, "In vivo endoscopic OCT imaging of precancer and cancer states of human mucosa," *Optics Express,* vol. 1, 1997/12/22 1997.

[83] S. Jäckle, N. Gladkova, F. Feldchtein, A. Terentieva, B. Brand, G. Gelikonov, V. Gelikonov, A. Sergeev, A. Fritscher-Ravens, J. Freund, U. Seitz, S. Soehendra, and N. Schrödern, "In vivo endoscopic optical coherence tomography of the human gastrointestinal tract--toward optical biopsy," *Endoscopy,* vol. 32, pp. 743-9, Oct 2000.

[84] X. D. Li, S. A. Boppart, J. Van Dam, H. Mashimo, M. Mutinga, W. Drexler, M. Klein, C. Pitris, M. L. Krinsky, M. E. Brezinski, and J. G. Fujimoto, "Optical coherence tomography: advanced technology for the endoscopic imaging of Barrett's esophagus," *Endoscopy,* vol. 32, pp. 921-30, Dec 2000.

[85] J. M. Poneros, S. Brand, B. E. Bouma, G. J. Tearney, C. C. Compton, and N. S. Nishioka, "Diagnosis of specialized intestinal metaplasia by optical coherence tomography," *Gastroenterology,* vol. 120, pp. 7-12, Jan 2001.

[86] S. H. Yun, G. J. Tearney, B. J. Vakoc, M. Shishkov, W. Y. Oh, A. E. Desjardins, M. J. Suter, R. C. Chan, J. A. Evans, I. K. Jang, N. S. Nishioka, J. F. de Boer, and B. E. Bouma, "Comprehensive volumetric optical microscopy in vivo," *Nature Medicine,* vol. 12, pp. 1429-1433, Dec 2006.

[87] D. C. Adler, Y. Chen, R. Huber, J. Schmitt, J. Connolly, and J. G. Fujimoto, "Three-dimensional endomicroscopy using optical coherence tomography," *Nature Photonics,* vol. 1, pp. 709-716, Dec 2007.

[88] B. J. Vakoc, M. Shishko, S. H. Yun, W. Y. Oh, M. J. Suter, A. E. Desjardins, J. A. Evans, N. S. Nishioka, G. J. Tearney, and B. E. Bouma, "Comprehensive esophageal microscopy by using optical frequency-domain imaging (with video)," *Gastrointestinal Endoscopy,* vol. 65, pp. 898-905, May 2007.

[89] B. Shen, G. Zuccaro, Jr., T. L. Gramlich, N. Gladkova, P. Trolli, M. Kareta, C. P. Delaney, J. T. Connor, B. A. Lashner, C. L. Bevins, F. Feldchtein, F. H. Remzi, M. L. Bambrick, and V. W. Fazio, "In vivo colonoscopic optical coherence tomography for transmural inflammation in inflammatory bowel disease," *Clin Gastroenterol Hepatol,* vol. 2, pp. 1080-7, Dec 2004.

[90] C. Zhou, D. C. Adler, L. Becker, Y. Chen, T.-H. Tsai, M. Figueiredo, J. M. Schmitt, J. G. Fujimoto, and H. Mashimo, "Effective treatment of chronic radiation proctitis using radiofrequency ablation " *Therapeutic Advances in Gastroenterology,* vol. 2, pp. 149-156, 2009.

[91] U. Seitz, J. Freund, S. Jaeckle, F. Feldchtein, S. Bohnacker, F. Thonke, N. Gladkova, B. Brand, S. Schröder, and N. Soehendra, "First in vivo optical coherence tomography in the human bile duct," *Endoscopy,* vol. 33, pp. 1018-21, Dec 2001.

[92] J. M. Poneros, G. J. Tearney, M. Shiskov, P. B. Kelsey, G. Y. Lauwers, N. S. Nishioka, and B. E. Bouma, "Optical coherence tomography of the biliary tree during ERCP," *Gastrointestinal endoscopy,* vol. 55, pp. 84-8, Jan 2002.

[93] J. A. Evans, B. E. Bouma, J. Bressner, M. Shishkov, G. Y. Lauwers, M. Mino-Kenudson, N. S. Nishioka, and G. J. Tearney, "Identifying intestinal metaplasia at the squamocolumnar junction by using optical coherence tomography," *Gastrointestinal Endoscopy,* vol. 65, pp. 50-56, Jan 2007.

[94] G. Isenberg, M. V. Sivak Jr, A. Chak, R. C. K. Wong, J. E. Willis, B. Wolf, D. Y. Rowland, A. Das, and A. Rollins, "Accuracy of endoscopic optical coherence tomography in the detection of dysplasia in Barrett's esophagus: a prospective, double-blinded study," *Gastrointestinal Endoscopy,* vol. 62, pp. 825-831, 2005.

[95] J. A. Evans, J. M. Poneros, B. E. Bouma, J. Bressner, E. F. Halpern, M. Shishkov, G. Y. Lauwers, M. Mino-Kenudson, N. S. Nishioka, and G. J. Tearney, "Optical coherence tomography to identify intramucosal carcinoma and high-grade dysplasia in Barrett's esophagus," *Clinical Gastroenterology and Hepatology,* vol. 4, pp. 38-43, Jan 2006.

[96] C. L. Leggett, E. C. Gorospe, D. K. Chan, P. Muppa, V. Owens, T. C. Smyrk, M. Anderson, L. S. Lutzke, G. Tearney, and K. K. Wang, "Comparative diagnostic performance of volumetric laser endomicroscopy and confocal laser endomicroscopy in the detection of dysplasia associated with Barrett's esophagus," *Gastrointest Endosc,* vol. 83, pp. 880-888 e2, May 2016.

[97] X. Qi, M. V. Sivak, G. Isenberg, J. E. Willis, and A. M. Rollins, "Computer-aided diagnosis of dysplasia in Barrett's esophagus using endoscopic optical coherence tomography," *Journal of Biomedical Optics,* vol. 11, p. 10, Jul-Aug 2006.

[98] M. A. Choma, M. V. Sarunic, C. H. Yang, and J. A. Izatt, "Sensitivity advantage of swept source and Fourier domain optical coherence tomography," *Optics Express,* vol. 11, pp. 2183-2189, SEP 8 2003.

[99] R. Leitgeb, C. K. Hitzenberger, and A. F. Fercher, "Performance of Fourier domain vs. time domain optical coherence tomography," *Optics Express,* vol. 11, pp. 889-894, 2003/04/21 2003.

[100] D. C. Adler, C. Zhou, T. H. Tsai, H. C. Lee, L. Becker, J. M. Schmitt, Q. Huang, J. G. Fujimoto, and H. Mashimo, "Three-dimensional optical coherence tomography of Barrett's esophagus and buried glands beneath neosquamous epithelium following radiofrequency ablation," *Endoscopy,* vol. 41, pp. 773-776, Sep 2009.

[101] T. H. Tsai, C. Zhou, H. C. Lee, Y. K. Tao, O. O. Ahsen, M. Figueiredo, D. C. Adler, J. M. Schmitt, Q. Huang, J. G. Fujimoto, and H. Mashimo, "Comparison of Tissue Architectural Changes between Radiofrequency Ablation and Cryospray Ablation in Barrett's Esophagus Using Endoscopic Three-Dimensional Optical Coherence Tomography," *Gastroenterology Research and Practice,* 2012.

[102] T. H. Tsai, C. Zhou, Y. K. Tao, H. C. Lee, O. O. Ahsen, M. Figueiredo, T. Kirtane, D. C. Adler, J. M. Schmitt, Q. Huang, J. G. Fujimoto, and H. Mashimo, "Structural markers observed with endoscopic 3-dimensional optical coherence tomography correlating with Barrett's esophagus radiofrequency ablation treatment response," *Gastrointestinal Endoscopy,* vol. 76, pp. 1104-1112, Dec 2012.

[103] C. Zhou, T. H. Tsai, H. C. Lee, T. Kirtane, M. Figueiredo, Y. K. K. Tao, O. O. Ahsen, D. C. Adler, J. M. Schmitt, Q. Huang, J. G. Fujimoto, and H. Mashimo, "Characterization of buried glands before and after radiofrequency ablation by using 3-dimensional optical coherence tomography (with videos)," *Gastrointestinal Endoscopy,* vol. 76, pp. 32-40, Jul 2012.

[104] M. J. Suter, B. J. Vakoc, P. S. Yachimski, M. Shishkov, G. Y. Lauwers, M. Mino-Kenudson, B. E. Bouma, N. S. Nishioka, and G. J. Tearney, "Comprehensive microscopy of the esophagus in human patients with optical frequency domain imaging," *Gastrointestinal Endoscopy,* vol. 68, pp. 745-753, 2008.

[105] J. Sauk, E. Coron, L. Kava, M. Suter, M. Gora, K. Gallagher, M. Rosenberg, A. Ananthakrishnan, N. Nishioka, G. Lauwers, K. Woods, W. Brugge, D. Forcione, B. Bouma, and G. Tearney, "Interobserver Agreement for the Detection of Barrett's Esophagus with Optical Frequency Domain Imaging," *Digestive Diseases and Sciences,* pp. 1-5, 2013/03/19 2013.

[106] M. J. Cobb, J. H. Hwang, M. P. Upton, Y. C. Chen, B. K. Oelschlager, D. E. Wood, M. B. Kimmey, and X. D. Li, "Imaging of subsquamous Barrett's epithelium with ultrahigh-resolution optical coherence tomography: a histologic correlation study," *Gastrointestinal Endoscopy,* vol. 71, pp. 223-230, Feb 2010.

[107] G. Isenberg, M. V. Sivak, Jr., A. Chak, R. C. Wong, J. E. Willis, B. Wolf, D. Y. Rowland, A. Das, and A. Rollins, "Accuracy of endoscopic optical coherence tomography in the detection of dysplasia in Barrett's esophagus: a prospective, double-blinded study," *Gastrointest Endosc,* vol. 62, pp. 825-31, Dec 2005.

[108] J. Folkman, "Angiogenesis in cancer, vascular, rheumatoid and other disease," *Nat Med,* vol. 1, pp. 27-31, Jan 1995.

[109] A. Couvelard, F. Paraf, V. Gratio, J. Y. Scoazec, D. Henin, C. Degott, and J. F. Flejou, "Angiogenesis in the neoplastic sequence of Barrett's oesophagus. Correlation with VEGF expression," *Journal of Pathology,* vol. 192, pp. 14-18, Sep 2000.

[110] M. I. Auvinen, E. I. T. Sihvo, T. Ruohtula, J. T. Salminen, A. Koivistoinen, P. Siivola, R. Ronnholm, J. O. Ramo, M. Bergman, and J. A. Salo, "Incipient angiogenesis in Barrett's epithelium and lymphangiogenesis in Barrett's adenocarcinoma," *Journal of Clinical Oncology,* vol. 20, pp. 2971-2979, Jul 1 2002.

[111] S. Makita, Y. Hong, M. Yamanari, T. Yatagai, and Y. Yasuno, "Optical coherence angiography," *Optics Express,* vol. 14, pp. 7821-7840, Aug 2006.

[112] R. K. Wang, S. L. Jacques, Z. Ma, S. Hurst, S. R. Hanson, and A. Gruber, "Three dimensional optical angiography," *Optics Express,* vol. 15, pp. 4083-4097, Apr 2007.

[113] R. Reif and R. K. Wang, "Optical Microangiography Based on Optical Coherence Tomography," in *Optical Coherence Tomography: Technology and Applications*, W. Drexler and G. J. Fujimoto, Eds., ed Cham: Springer International Publishing, 2015, pp. 1373-1397.

[114] Y. Wang and R. Wang, "Autocorrelation optical coherence tomography for mapping transverse particle-flow velocity," *Opt Lett,* vol. 35, pp. 3538-40, Nov 1 2010.

[115] E. Jonathan, J. Enfield, and M. J. Leahy, "Correlation mapping method for generating microcirculation morphology from optical coherence tomography (OCT) intensity images," *Journal of Biophotonics,* vol. 4, pp. 583-587, Sep 2011.

[116] Y. Jia, O. Tan, J. Tokayer, B. Potsaid, Y. Wang, J. J. Liu, M. F. Kraus, H. Subhash, J. G. Fujimoto, J. Hornegger, and D. Huang, "Split-spectrum amplitude-decorrelation angiography with optical coherence tomography," *Opt Express,* vol. 20, pp. 4710-25, Feb 13 2012.

[117] A. Mariampillai, B. A. Standish, E. H. Moriyama, M. Khurana, N. R. Munce, M. K. K. Leung, J. Jiang, A. Cable, B. C. Wilson, I. A. Vitkin, and V. X. D. Yang, "Speckle variance detection of microvasculature using swept-source optical coherence tomography," *Optics Letters,* vol. 33, pp. 1530-1532, 2008.

[118] J. Enfield, E. Jonathan, and M. Leahy, "In vivo imaging of the microcirculation of the volar forearm using correlation mapping optical coherence tomography (cmOCT)," *Biomedical Optics Express,* vol. 2, pp. 1184-1193, May 1 2011.

[119] V. X. D. Yang, S.-j. Tang, M. L. Gordon, B. Qi, G. Gardiner, M. Cirocco, P. Kortan, G. B. Haber, G. Kandel, I. A. Vitkin, B. C. Wilson, and N. E. Marcon, "Endoscopic Doppler optical coherence tomography in the human GI tract: initial experience," *Gastrointestinal Endoscopy,* vol. 61, pp. 879-890, 2005.

[120] B. J. Vakoc, M. Shishko, S. H. Yun, W.-Y. Oh, M. J. Suter, A. E. Desjardins, J. A. Evans, N. S. Nishioka, G. J. Tearney, and B. E. Bouma, "Comprehensive esophageal microscopy by using optical frequency–domain imaging (with video)," *Gastrointestinal Endoscopy,* vol. 65, pp. 898-905, 2007.

[121] T.-H. Tsai, O. O. Ahsen, H.-C. Lee, K. Liang, M. Figueiredo, Y. K. Tao, M. G. Giacomelli, B. M. Potsaid, V. Jayaraman, Q. Huang, A. E. Cable, J. G. Fujimoto, and H. Mashimo, "Endoscopic Optical Coherence Angiography Enables Three Dimensional Visualization of Subsurface Microvasculature," *Gastroenterology,* vol. 147, pp. 1219-1221, 2014.

[122] X. M. Liu, M. J. Cobb, Y. C. Chen, M. B. Kimmey, and X. D. Li, "Rapid-scanning forward-imaging miniature endoscope for real-time optical coherence tomography," *Optics Letters,* vol. 29, pp. 1763-1765, Aug 1 2004.

[123] A. D. Aguirre, J. Sawinski, S. W. Huang, C. Zhou, W. Denk, and J. G. Fujimoto, "High speed optical coherence microscopy with autofocus adjustment and a miniaturized endoscopic imaging probe," *Optics Express,* vol. 18, pp. 4222-4239, Mar 1 2010.

[124] L. Huo, J. F. Xi, Y. C. Wu, and X. D. Li, "Forward-viewing resonant fiber-optic scanning endoscope of appropriate scanning speed for 3D OCT imaging," *Optics Express,* vol. 18, pp. 14375-14384, Jul 5 2010.

[125] S. Moon, S. W. Lee, M. Rubinstein, B. J. F. Wong, and Z. P. Chen, "Semi-resonant operation of a fiber-cantilever piezotube scanner for stable optical coherence tomography endoscope imaging," *Optics Express,* vol. 18, pp. 21183-21197, Sep 27 2010.

[126] Y. T. Pan, H. K. Xie, and G. K. Fedder, "Endoscopic optical coherence tomography based on a microelectromechanical mirror," *Optics Letters,* vol. 26, pp. 1966-1968, Dec 15 2001.

[127] W. Jung, D. T. McCormick, J. Zhang, L. Wang, N. C. Tien, and Z. P. Chen, "Three-dimensional endoscopic optical coherence tomography by use of a two-axis microelectromechanical scanning mirror," *Applied Physics Letters,* vol. 88, pp. -, Apr 17 2006.

[128] K. H. Kim, B. H. Park, G. N. Maguluri, T. W. Lee, F. J. Rogomentich, M. G. Bancu, B. E. Bouma, J. F. de Boer, and J. J. Bernstein, "Two-axis magnetically-driven MEMS scanning catheter for endoscopic high-speed optical coherence tomography," *Optics Express,* vol. 15, pp. 18130-18140, Dec 24 2007.

[129] A. D. Aguirre, P. R. Hertz, Y. Chen, J. G. Fujimoto, W. Piyawattanametha, L. Fan, and M. C. Wu, "Two-axis MEMS Scanning Catheter for Ultrahigh Resolution Three-dimensional and En Face Imaging," *Opt Express,* vol. 15, pp. 2445-53, Mar 05 2007.

[130] H. C. Park, C. Song, M. Kang, Y. Jeong, and K. H. Jeong, "Forward imaging OCT endoscopic catheter based on MEMS lens scanning," *Opt Lett,* vol. 37, pp. 2673-5, Jul 01 2012.

[131] P. H. Tran, D. S. Mukai, M. Brenner, and Z. P. Chen, "In vivo endoscopic optical coherence tomography by use of a rotational microelectromechanical system probe," *Optics Letters,* vol. 29, pp. 1236-1238, JUN 1 2004.

[132] P. R. Herz, Y. Chen, A. D. Aguirre, K. Schneider, P. Hsiung, J. G. Fujimoto, K. Madden, J. Schmitt, J. Goodnow, and C. Petersen, "Micromotor endoscope catheter for in vivo, ultrahigh-resolution optical coherence tomography," *Optics Letters,* vol. 29, pp. 2261-3, 2004/10/01 2004.

[133] T. H. Tsai, H. C. Lee, O. O. Ahsen, K. C. Liang, M. G. Giacomelli, B. M. Potsaid, Y. K. K. Tao, V. Jayaraman, M. Figueiredo, Q. Huang, A. E. Cable, J. Fujimoto, and H. Mashimo, "Ultrahigh speed endoscopic optical coherence tomography for gastroenterology," *Biomedical Optics Express,* vol. 5, pp. 4387-4404, Dec 2014.

[134] T. S. Wang, W. Wieser, G. Springeling, R. Beurskens, C. T. Lancee, T. Pfeiffer, A. F. W. van der Steen, R. Huber, and G. van Soest, "Intravascular optical coherence tomography imaging at 3200 frames per second," *Optics Letters,* vol. 38, pp. 1715-1717, May 15 2013.

[135] J. Mavadia, J. F. Xi, Y. P. Chen, and X. D. Li, "An all-fiber-optic endoscopy platform for simultaneous OCT and fluorescence imaging," *Biomedical Optics Express,* vol. 3, pp. 2851-2859, Nov 1 2012.

[136] J. Li, M. de Groot, F. Helderman, J. Mo, J. M. Daniels, K. Grunberg, T. G. Sutedja, and J. F. de Boer, "High speed miniature motorized endoscopic probe for optical frequency domain imaging," *Opt Express,* vol. 20, pp. 24132-8, Oct 22 2012.

[137] O. O. Ahsen, H.-C. Lee, M. G. Giacomelli, Z. Wang, K. Liang, T.-H. Tsai, B. Potsaid, H. Mashimo, and J. G. Fujimoto, "Correction of rotational distortion for catheter-based en face OCT and OCT angiography," *Optics Letters,* vol. 39, pp. 5973-5976, 2014.

[138] S. D. Chang, E. Murdock, Y. X. Mao, C. Flueraru, and J. Disano, "Stationary-fiber rotary probe with unobstructed 360 degrees view for optical coherence tomography," *Optics Letters,* vol. 36, pp. 4392-4394, Nov 2011.

[139] T. Y. Chen, N. Zhang, T. C. Huo, C. M. Wang, J. G. Zheng, T. Y. Zhou, and P. Xue, "Tiny endoscopic optical coherence tomography probe driven by a miniaturized hollow ultrasonic motor," *Journal of Biomedical Optics,* vol. 18, Aug 2013.

[140] H. C. Lee, O. O. Ahsen, K. C. Liang, Z. Wang, C. Cleveland, L. Booth, B. Potsaid, V. Jayaraman, A. E. Cable, H. Mashimo, R. Langer, G. Traverso, and J. G. Fujimoto, "Circumferential optical coherence tomography angiography imaging of the swine esophagus using a micromotor balloon catheter," *Biomedical Optics Express,* vol. 7, pp. 2927-2942, Aug 1 2016.

[141] W. Kang, H. Wang, Z. Wang, M. W. Jenkins, G. A. Isenberg, A. Chak, and A. M. Rollins, "Motion artifacts associated with in vivo endoscopic OCT images of the esophagus," *Optics Express,* vol. 19, pp. 20722-20735, Oct 10 2011.
[142] M. Guizar-Sicairos, S. T. Thurman, and J. R. Fienup, "Efficient subpixel image registration algorithms," *Opt Lett,* vol. 33, pp. 156-8, Jan 15 2008.
[143] Z. Wang, H. Kyono, H. G. Bezerra, H. Wang, M. Gargesha, C. Alraies, C. Y. Xu, J. M. Schmitt, D. L. Wilson, M. A. Costa, and A. M. Rollins, "Semiautomatic segmentation and quantification of calcified plaques in intracoronary optical coherence tomography images," *Journal of Biomedical Optics,* vol. 15, Nov-Dec 2010.
[144] H. S. Cho, S. J. Jang, K. Kim, A. V. Dan-Chin-Yu, M. Shishkov, B. E. Bouma, and W. Y. Oh, "High frame-rate intravascular optical frequency-domain imaging in vivo," *Biomed Opt Express,* vol. 5, pp. 223-32, Dec 16 2013.
[145] W. Yuan, J. Mavadia-Shukla, J. Xi, W. Liang, X. Yu, S. Yu, and X. Li, "Optimal operational conditions for supercontinuum-based ultrahigh-resolution endoscopic OCT imaging," *Opt Lett,* vol. 41, pp. 250-3, Jan 15 2016.
[146] Z. Wang, H.-C. Lee, O. O. Ahsen, B. Lee, W. Choi, B. Potsaid, J. Liu, V. Jayaraman, A. Cable, M. F. Kraus, K. Liang, J. Hornegger, and J. G. Fujimoto, "Depth-encoded all-fiber swept source polarization sensitive OCT," *Biomedical Optics Express,* vol. 5, pp. 2931-2949, Sep 1 2014.
[147] H. L. Fu, Y. Leng, M. J. Cobb, K. Hsu, J. H. Hwang, and X. Li, "Flexible miniature compound lens design for high-resolution optical coherence tomography balloon imaging catheter," *J Biomed Opt,* vol. 13, p. 060502, Nov-Dec 2008.
[148] J. Xi, L. Huo, Y. Wu, M. J. Cobb, J. H. Hwang, and X. Li, "High-resolution OCT balloon imaging catheter with astigmatism correction," *Opt Lett,* vol. 34, pp. 1943-5, Jul 1 2009.
[149] W. Kang, H. Wang, Y. Pan, M. W. Jenkins, G. A. Isenberg, A. Chak, M. Atkinson, D. Agrawal, Z. Hu, and A. M. Rollins, "Endoscopically guided spectral-domain OCT with double-balloon catheters," *Opt Express,* vol. 18, pp. 17364-72, Aug 2 2010.
[150] T. Endo, T. Awakawa, H. Takahashi, Y. Arimura, F. Itoh, K. Yamashita, S. Sasaki, H. Yamamoto, X. Tang, and K. Imai, "Classification of Barrett's epithelium by magnifying endoscopy," *Gastrointestinal Endoscopy,* vol. 55, pp. 641-647, 2002.
[151] P. R. Herz, Y. Chen, A. D. Aguirre, J. G. Fujimoto, H. Mashimo, J. Schmitt, A. Koski, J. Goodnow, and C. Petersen, "Ultrahigh resolution optical biopsy with endoscopic optical coherence tomography," *Optics Express,* vol. 12, pp. 3532-3542, JUL 26 2004.
[152] T.-H. Tsai, B. Potsaid, Y. K. Tao, V. Jayaraman, J. Jiang, P. J. S. Heim, M. F. Kraus, C. Zhou, J. Hornegger, H. Mashimo, A. E. Cable, and J. G. Fujimoto, "Ultrahigh speed endoscopic optical coherence tomography using micromotor imaging catheter and VCSEL technology," *Biomedical Optics Express,* vol. 4, pp. 1119-1132, Jul 1 2013.
[153] V. Jayaraman, J. Jiang, H. Li, P. J. S. Heim, G. D. Cole, B. Potsaid, J. G. Fujimoto, and A. Cable, "OCT imaging up to 760 kHz axial scan rate using single-mode 1310nm MEMS-tunable VCSELs with >100nm tuning range," in *Lasers and Electro-Optics (CLEO), 2011 Conference on*, 2011, pp. 1-2.
[154] J. A. Li, M. de Groot, F. Helderman, J. H. Mo, J. M. A. Daniels, K. Grunberg, T. G. Sutedja, and J. F. de Boer, "High speed miniature motorized endoscopic probe for optical frequency domain imaging," *Optics Express,* vol. 20, pp. 24132-24138, Oct 22 2012.
[155] K. Liang, G. Traverso, H. C. Lee, O. O. Ahsen, Z. Wang, B. Potsaid, M. Giacomelli, V. Jayaraman, R. Barman, A. Cable, H. Mashimo, R. Langer, and J. G. Fujimoto, "Ultrahigh

speed en face OCT capsule for endoscopic imaging," *Biomed Opt Express,* vol. 6, pp. 1146-63, Apr 1 2015.

[156] J. Mavadia, J. Xi, Y. Chen, and X. Li, "An all-fiber-optic endoscopy platform for simultaneous OCT and fluorescence imaging," *Biomed Opt Express,* vol. 3, pp. 2851-9, Nov 1 2012.

[157] N. Uribe-Patarroyo and B. E. Bouma, "Rotational distortion correction in endoscopic optical coherence tomography based on speckle decorrelation," *Opt Lett,* vol. 40, pp. 5518-21, Dec 1 2015.

[158] M. F. Kraus, B. Potsaid, M. A. Mayer, R. Bock, B. Baumann, J. J. Liu, J. Hornegger, and J. G. Fujimoto, "Motion correction in optical coherence tomography volumes on a per A-scan basis using orthogonal scan patterns," *Biomedical Optics Express,* vol. 3, pp. 1182-1199, Jun 1 2012.

[159] M. J. Gora, J. S. Sauk, R. W. Carruth, W. Lu, D. T. Carlton, A. Soomro, M. Rosenberg, N. S. Nishioka, and G. J. Tearney, "Imaging the upper gastrointestinal tract in unsedated patients using tethered capsule endomicroscopy," *Gastroenterology,* vol. 145, pp. 723-5, Oct 2013.

[160] A. Couvelard, F. Paraf, V. Gratio, J.-Y. Scoazec, D. HeÂnin, C. Degott, and J.-F. FleÂjou, "Angiogenesis in the neoplastic sequence of Barrett's oesophagus. Correlation with VEGF expression," *J Pathol,* vol. 192, pp. 14-18, 2000.

[161] V. Becker, M. Vieth, M. Bajbouj, R. M. Schmid, and A. Meining, "Confocal laser scanning fluorescence microscopy for in vivo determination of microvessel density in Barrett's esophagus," *Endoscopy,* vol. 40, pp. 888-891, Nov 2008.

[162] S. Yun, G. Tearney, J. de Boer, and B. Bouma, "Removing the depth-degeneracy in optical frequency domain imaging with frequency shifting," *Opt Express,* vol. 12, pp. 4822-8, Oct 4 2004.

[163] Z. Wang, H. C. Lee, D. Vermeulen, L. Chen, T. Nielsen, S. Y. Park, A. Ghaemi, E. Swanson, C. Doerr, and J. Fujimoto, "Silicon photonic integrated circuit swept-source optical coherence tomography receiver with dual polarization, dual balanced, in-phase and quadrature detection," *Biomedical Optics Express,* vol. 6, pp. 2562-2574, Jul 1 2015.

[164] M. J. Suter, P. A. Jillella, B. J. Vakoc, E. F. Halpern, M. Mino-Kenudson, G. Y. Lauwers, B. E. Bouma, N. S. Nishioka, and G. J. Tearney, "Image-guided biopsy in the esophagus through comprehensive optical frequency domain imaging and laser marking: a study in living swine," *Gastrointestinal Endoscopy,* vol. 71, pp. 346-353, Feb 2010.

[165] K. Beaudette, H. W. Baac, W. J. Madore, M. Villiger, N. Godbout, B. E. Bouma, and C. Boudoux, "Laser tissue coagulation and concurrent optical coherence tomography through a double-clad fiber coupler," *Biomedical Optics Express,* vol. 6, pp. 1293-1303, Apr 1 2015.

[166] K. K. Wang and R. E. Sampliner, "Updated Guidelines 2008 for the Diagnosis, Surveillance and Therapy of Barrett's Esophagus," *Am J Gastroenterol,* vol. 103, pp. 788-797, 2008.

[167] N. Thosani, B. K. Abu Dayyeh, P. Sharma, H. R. Aslanian, B. K. Enestvedt, S. Komanduri, M. Manfredi, U. Navaneethan, J. T. Maple, R. Pannala, M. A. Parsi, Z. L. Smith, S. A. Sullivan, and S. Banerjee, "ASGE Technology Committee systematic review and meta-analysis assessing the ASGE Preservation and Incorporation of Valuable Endoscopic Innovations thresholds for adopting real-time imaging-assisted endoscopic

targeted biopsy during endoscopic surveillance of Barrett's esophagus," *Gastrointest Endosc,* vol. 83, pp. 684-698 e7, Apr 2016.

[168] C. Mobius, H. J. Stein, I. Becker, M. Feith, J. Theisen, P. Gais, U. Jutting, and J. R. Siewert, "The 'angiogenic switch' in the progression from Barrett's metaplasia to esophageal adenocarcinoma," *Eur J Surg Oncol,* vol. 29, pp. 890-4, Dec 2003.

[169] V. J. A. Konda, J. Hart, S. Lin, M. Tretiakova, I. O. Gordon, L. Campbell, A. Kulkarni, M. Bissonnette, S. Seewald, and I. Waxman, "Evaluation of microvascular density in Barrett's associated neoplasia," *Modern Pathology,* vol. 26, pp. 125-130, Jan 2013.

[170] M. W. Shahid, J. E. Crook, A. Meining, A. Perchant, A. Buchner, V. Gomez, and M. B. Wallace, "Exploring the optimal fluorescein dose in probe-based confocal laser endomicroscopy for colonic imaging," *J Interv Gastroenterol,* vol. 1, pp. 166-171, Oct 2011.

[171] Y. Chen, A. D. Aguirre, P. L. Hsiung, S. Desai, P. R. Herz, M. Pedrosa, Q. Huang, M. Figueiredo, S. W. Huang, A. Koski, J. M. Schmitt, J. G. Fujimoto, and H. Mashimo, "Ultrahigh resolution optical coherence tomography of Barrett's esophagus: preliminary descriptive clinical study correlating images with histology," *Endoscopy,* vol. 39, pp. 599-605, Jul 2007.

[172] M. Singh, A. Bansal, W. L. Curvers, M. A. Kara, S. B. Wani, L. Alvarez Herrero, C. R. Lynch, M. C. van Kouwen, F. T. Peters, J. D. Keighley, A. Rastogi, K. Pondugula, R. Kim, V. Singh, S. Gaddam, J. J. Bergman, and P. Sharma, "Observer agreement in the assessment of narrowband imaging system surface patterns in Barrett's esophagus: a multicenter study," *Endoscopy,* vol. 43, pp. 745-51, Sep 2011.

[173] J. L. Fleiss, B. Levin, and M. C. Paik, *Statistical methods for rates and proportions*, 3rd ed. Hoboken, N.J.: J. Wiley, 2003.

[174] J. R. Landis and G. G. Koch, "The measurement of observer agreement for categorical data," *Biometrics,* vol. 33, pp. 159-74, Mar 1977.

[175] A. Swager, G. J. Tearney, C. L. Leggett, M. G. H. van Oijen, S. L. Meijer, B. L. Weusten, W. L. Curvers, and J. J. Bergman, "Identification of Volumetric Laser Endomicroscopy features predictive for early neoplasia in Barrett's esophagus using high-quality histological correlation," *Gastrointest Endosc,* 2016.

[176] K. N. Phoa, F. G. van Vilsteren, B. L. Weusten, R. Bisschops, E. J. Schoon, K. Ragunath, G. Fullarton, M. Di Pietro, N. Ravi, M. Visser, G. J. Offerhaus, C. A. Seldenrijk, S. L. Meijer, F. J. ten Kate, J. G. Tijssen, and J. J. Bergman, "Radiofrequency ablation vs endoscopic surveillance for patients with Barrett esophagus and low-grade dysplasia: a randomized clinical trial," *JAMA,* vol. 311, pp. 1209-17, Mar 26 2014.

[177] D. G. Hewett, M. E. Huffman, and D. K. Rex, "Leaving distal colorectal hyperplastic polyps in place can be achieved with high accuracy by using narrow-band imaging: an observational study," *Gastrointestinal Endoscopy,* vol. 76, pp. 374-380, Aug 2012.

[178] P. Sharma, J. J. G. H. M. Bergman, K. Goda, M. Kato, H. Messmann, B. R. Alsop, N. Gupta, P. Vennalaganti, M. Hall, V. Konda, A. Koons, O. Penner, J. R. Goldblum, and I. Waxman, "Development and Validation of a Classification System to Identify High-Grade Dysplasia and Esophageal Adenocarcinoma in Barrett's Esophagus Using Narrow-Band Imaging," *Gastroenterology,* vol. 150, pp. 591-598, Mar 2016.

[179] T. Kuiper, F. J. C. van den Broek, S. van Eeden, P. Fockens, and E. Dekker, "Feasibility and Accuracy of Confocal Endomicroscopy in Comparison With Narrow-Band Imaging

and Chromoendoscopy for the Differentiation of Colorectal Lesions," *Am J Gastroenterol,* vol. 107, pp. 543-550, 2012.

[180] R. A. Ganz, D. S. Utley, R. A. Stern, J. Jackson, K. P. Batts, and P. Termin, "Complete ablation of esophageal epithelium with a balloon-based bipolar electrode: a phased evaluation in the porcine and in the human esophagus," *Gastrointestinal Endoscopy,* vol. 60, pp. 1002-1010, Dec 2004.

[181] B. Dunkin, J. Martinez, P. Bejarano, C. Smith, K. Chang, A. Livingstone, and W. Melvin, "Thin-layer ablation of human esophageal epithelium using a bipolar radiofrequency balloon device," *Surgical Endoscopy,* vol. 20, pp. 125-130, 2006.

[182] T. H. Tsai, C. Zhou, Y. K. Tao, H. C. Lee, O. O. Ahsen, M. Figueiredo, T. Kirtane, D. C. Adler, J. M. Schmitt, Q. Huang, J. G. Fujimoto, and H. Mashimo, "Structural markers observed with endoscopic 3-dimensional optical coherence tomography correlating with Barrett's esophagus radiofrequency ablation treatment response (with videos)," *Gastrointest Endosc,* vol. 76, pp. 1104-12, Dec 2012.

[183] C. P. Fleming, H. Wang, K. J. Quan, and A. M. Rollins, "Real-time monitoring of cardiac radio-frequency ablation lesion formation using an optical coherence tomography forward-imaging catheter," *Journal of Biomedical Optics,* vol. 15, May-Jun 2010.

[184] H. Wang, W. Kang, T. Carrigan, A. Bishop, N. Rosenthal, M. Arruda, and A. M. Rollins, "In vivo intracardiac optical coherence tomography imaging through percutaneous access: toward image-guided radio-frequency ablation," *J Biomed Opt,* vol. 16, p. 110505, Nov 2011.

[185] X. Fu, Z. Wang, H. Wang, Y. T. Wang, M. W. Jenkins, and A. M. Rollins, "Fiber-optic catheter-based polarization-sensitive OCT for radio-frequency ablation monitoring," *Opt Lett,* vol. 39, pp. 5066-9, Sep 1 2014.

[186] D. Herranz, J. Lloret, S. Jimenez-Valero, J. L. Rubio-Guivernau, and E. Margallo-Balbas, "Novel catheter enabling simultaneous radiofrequency ablation and optical coherence reflectometry," *Biomed Opt Express,* vol. 6, pp. 3268-75, Sep 1 2015.

[187] D. C. Adler, S. W. Huang, R. Huber, and J. G. Fujimoto, "Photothermal detection of gold nanoparticles using phase-sensitive optical coherence tomography," *Optics Express,* vol. 16, pp. 4376-4393, Mar 31 2008.

[188] T. H. Tsai, B. Potsaid, M. F. Kraus, C. Zhou, Y. K. Tao, J. Hornegger, and J. G. Fujimoto, "Piezoelectric-transducer-based miniature catheter for ultrahigh-speed endoscopic optical coherence tomography," *Biomedical Optics Express,* vol. 2, pp. 2438-2448, Aug 1 2011.

[189] H.-C. Lee, J. J. Liu, Y. Sheikine, A. D. Aguirre, J. L. Connolly, and J. G. Fujimoto, "Ultrahigh-speed spectral domain optical coherence microscopy," *Biomed. Opt. Express,* vol. 4, p. 19, 2013.

[190] V. Westphal, A. M. Rollins, J. Willis, M. V. Sivak Jr, and J. A. Izatt, "Correlation of endoscopic optical coherence tomography with histology in the lower-GI tract," *Gastrointestinal Endoscopy,* vol. 61, pp. 537-546, 2005.

[191] J. Chennat, A. S. Ross, V. J. A. Konda, S. Lin, A. Noffsinger, J. Hart, and I. Waxman, "Advanced pathology under squamous epithelium on initial EMR specimens in patients with Barrett's esophagus and high-grade dysplasia or intramucosal carcinoma: implications for surveillance and endotherapy management," *Gastrointestinal Endoscopy,* vol. 70, pp. 417-421, Sep 2009.

[192] M. Titi, A. Overhiser, O. Ulusarac, G. W. Falk, A. Chak, K. Wang, and P. Sharma, "Development of subsquamous high-grade dysplasia and adenocarcinoma after

successful radiofrequency ablation of Barrett's esophagus," *Gastroenterology,* vol. 143, pp. 564-6 e1, Sep 2012.

[193] E. C. Gorospe, G. Sun, and K. K. Wang, "Endpoints for radiofrequency ablation in Barrett's dysplasia," *Am J Gastroenterol,* vol. 108, pp. 197-9, Feb 2013.

[194] S. S. Zeki, R. Haidry, T. A. Graham, M. Rodriguez-Justo, M. Novelli, J. Hoare, J. Dunn, N. A. Wright, L. B. Lovat, and S. A. C. McDonald, "Clonal Selection and Persistence in Dysplastic Barrett's Esophagus and Intramucosal Cancers After Failed Radiofrequency Ablation," *American Journal of Gastroenterology,* vol. 108, pp. 1584-1592, Oct 2013.

[195] M. Villiger, A. Soroka, G. J. Tearney, B. E. Bouma, and B. J. Vakoc, "Injury depth control from combined wavelength and power tuning in scanned beam laser thermal therapy," *Journal of Biomedical Optics,* vol. 16, Nov 2011.

[196] William C. Y. Lo, Néstor Uribe-Patarroyo, Ahhyun S. Nam, Martin Villiger, Benjamin J. Vakoc, and B. E. Bouma, "Laser thermal therapy monitoring using complex differential variance in optical coherence tomography," *Journal of Biophotonics,* 2016.

[197] A. M. Lee, L. Cahill, K. Liu, C. MacAulay, C. Poh, and P. Lane, "Wide-field in vivo oral OCT imaging," *Biomed Opt Express,* vol. 6, pp. 2664-74, Jul 1 2015.

[198] Y. Yoon, W. H. Jang, P. Xiao, B. Kim, T. Wang, Q. Li, J. Y. Lee, E. Chung, and K. H. Kim, "In vivo wide-field reflectance/fluorescence imaging and polarization-sensitive optical coherence tomography of human oral cavity with a forward-viewing probe," *Biomedical Optics Express,* vol. 6, pp. 524-535, Feb 1 2015.

[199] M. C. Pierce, R. L. Sheridan, B. H. Park, B. Cense, and J. F. de Boer, "Collagen denaturation can be quantified in burned human skin using polarization-sensitive optical coherence tomography," *Burns,* vol. 30, pp. 511-517, SEP 2004.

[200] J. Trunzo, M. McGee, B. Poulose, J. Willis, B. Ermlich, M. Laughinghouse, B. Champagne, C. Delaney, and J. Marks, "A feasibility and dosimetric evaluation of endoscopic radiofrequency ablation for human colonic and rectal epithelium in a treat and resect trial," *Surgical Endoscopy,* vol. 25, pp. 491-496, 2011.

[201] H. W. Huang, "Influence of blood vessel on the thermal lesion formation during radiofrequency ablation for liver tumors," *Med Phys,* vol. 40, p. 073303, Jul 2013.